CONTROL STRATEGY FOR MARINE RISER OF POSITION-MOORED VESSEL IN OPEN AND LEVEL ICE-COVERED SEA

NGUYEN HOANG DAT

NATIONAL UNIVERSITY OF SINGAPORE

2011

CONTROL STRATEGY FOR MARINE RISER OF POSITION-MOORED VESSEL IN OPEN AND LEVEL ICE-COVERED SEA

NGUYEN HOANG DAT
(B.Eng. (Hons.), HCMUT)

A THESIS SUBMITTED

FOR THE DEGREE OF DOCTOR OF PHILOSOPHY

DEPARTMENT OF CIVIL ENGINEERING

NATIONAL UNIVERSITY OF SINGAPORE

2011

ACKNOWLEDGEMENTS

TABLE OF CONTENTS

SUMMARY

Increasing safety and efficiency of drilling operation is a challenging research topic in offshore engineering especially when the operating location changes. Ensuring that marine risers remain functional during operations under "normal" environmental condition is critical. The main objective of the study is to present a control strategy for maintaining small end angles of marine riser during shallow water drilling operations by position-moored (PM) systems in open water and level ice-covered sea. Basically, an active positioning control using mooring line tensioning to reduce the riser end angles (REAs) in open sea is first formulated and illustrated numerically. Model experimental tests are then performed to validate the proposed control strategy. In addition, stresses along the riser due to bending are considered numerically, including the case where end bending stiffeners are used, which requires the REA control criterion to be replaced by one with terms related to the stresses at the riser ends. The proposed REA control strategy using line tensioning with vessel set-point chasing algorithm is extended for operation in level ice-covered sea.

In the normal drilling and work-over operations, the riser angles at the well-head and top joint must be kept within an allowable limit (ideally within $\pm 2^{o}$) to prevent the drilling string wearing against the ball joints and guarantee continuous drilling operation. Although this can be achieved by applying sufficient tension at the top of the riser, this may lead to higher stresses, requiring the use of pipes with higher strength or dimensions. Alternatively, the vessel may be moved to reduce the mean offset, and hence the REAs, by tensioning the mooring lines under normal environmental conditions. This minimizes the need for and/or fuel consumption of thrusters to control the surge and sway.

In this study, the minimization of vessel offset and REAs of the vessel-mooring-riser system is achieved by automatically changing the lengths of the mooring lines based on optimal set-point chasing. To design the control strategy, the mathematical model of the riser, mooring system and vessel is formulated. The riser is modeled using beam elements which include the flexural stiffness, since the latter can contribute significantly in shallow water condition. The cable catenary equation is used to analyze the mooring line and the effect of mooring is applied on the hull as position-dependent

external forces. The effect of the motions of the hull subjected to the environmental loads is integrated into the system by imposing externally defined oscillations at the top end of the riser. The effectiveness of the strategy is demonstrated by numerical simulations and experiments of a moored vessel. The simulations are conducted using the Marine System Simulator (MSS) developed by the Norwegian University of Science and Technology (NTNU) with some modifications to integrate the multi-cable mooring system and riser finite element model. The experiments were performed in the Marine Cybernetics Laboratory (MCLab) at the NTNU using the Cybership 3 model vessel, which is a 1:120 scaled model of the vessel used in the numerical simulation.

Bending stress in the riser may be a controlling factor in the performance of marine operations and hence studied herein. It is observed that for riser with hinge-connected ends, executing the proposed PM control reduces its bending stresses considerably. Hence its material/geometry can be optimally proportioned such that both the allowable limits of the REAs and the stresses are not exceeded. For the case where the riser is fitted with end bending stiffeners, the control criterion can be modified to account for the end bending stresses instead of REAs. The control strategy is shown to be similarly effective numerically.

The Arctic region is one of the most difficult areas to work in due to its remoteness, the extreme cold, and presence of dangerous sea ice. Normal dynamic positioning (DP) systems may not operate satisfactorily in ice-covered sea since they are designed for open water. For moored system in ice, it seems that no active control of PM system has been implemented with respect to riser performance. Therefore the control strategy for PM system proposed herein is extended to level ice-covered sea. For simulating ice-vessel interactions, an ice-breaking process is adopted, which considers the coupling between the vessel motion and the ice-breaking process. To validate the control performance in ice-covered sea, the vessel is first exposed to open water and then to level ice regime with different ice thicknesses. Numerically simulated results support the implementation of the proposed vessel set-point chasing algorithm using REA criterion in conjunction with line tensioning for moored vessel operating in level ice.

LIST OF TABLES

LIST OF FIGURES

LIST OF SYMBOLS

A	Cross-sectional area of riser pipe
A_c	Contact area of vessel hull and ice
A_m	Cross-sectional area of mooring line
A_{int}	Internal cross-sectional area of riser pipe
A_{out}	External cross-sectional area of riser pipe
B	Breadth of vessel
B_c	Length of crushing area
$\mathbf{C}_A$	Coriolis and centripetal matrix of water added mass
C_a	Allowable stress factor of riser
C_d	Drag coefficient of riser
C_f	Design case factor of riser
C_m	Added mass coefficient of riser
$\mathbf{C}_{RB}$	Skew-symmetric Coriolis and centripetal matrix of vessel
$\mathbf{C}_r$	Total structural damping matrix of riser
D	Draft of vessel
D_{int}	Internal diameter of riser pipe
$\mathbf{D}_{mo}$	Vector of additional damping from mooring system
$\mathbf{D}_L$	Linear damping matrix caused by wave-drift damping and skin friction
D_{out}	External diameter of riser pipe
$\mathbf{d}_{NL}$	Nonlinear damping vector
E	Young's modulus of riser material
$\mathbf{E}_b$	Diagonal scaling matrix
E_{ice}	Young's modulus of ice
E_m	Young's modulus of mooring line material
$\mathbf{F}_{hydro}$	Total hydrodynamic load vector acting on riser
$\mathbf{F}_{vessel}$	Force caused by specified vessel motion at sea surface
$\mathbf{G}_L$	Matrix of linear generalized gravitation and buoyancy force coefficients
g	Acceleration due to gravity
$\mathbf{g}_{mo}$	Mooring force vector in Earth-fixed frame
H_{ice}	Ice thickness
H_{moor}	Horizontal force at top point of mooring line

I	Second moment of inertia of riser pipe
$\mathbf{J}$	Transformation between Earth-fixed and body-fixed coordinates
$\mathbf{K}_r$	Total stiffness matrix of whole riser
$\mathbf{k}_e$	Elastic stiffness matrix of riser element
$\mathbf{k}_g$	Geometric stiffness matrix of riser element
L	Length of vessel
L_c	Crushing depth
L_m	Length of mooring line
l_c	Characteristic length of ice
$\mathbf{M}$	System inertia matrix of vessel
$\mathbf{M}_r$	Total mass matrix of entire riser
$\mathbf{m}_a$	Hydrodynamic added mass matrix of riser element
$\mathbf{m}_f$	Mass matrix of mud in riser element
$\mathbf{m}_s$	Structural mass matrix of riser element
$\mathbf{p}_w$	State of vessel WF model
$\mathbf{R}_{b,s,v}$	Ice resistances due to bending and submersion coupled with motion
$\mathbf{r}$	Riser displacement vector in global coordinate
$\mathbf{r}_e$	Riser displacement vector in local coordinate
r_{vessel}	Specified vessel motion at sea surface
$\mathbf{T}$	Transformation matrix from riser local to riser global coordinates
$\mathbf{T}_b$	User specified diagonal matrix of bias time constants
T_e	Effective tension of riser
T_{moor}	Tension of mooring line
t_w	Wall thickness of riser pipe
V_c	Current velocity
V_{moor}	Vertical force at top point of mooring line
V_w	Wind velocity
$\mathbf{w}_b$	Zero-mean Gaussian white noise vector (bias)
w_m	Weight in water per unit length of mooring line
$\mathbf{w}_w$	Zero-mean Gaussian white noise vector (WF)
X_{hor}	Horizontal distance from top point to anchor point of mooring line
$\bar{x}_i$	X-coordinate of winch position
$\bar{y}_i$	Y-coordinate of winch position

α_b	Riser bottom end angle
α_t	Riser top end angle
α_{ves}	Waterline entrance angle of vessel hull
β	Planar angle of mooring line
β_c	Current direction
β_w	Wind direction
Δr_{vessel}^*	Optimal vessel incremental position
δ_ρ	Density difference between water and ice
$\boldsymbol{\eta}$	Vessel position vector in Earth-fixed frame
$\boldsymbol{\eta}_r$	Reference position and heading vector in Earth-fixed frame
$\boldsymbol{\eta}_w$	Vessel WF motion vector in Earth-fixed frame
$\boldsymbol{\eta}_{Rw}$	Vessel WF motion vector in reference-parallel frame
μ_{ice}	Friction coefficient between vessel hull and ice
$\boldsymbol{\nu}$	Vessel velocity vector
$\boldsymbol{\nu}_r$	Relative velocity vector between vessel and current
ρ_a	Density of air
ρ_f	Density of internal fluid of riser
ρ_w	Density of sea water
σ	Bending stress of riser
σ_b	Bottom end bending stress of riser
σ_c	Crushing strength of ice
σ_e	von Mises equivalent stress of riser pipe
σ_f	Bending strength of ice
σ_{pr}	Radial stress of riser pipe
σ_{pz}	Axial stress of riser pipe
$\sigma_{p\theta}$	Hoop stress of riser pipe
σ_t	Top end bending stress of riser
σ_y	Yield strength of steel
$\boldsymbol{\tau}_{cmoor}$	Control force from mooring line
$\boldsymbol{\tau}_{cr}$	Vector of ice crushing load
$\boldsymbol{\tau}_{ice}$	Ice load
$\boldsymbol{\tau}_{moor}$	Mooring force vector in body-fixed frame
$\boldsymbol{\tau}_{thr}$	Thrust force vector

$\boldsymbol{\tau}_{wave2}$	Second-order wave load vector
$\boldsymbol{\tau}_{wind}$	Wind load vector
υ	Poisson coefficient
ϕ_{ves}	Stem angle of vessel hull
φ_{e}	Angle of axial axis of riser element in global coordinate
φ_{ice}	Opening angle of ice wedge
ψ_{ves}	Slope angle of vessel hull

LIST OF ABBREVIATIONS

API	American Petroleum Institute
CG	Centre of gravity
DCMV	Dynamics and control of marine vehicles
DNV	Det Norske Veritas
DOF	Degree of freedom
DP	Dynamic positioning
FE	Finite element
FEM	Finite element method
FPSO	Floating Production Storage and Offloading
GNC	Guidance and navigation control
JONSWAP	Joint North Sea wave project
LF	Low frequency
MCLab	Marine Cybernetic Laboratory
MCSim	Marine Cybernetics Simulator
MSS	Marine Systems Simulator
MCU	Motion capture unit
NTNU	Norwegian University of Science and Technology
PID	Proportional – Integral – Derivative
PM	Position mooring
QTM	Qualisys track manager
REA	Riser end angle
RPM	Revolutions per minute
SNAME	Society of naval architects and marine engineers
TLP	Tension leg platform
WAMIT	Wave analysis Massachusetts Institute of Technology
WF	Wave frequency

CHAPTER 1. INTRODUCTION

1.1   Background and Motivation

Increasing safety and efficiency of drilling operations is an important and challenging research topic in offshore engineering. In recent years, developments in oil and gas exploration have resulted in an increasing use of marine risers connecting a surface vessel or a platform to the well-head (through a blowout preventer (BOP)) at the seabed as shown in Figure 1.1.
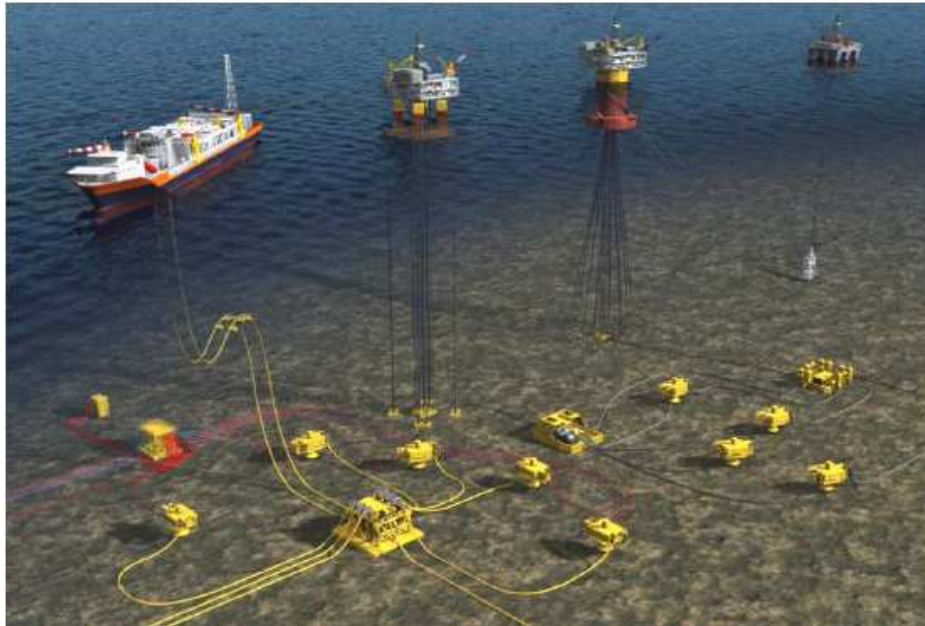
Figure 1.1. Oil and gas work-over and drilling operations

Marine risers are traditionally classified in two main groups, namely, production risers and drilling risers. Production risers can be found in a broad range of fluid-conveying applications whereas drilling risers are used in drilling operations. Normally, each drilling riser comprises rigid steel pipes, each with an average length of 12 m and an outer diameter between 0.4 and 1 m. When a drilling riser conducting a drilling or work-over operation is connected to a floating structure at the top end, the bottom end is then connected to the well-head at the sea floor through a BOP, schematically shown in Figure 1.2. The top end is subjected to the motion of the

structure, which will induce stresses along the riser. The bottom end is restrained in translational motions.
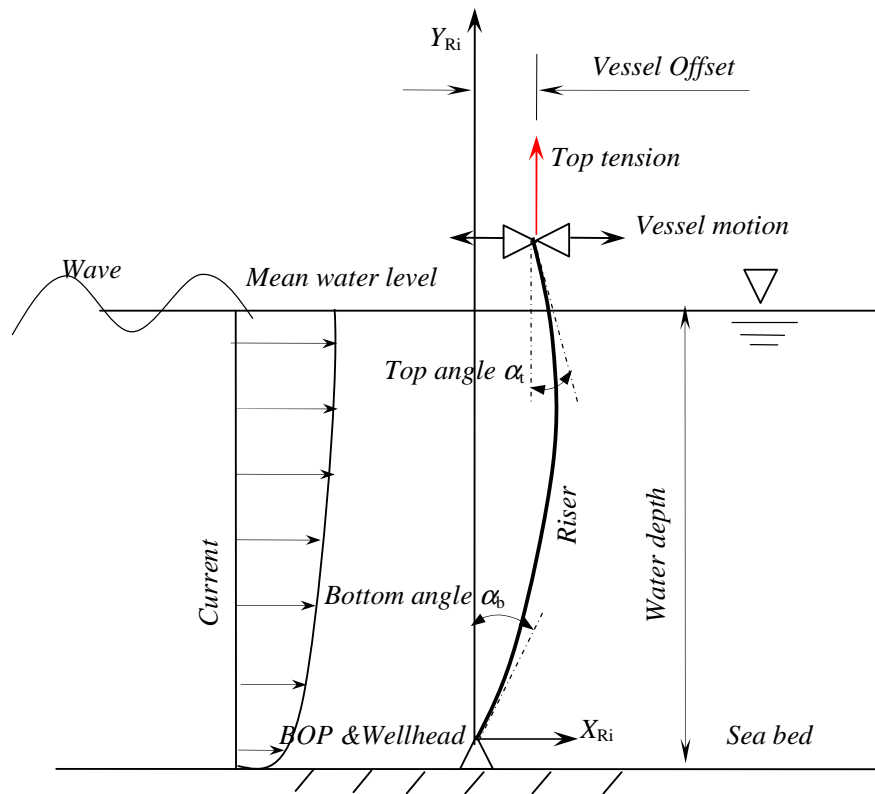
Figure 1.2. Typical drilling riser system

Under disturbances by the surrounding environment such as the wind, wave and ocean current, the position offsets of drilling vessels may become considerable and may cause large magnitudes of riser end angles (REAs) at the top joint and the well-head on the subsea structure. Therefore, the main concern is how to manage the excessive magnitudes of the REAs during drilling operations. This is particularly so when sea conditions become extreme, as the allowable limits of the REAs will usually be violated, leading to serious consequences. At the upper end of the riser, contacts between the riser pipe and the surface structure (e.g. the moon-pool) due to excessive top angle may lead to serious damage for some types of risers. At the lower end of riser, even moderate end angles ($2 - 4^{o}$) may cause the drilling string within the riser pipe to contact against the ball-joint or well-head (Sørensen, 2005a). For larger REAs, the operation has to be interrupted to prevent damage to the subsea system. This damage will lead to significant financial losses.

One way to avoid the resulting problems mentioned above is to keep the REAs under control to within allowable limits during drilling operations. This solution can be implemented by increasing the tension at the top of the riser or station keeping of the drilling vessel against the disturbances caused by winds, waves and ocean currents. Increasing the top tension can reduce deformation of the riser as well the REAs but the higher stresses may result in the need to use pipes of higher strength, which may be costly. In addition, this approach may not be effective if the REAs are caused by large vessel offsets since the top tension mainly reduces the REAs caused by current load. The second approach of station keeping is currently more popular, where the drilling vessel is kept close to a specified position by either dynamic positioning (DP) or position mooring (PM). DP system exclusively uses thrusters and is most efficient for deep water operations (Sørensen, 2005a). PM system differs from DP system in that thrusters are used only for keeping the desired heading whereas the position is kept to within an acceptable region by the mooring lines (DNV, 2004). The mooring system basically compensates for the slowly-varying disturbances. This is most efficient for moored vessels in shallow water as the operational cost and risk are low. However, it seems that no active control concept is implemented in PM system for minimizing the REAs. This may be a practically worthwhile and challenging pursuit since keeping the REAs within allowable limits will widen the operational window, and should be particularly applicable for shallow water depths where PM system shows a potential for lowering fuel consumption compared to DP system.

1.2   Brief Review of Previous Works

The state of research in modelling and control of REAs will be reviewed in the following sections. First, finite element modelling of marine risers will be presented. Next, the review continues with a brief review of operational control of marine risers. Subsequently, the review will focus on the dynamic positioning (DP) and position mooring (PM) for minimizations of the REAs in open water. Final, a review on station keeping for drilling operations in ice-covered sea is summarized.

1.2.1 Modelling of Marine Risers

Marine riser is a significant component in drilling and production operation for oil and gas. During the last two decades, significant efforts have been expended in the

modelling, static, dynamic and fatigue analyses of marine risers. API (1998) has recommended that some nonlinearities should be carefully considered in riser models and these include:

- Geometric stiffness, where variation in the effective tension contributes to the transverse stiffness in a nonlinear manner;
- Hydrodynamic loading where nonlinearities are introduced by the quadratic drag term in Morison's equation expressed in term of the relative structure-fluid velocity, and by the integration of hydrodynamic loading up to the actual surface elevation;
- Large displacement of the cable; and
- Material nonlinearities.

Depending on the specific problem of interest, one or more of the above nonlinearities may be neglected in the riser model. Amongst the various numerical models available for offshore engineering problems, the finite element (FE) method seems to be most popular due the intensive effort in its development and the availability of numerous commercial software packages. FE modelling of slender structures such as marine risers has been extensively covered by many text books and papers. In most of these models, subsystems such as surface vessel and submerged buoys, are usually considered as rigid bodies. Software packages, which have been used in offshore engineering, include ABAQUS, ADINA, RIFLEX and GMOOR.

Huang and Chucheepsakul (1985) and Huang and Kang (1991) proposed a Lagrangian formulation where the total energy of a riser pipe with a sliding top connection was derived and minimized using a variational approach to yield the equilibrium relationships and associated boundary conditions. The FE method was then used to obtain the equilibrium configuration iteratively using the Newton-Raphson method. The formulation uses exact expressions for pipe curvature and hence provides quite accurate solutions. Yardchi and Crisfield (2002) used simple lower-order two-dimensional beam elements for the non-linear FE static analysis of a curved beam to simulate the riser. The effects of buoyancy, steady-state current loading and top tension were included in their model. Subsequently, Kordkheili and Bahai (2007) used a four-node, twenty-four degrees of freedom pipe elbow element to obtain a more accurate non-linear FE solution to the riser problem. However, the FE formulations in these studies may be too complicated and computational costly for studying the control

of risers as lengthy simulations are needed. In a study of top tension control, Rustad et al. (2008) introduced a less complicated FE approach to model the top tensioned riser in deep water using a two-dimensional truss element with four degrees of freedom. By neglecting the bending stiffness, the implementation is highly simplified and the computational time significantly reduced. However in shallow water applications, the contribution of bending stiffness of the riser may be significant.

In riser modelling and analysis techniques, the mass matrix is usually established according to two different methods, namely a concentrated (lumped) mass matrix and a consistent mass matrix. Larsen (1976) and Patel et al. (1984) presented a two-dimensional FE model for the displacements and stresses of riser under self-weight, surface vessel motions and environmental forces. Engseth et al. (1988) developed a flexible riser analysis package in time domain technique, which offers linear and nonlinear analysis options. The package provided a facility for the analysis of various riser geometries. Ghadimi (1988) proposed a simple and efficient computational algorithm based on FE analysis to solve the equations of motion of flexible risers in three-dimensional space. Spanos et al. (1990) presented an approximate analysis procedure based on the concepts of equivalent linearization and time averaging to determine the riser maximum stress. The computational features of the proposed method made it quite appropriate for implementation in the preliminary design stage of marine risers. In these studies, the lumped mass approach was adopted. The lumped mass method, in which the deformation of each element is ignored, creates a diagonal mass matrix and negates the need to integrate mass across the deformed element. According to Patel et al. (1984) and Spanos et al. (1990), the lumped mass formulation permits an efficient numerical manipulation and leads to a simpler definition of element properties together with fewer degrees of freedom compared with the consistent mass formulation. However, the main difficulty lies in incorporating the riser effects with the parameters of the attached body. In addition, when dealing with the hydrodynamic mass contribution, the lumped mass formulation represents a simplification that may lead to loss of accuracy. This is related to the fact that the added mass matrix is non-isotropic, since the added mass is different for lateral and tangential motion of a pipe element. Hence, the consistent mass approach, in which the same interpolation polynomial is used for derivation of the displacement for both the mass and stiffness matrices, may be a better option. This approach was adopted in

Patel and Jesudasen (1987), Admad and Datta (1989), O'Brien and McNamara (1989), Sørensen et al. (2001), Kaewunruen et al. (2005), Jacobsen (2006) and Rustad (2007). In these studies, the FE method was employed to model the riser. The derivation of mass and stiffness matrices was based on interpolation polynomial, which describes the motion inside the element based on motion of the modes. When using the consistent mass formulation, it makes use of the FE concept and requires the mass matrix to be calculated from the same shape functions used in deriving the stiffness matrix. Hence, in the consistent mass matrix, coupling due to off-diagonal terms exists and all rotational as well as translational degrees of freedom must be included. By using the consistent mass approach, greater accuracy can be achieved. However, this requires more computational efforts than the lumped mass approach.

In many FE applications, such as in Tucker and Murtha (1973), Burke (1973), Wu (1976), Krolikowski and Gay (1980), Patel et al. (1984), Langley (1984), Kirk (1985), Chen (1987), Chen and Lin (1989), Spanos et al. (1990) and Ellwanger et al. (1991), the drag component due to hydrodynamic loading acting on the riser is linearized to simplify the analysis and allow frequency domain analysis methods to be applied. By linearizing, the drag component can be split into two terms, namely a damping term and an excitation term. The damping term is then added to the structural damping of the equation of motion. In some cases, such linearization may lead to loss of accuracy in the numerical model (Sørensen et al., 2001). In Krolikowski and Gay (1980), an improved linearization technique for frequency domain riser analyses was proposed. This method relied on a Fourier expansion of the nonlinear drag term where the harmonics above the fundamental were ignored. The results highlighted the significant improvement compared with the conventional linearized technique. Krolikowski and Gay's method appears to be suitable when time saving is required and time domain simulations are not available. Langley (1984) introduced an attractive method for linearization of the drag force in irregular seas. In this method, terms of the linearized drag coefficients were computed through fairly time consuming numerical integrations in two dimensions. This implies that the implementation is likely more complicated compared with a time domain analysis. Also using the Fourier expansion, Chen (1987) provided an improved drag force linearization technique to analyze the marine riser system subjected to single regular wave, steady current and platform offsets. The method achieved a better performance compared with the conventional

linearization scheme (the first order Fourier expansion). The merits of various linearization techniques in marine riser analyses were addressed in Leira (1987). In the past, when computational efforts are not available, frequency domain methods in conjunction with suitable linearization techniques offer large reduction in computational time. When modelling nonlinearities of the drag forces, a time domain analysis is employed. This technique requires high computational capacity to reduce access times. Such nonlinear drag forces are fully considered in Larsen (1976), Kirk et al. (1979), Patel et al. (1984), Patel and Jesudasen (1987), Admad and Datta (1989), Trim (1990), Larsen (1992), Sørensen et al. (2001), Jacobsen (2006), Rustad (2007) and Do and Pan (2009). Larsen (1976) employed a FE analysis in conjunction with a direct time integration method to provide a time domain technique for the analysis of marine risers. A computer program to perform the analysis described has been developed. This study was properly considered the nonlinear drag forces and therefore provided acceptable results. Patel et al. (1984) used the drag nonlinearity in time domain analysis. This study also carried out a linearized frequency domain analysis. The results of both analyses were then compared with those of API (1977) and a standard computer program. The results concluded the greater accuracy of nonlinear solutions. Subsequently, Patel and Jesudasen (1987) addressed a theoretical and experimental investigation of lateral dynamics of a riser when it disconnects from the subsea well-head and remains hanging freely from the surface vessel. The in-plane behaviour was investigated using the FE method and the Newmark-β time domain technique, which also accounted for the nonlinear drag forces. In Admad and Datta (1989), nonlinear effects due to the relative velocity squared drag force was fully considered by some iterative procedures in time marching integration algorithms. The results concluded that a simple linearization of the drag force leads to an under-estimation of about 20 to 40% in the maximum stress and an over-estimation up to 45% in the response. Jacobsen (2006) accounted the nonlinear drag force in riser models when testing the observer design for risers on tension leg platforms (TLP). In Rustad (2007), the nonlinearities were solved numerically by the Newton-Raphson iteration and Newmark-β time integration with constant acceleration at each time step. In a study of boundary control, Do and Pan (2009) derived a set of partial and ordinary differential equations and boundary conditions describing riser motions based on balancing internal and external forces and Hamilton principle. The nonlinear fluid drag

force was found by using Morison's equation. Generally, the effect of nonlinear drag forces is of vital importance for the riser dynamic behaviour and should be properly taken into account. It is observed that by taking advantages of computer effort and storage, most recent studies focused on the development of time domain techniques, which allows the nonlinearities, for riser applications.

1.2.2 Control of Marine Risers

Active control of vibrating slender structures have been investigated and implemented in many industrial applications. In offshore engineering, these structures include marine risers, free hanging underwater pipelines, and drill strings for oil and gas operations. Fard and Sagatun (2001) used the dynamic equations of motion of a nonlinear Euler-Bernoulli tensioned beam to study the boundary control. The novelty of this study is that it is possible to exponentially stabilize a free transversely vibrating beam by introducing a control law, which is a nonlinear function of the slopes and velocities at the boundary of the beam. Tanaka and Iwamoto (2007) also proposed an active boundary control of an Euler-Bernoulli beam that allows the generation of a desired boundary condition and a vibration-free state at a designated area of a target structure. In the boundary control approach, all control inputs are applied at the boundaries and the need for distributed actuators and sensors is ignored. In these two studies, distributed external forces as well as the structural self weight are not considered. Additionally, these studies only focus on two-dimensional beam models. In recent studies, Do and Pan (2008a, 2009) designed the boundary controllers actuated by hydraulic actuators at the top end for stabilization of riser vibrations. In Do and Pan (2009), a control problem of global stabilization for three-dimensional inextensible flexible marine riser system was investigated. The study handled the couplings between motions of the riser, which cause more difficulties in three-dimensional space. The study also presented proof of existence and uniqueness of the solution of the closed-loop system, which was not given in previous studies. In another study of boundary control, Do and Pan (2008b) proposed a nonlinear controller for active heave compensation to compensate for heave motions of a vessel connected to the riser. The goal of the proposed method is the use of the disturbance observers, which are then properly embedded in the control design procedure. Nguyen (2004) presented the beam and string equations for the observer design of flexible mechanical

systems described by partial differential equations. In this study, the observer was designed for a motorized Euler-Bernoulli beam and towed seismic streamer cables. Subsequently, Jacobsen (2006) carried out a study of observer design of risers by designing four different observers. FE methods including both bar and beam elements were employed to model the riser. The study showed that the observers were able to filter out the simple vortex-induced vibrations applied on the model, but they had some problems to follow the fast dynamics induced by TLP motions, which causes large estimation error. One possible solution could be to treat the TLP motion as a prescribed motion for the riser and not as a part of the observer. Rustad et al. (2008) proposed and investigated the concept of top tension control to prevent collision between two neighboring risers. Automatic control of top tension to achieve equal effective length for two risers decreased the number of collision, both in the static cases and in the cases with dynamic TLP motions. The proposed tasks are promising but model tests would be of importance for the actual implementation. In this study, bar elements were used for the FE riser model in deep water. This approach may simplify the calculation. However, the flexural stiffness may be significant in shallower water depths.

1.2.3 Control of Riser End Angles

Generally the excess of REAs is avoided by increasing tension at the top of riser or by station keeping of the drilling vessel against the disturbances caused by wind, wave and current. The concept of top tension control has been proposed and investigated by Rustad et al. (2008) using a two-dimensional FE riser model. However the study only focused on preventing collision between two neighboring risers. The active control the REAs by increasing top tension may be costly or even impossible if large vessel offsets are expected. It is therefore not surprising that most of studies on reducing the REAs focused on station keeping, where the floating vessels are kept in position either by PM with or without thruster assistance systems, or by DP using only thrusters.

The main objective of PM is to keep the vessel in a fixed position while the secondary objective is to keep the line tensions within a limited range to prevent line break. According to Strand et al. (1997, 1998), modelling and control of turret-moored vessels are complicated problems since the mooring forces are inherently nonlinear.

Strand et al. (1997) proposed a model and control strategy for PM satisfying the first objective. This study focused on introducing a simple mooring line model to simplify the control problem and reduce computational time. Following this, Aamo and Fossen (1999) worked on the control strategy for PM satisfying both the main and secondary objectives, and demonstrated the reduction in fuel consumption by letting the mooring system compensate for the slowly varying disturbances. This concept can be applied for keeping the REAs within allowable limits and optimizing fuel consumption. The use of thruster-assisted position mooring has recently been extended to extreme conditions by Nguyen and Sørensen (2009b). They proposed a supervisory switching control concept, which was experimentally verified.

In contrast to PM system, DP operation is used for non-anchored vessel where station keeping is left entirely to thrusters. Marine vessels with DP system are mostly used in oil and gas industries for exploration, exploitation, production and pipe laying. Early DP systems used conventional low-pass and single-input-single-output proportional-integral-derivative (PID) controller. The limitations of this controller are the poor wave filtering properties. Several recent studies have lifted these limitations considerably by introducing the passive nonlinear observer and effective filtering for wave frequency motions (Strand and Fossen, 1999). In a subsequent application of DP system, Sørensen et al. (2001) and Leira et al. (2004) proposed a control strategy to minimize the REAs by DP control. Criteria related to the riser angles were used for optimal set-point chasing of the vessel position. In another study, Suzuki et al. (1995) outlined an active control scheme by using DP control and thrusters attached along the riser that can deal with the case of strong current. The advantage of DP system is its flexibility to quickly establish position and operate in deep water exploration and exploitation (Sørensen, 2005a). However, drilling operations in shallow water are usually done by moored vessels due to their lower investment costs and reduced operational risk compared to DP.

1.2.4 Station Keeping for Drilling Operations in Ice-covered Sea

All the earlier works mentioned above were studied for open water where only wind, wave and ocean current are present. Despite the relative calmer sea conditions in the Arctic region, the presence of sea ice makes this area one of the most difficult areas to work in (Figure 1.3).

Figure 1.3. Representative ice conditions

According to Bonnemaire et al. (2007) and Kuehnlein et al. (2009), the presence of sea ice causes significant additional challenges for station keeping compared to open water operations. The additional issues include the capability of continuous ice breaking, the interactions between thrust and motions of vessels, and the drift and dynamic motions of the ice. The first report of DP operations in ice is in offshore Sakhalin (May – June 1999) with the CSO Constructor vessel (Keinonen et al., 2000). The CSO Constructor DP vessel (Figure 1.4) was supported by two ice-breakers, operating under 90% ice coverage with ice thickness varying in the range of 0.7 – 1.5 m. The operational downtime was 22%. Moran et al. (2006) reported the operations of a DP drilling vessel, the *Vidar Viking* (Figure 1.4), in the Arctic Ocean with more than 90% ice cover. Two other ice-breakers protected the *Vidar Viking* by circling upstream in the flowing sea ice and breaking the floes in smaller pieces. During the Arctic Coring Expedition (ACEX) in 2004, manual positioning with appropriate thrust was used to keep the vessel within the limits for maximum offsets. In this context, the downtime for the *Vidar Viking* vessel while on drilling locations was 38.3%. Although ice mechanics and ice load modelling have been extensively studied, few studies on DP systems in ice-covered sea have been presented in the open literature. Although DP is a well-designed system for open water, its ability to fulfill the control objectives under ice conditions remains unanswered. Recently, Nguyen et al. (2009a) modified the conventional DP controller for open water to extend its operation in ice-covered

water. A method for simulating the dynamic behaviour of DP vessels in level ice-covered sea was proposed. The study also showed that the modified DP controller for level ice performed better than the conventional controller for open water.

Figure 1.4. CSO Constructor vessel (left, photo by © AKAC INC) and Vidar Viking drill ship (right, photo by M. Jakobsson © ECORD/IODP)

While the DP systems have some challenges in ice (described by Kuehnlein et al., 2009); Bonnemaire et al. (2007) pointed out that moored structures supported by disconnection possibility of mooring systems and an efficient ice management system is an attractive option for most operations, including drilling and production of oil and gas, within a range of water depths in the Arctic region. The oil and gas development in the Arctic region was carried out earlier in the Beaufort Sea by moored platforms such as CanMar's drill ships and Kulluk platform (Figure 1.5). CanMar Explorer drill ships were fully equipped for arctic operations with an ice-reinforced hull, a mooring system and four tunnel thrusters (Hinkel et al., 1988). The mooring system of CanMar Explorer has a full remote anchor release capacity and collapsible anchor winch pawls. The drill ships were positioned at drilling locations by mooring lines while their desired positions were done by manual controls during drilling operations. The time lost due to ice conditions of CanMar Explorer was 41%. The Kulluk platform is a conical drilling unit, which was designed with a variety of special features to improve the performance in ice conditions (Wright, 2000). The system has good ice-breaking capabilities and a strong mooring system that could resist ice forces up to 450 tons. Recently the Submerged Turret Loading (STL) is widely using in the North Sea. For the increasing use of moored systems in ice, Løset et al. (1998) developed the model

tests of a STL to study the feasibility and line tension in level ice, broken ice and pressure ridges. Hansen and Løset (1999) simulated the behaviour of a vessel moored in broken ice and compared the simulation results with those obtained from ice tank tests.

Figure 1.5. Kulluk drilling vessel (left; Wright, 2000) and Canmar drill ship (right) in the Beaufort Sea (http://www.mms.gov)

In order to operate in the Arctic region, virtually all drilling vessels and platforms need ice-breakers to reduce the interference of ice during drilling operations. There are some delays in the operation until the ice condition improves, resulting in significant downtime. There are several PM systems reported to be operating in ice environment. However the mooring systems are normally not used to actively control the vessel motions as well as the REAs.

1.3   Objectives and Scope

From the above review, the following may be summarized:

a. In normal drilling operations, the REAs at the well-head and the top joint must be kept within allowable limits, ideally within $\pm 2^{o}$. Most studies focused on minimizing the REAs by station keeping through dynamic positioning. While the PM system has lower investment costs and operational risk in shallow water; no control concept for minimizing the REAs has been applied under such condition.

b. The Arctic region is rich in oil and gas and higher operational intensity is expected in the near future. As such the ability to operate offshore platforms

in ice-covered sea will be a principal concern. The presence of sea ice causes significant additional challenges for station keeping compared to open water operations. The operational downtime is significant due to manual controls of vessel positions and ice-breaker's activities for handling ice impacts. Although DP is a well-designed system for open water, its ability to fulfill the control objectives under ice conditions remains unanswered. As reported, PM systems are found to be more attractive in the Arctic region. However the mooring systems are normally not used to actively control the vessel motions as well as the REAs in ice conditions.

Therefore, the main objective of the study is to propose a control strategy for maintaining small REAs during shallow water drilling operations by PM systems in open water and level ice-covered sea. Specifically, the scopes of this study are to:

a. present process plant and control plant models of a drilling vessel and drilling riser for the control design of the REAs;

b. propose an active positioning control using mooring line tensioning for PM systems to reduce the REAs in open sea;

c. carry out experimental tests to validate the proposed control strategy;

d. extend the control algorithm to limit the riser end bending stresses rather than the REAs; and

e. extend the proposed control concept for operation in level ice-covered sea.

It should be noted that PM system is more efficient for calm and moderate sea conditions since the demand for thruster operation is less than that in DP system. In such environment, the mooring forces would counteract the slow-varying motions of the vessel. As such, the dynamic effects such as those induced by high frequency vortex-induced vibrations are not considered in this study. The applications of the control concept proposed in this study are limited to one moored vessel with one drilling riser.

1.4   Outline of Thesis

The thesis is organized as follows:

Chapter 1: A brief history of DP and PM systems in marine operations is summarized. The work of other researchers in the area of marine risers is also presented to explain the motivation behind this study. The objective and scope of this study is formulated.

Chapter 2: Process plant models of the riser, vessel and mooring system are presented. The FE beam element, which includes bending stiffness, is used to model the riser in two-dimensional space.

Chapter 3: This chapter mainly focuses on the control of REAs in PM systems through adjusting the vessel's position by changing the lengths of mooring lines in open water. The simulation and experimental results are also presented to verify the proposed control strategy.

Chapter 4: Bending stresses of the drilling riser during the control of the REAs are studied in this chapter. The control strategy proposed in Chapter 3 is extended to the control of the end bending stresses rather than the REAs.

Chapter 5: In this chapter, the alternative environmental condition of ice-covered sea is introduced. The set-point chasing algorithm based on the REAs proposed in Chapter 3 is used to generate vessel optimal positions. A coupling ice-vessel interaction is introduced to simulate level ice loads acting on vessels. Numerical simulations are carried out to test the control performance of the PM system under such environment.

Chapter 6: This chapter summarizes the key findings of this thesis. Subsequently, some areas where further work could be best directed are suggested.

CHAPTER 2.   MODEL OF VESSEL-MOORING-RISER SYSTEM

2.1   Introduction

The vessel-mooring-riser system has to be appropriately modeled to facilitate the design of controller. Within the field of marine control engineering, the control plant model and the process plant model are often introduced for the design and simulation of model-based control systems (Sørensen, 2005b). The process plant model describes the detailed physics of the actual process and simulates the real plant dynamics. The control plant model, which is a simplified mathematical version of the process plant model, is used for controller design and stability analysis. This chapter will mainly focus on the process plant model of the riser, vessel and mooring system.

The riser behaves like a tensioned beam when subject to current. In shallow water, the bending stiffness of the riser may influence its response significantly. Hence, to obtain the response via the FE method, the entire riser is normally discretized into beam elements, which includes the flexural stiffness.

The mooring system comprises a number of mooring lines to anchor the vessel in the desired positions. In this study, each mooring line is analyzed separately before assembling to obtain the total forces acting on the vessel. For simplicity, the catenary equations are normally used for the mooring analysis of anchored vessels by assuming that the dynamic effects such as high frequency vortex-induced vibrations are not significant.

In formulating the dynamics of the marine vessel, both low-frequency (LF) model and wave-frequency (WF) model are normally considered.

2.2   Kinematics and Coordinate Systems

In station keeping, the motion and state variables of the control system are defined and measured with respect to specific reference frames or coordinate systems as shown in Figures 2.1 and 2.2 (Sørensen, 2005b).
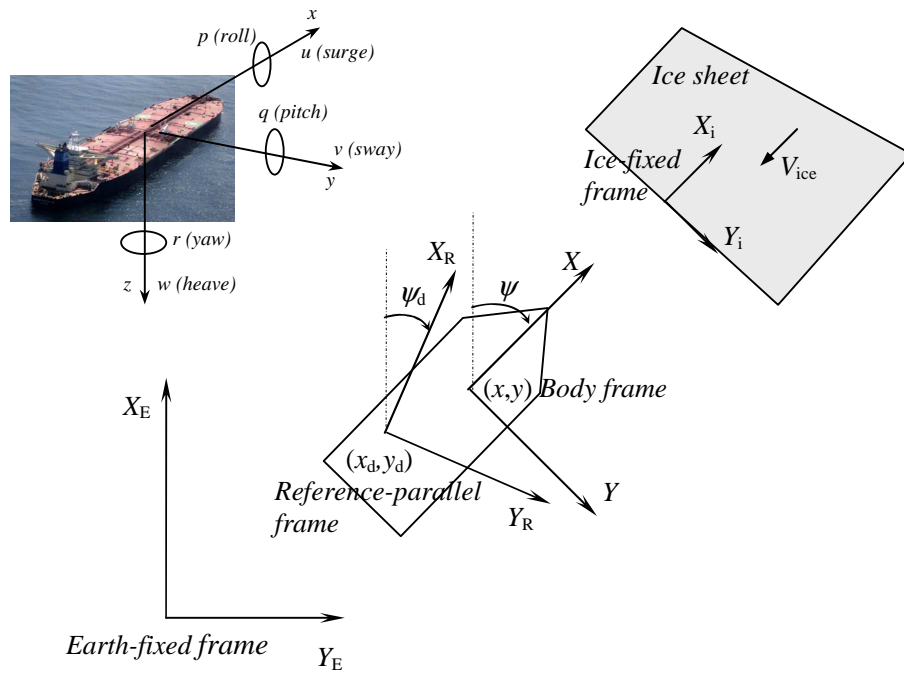
Figure 2.1. Vessel reference frames
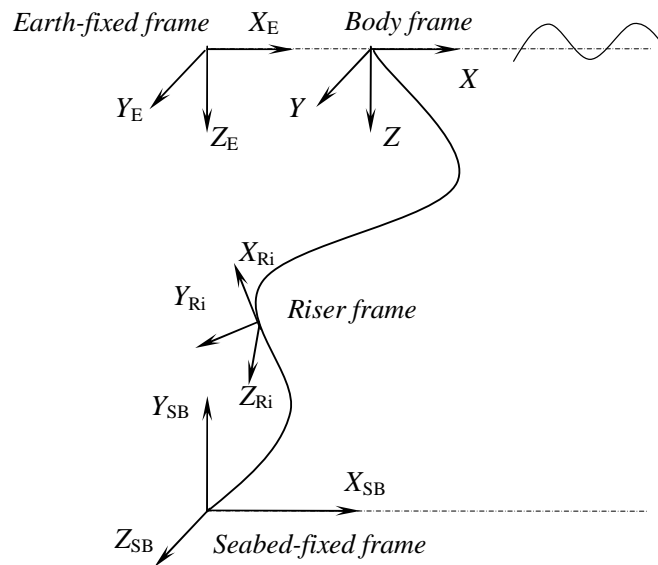
Figure 2.2. Riser reference frames

1. The Earth-fixed frame, denoted as $X_E Y_E Z_E$, is given in local geographical coordinates. The position and orientation of the vessel are measured in this frame relative to a defined origin.

2. The body-fixed frame, denoted as *XYZ*, is fixed to the vessel body with the origin coinciding with its center of gravity. The *X* axis is directed from aft to fore along the longitudinal axis of the vessel, and the *Y* axis is directed starboard, and *Z* axis is positive downwards. The motion and the loads acting on the vessel are calculated in this frame.

3. The reference-parallel frame, denoted as $X_R Y_R Z_R$, is Earth-fixed in station keeping operations. It is obtained by rotating the *XYZ* frame to the desired heading angle ψ_d and the origin is translated to the desired x_d and y_d position coordinates for the particular station keeping operation studied, as shown in Figure 2.1. The vessel is assumed to oscillate with small amplitudes about this frame such that linear theories may apply for modelling of the perturbations. Additionally, it is convenient to use this frame in the development of the control scheme.

4. The ice-fixed frame, denoted as $X_i Y_i Z_i$, is fixed to the ice sheet. The vessel hull and ice edge are discretized into a number of nodes with the nodal coordinates defined in this frame.

5. For the purpose of describing the force-displacement relationship of the riser at the elemental level, the local riser frame $X_{Ri} Y_{Ri} Z_{Ri}$ is introduced. The origin is located at the center line of the riser with X_{Ri} along the length of element *i* and $Y_{Ri} Z_{Ri}$ plane normal to the center line of each riser element as shown in Figure 2.2.

6. The sea bed-fixed frame is denoted as $X_{SB} Y_{SB} Z_{SB}$ with $X_{SB} Z_{SB}$ on the sea floor and Y_{SB} pointing upward. The positions of all the riser nodes in the global system are described relative to this frame.

The vectors defining the vessel's Earth-fixed position and orientation, and the body-fixed translation and rotation velocities (Figure 2.1) using SNAME (1950) notation are given by

$$\boldsymbol{\eta}_1 = \begin{bmatrix} x & y & z \end{bmatrix}^T, \quad \boldsymbol{\eta}_2 = \begin{bmatrix} \phi & \theta & \psi \end{bmatrix}^T \tag{2.1}$$

$$\mathbf{v}_1 = \begin{bmatrix} u & v & w \end{bmatrix}^T, \quad \mathbf{v}_2 = \begin{bmatrix} p & q & r \end{bmatrix}^T \tag{2.2}$$

where $\boldsymbol{\eta}_1$ denotes the position vector in the Earth-fixed frame, and $\boldsymbol{\eta}_2$ is a vector of Euler angles comprising the roll (ϕ), pitch (θ) and yaw (ψ); $\mathbf{v}_1$ denotes the body-fixed surge, sway and heave linear velocity vector, and $\mathbf{v}_2$ is the body-fixed roll, pitch and

yaw angular velocity vector. The transformation between the Earth-fixed and body-fixed coordinates can be realized through the matrix $\mathbf{J} \in \mathbb{R}^{6\times6}$ as follows (Fossen, 2002)

$$\dot{\boldsymbol{\eta}} = \begin{bmatrix} \dot{\boldsymbol{\eta}}_1 \\ \dot{\boldsymbol{\eta}}_2 \end{bmatrix} = \begin{bmatrix} \mathbf{J}_1(\boldsymbol{\eta}_2) & \mathbf{0}_{3\times3} \\ \mathbf{0}_{3\times3} & \mathbf{J}_2(\boldsymbol{\eta}_2) \end{bmatrix} \begin{bmatrix} \mathbf{v}_1 \\ \mathbf{v}_2 \end{bmatrix} = \mathbf{J}(\boldsymbol{\eta}_2)\mathbf{v} \tag{2.3}$$

where the rotation matrices $\mathbf{J}_1(\boldsymbol{\eta}_2) \in \mathbb{R}^{3\times3}$ and $\mathbf{J}_2(\boldsymbol{\eta}_2) \in \mathbb{R}^{3\times3}$ are functions of the Euler angles and are given by

$$\mathbf{J}_1(\boldsymbol{\eta}_2) = \begin{bmatrix} c\psi c\theta & -s\psi c\phi+c\psi s\theta s\phi & s\psi s\phi+c\psi c\phi s\theta \\ s\psi c\theta & c\psi c\phi+s\phi s\theta s\psi & -c\psi s\phi+s\theta s\psi c\phi \\ -s\theta & c\theta s\phi & c\theta c\phi \end{bmatrix} \tag{2.4}$$

$$\mathbf{J}_2(\boldsymbol{\eta}_2) = \begin{bmatrix} 1 & s\phi t\theta & c\phi t\theta \\ 0 & c\phi & -s\phi \\ 0 & s\phi/c\theta & c\phi/c\theta \end{bmatrix}, \quad c\theta \neq 0 \tag{2.5}$$

in which $s.=\sin(.)$, $c.=\cos(.)$ and $t.=\tan(.)$.

If only surge, sway and yaw (i.e. three degrees of freedom or 3DOF) are considered, the kinematics and the state vectors in (2.3) reduce to

$$\dot{\boldsymbol{\eta}} = \mathbf{R}(\psi)\mathbf{v} \qquad \text{or} \quad \begin{bmatrix} \dot{x} \\ \dot{y} \\ \dot{\psi} \end{bmatrix} = \begin{bmatrix} c\psi & -s\psi & 0 \\ s\psi & c\psi & 0 \\ 0 & 0 & 1 \end{bmatrix} \begin{bmatrix} u \\ v \\ r \end{bmatrix} \tag{2.6}$$

2.3 Model of Riser

2.3.1 Governing Equation of Motion

A drilling riser normally behaves like a long tensioned beam. The equations governing the lateral displacement of a tensioned beam under an externally applied dynamic load $f(x,t)$ and the effective tension T_e is given in API (1998) as

$$m(x)\frac{\partial^2 \eta(x,t)}{\partial t^2} + \frac{\partial^2}{\partial x^2}\left[EI(x)\frac{\partial^2 \eta(x,t)}{\partial x^2}\right] - \frac{\partial}{\partial x}\left[T_e(x,t)\frac{\partial \eta(x,t)}{\partial x}\right] = f(x,t) \tag{2.7}$$

where $m(x)$ is the mass per unit length, $EI(x)$ the bending stiffness, and $\eta(x,t)$ the transverse displacement (Figure 2.3). This equation was also derived by Fard (2001).
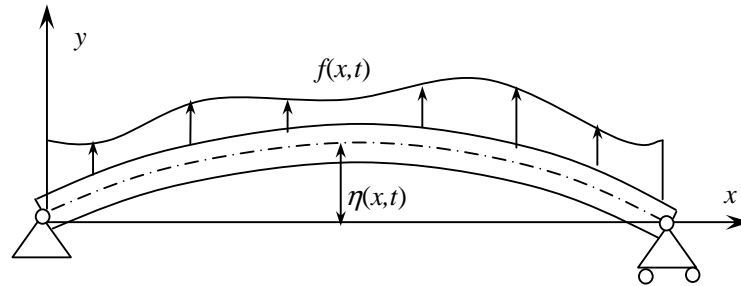
Figure 2.3. Transversely vibrating beam with lateral force

Under general conditions, the partial differential equation of (2.7) describing the static and dynamic behaviour of the riser cannot be solved exactly. Numerical solutions are often obtained by discretizing the entire riser into elements and then solved either by finite difference or FE techniques. As shown in Figure 2.4, the riser is modeled with n elements and $(n + 1)$ nodes, in which node 1 is at the sea bed and node $(n + 1)$ is at the surface vessel.
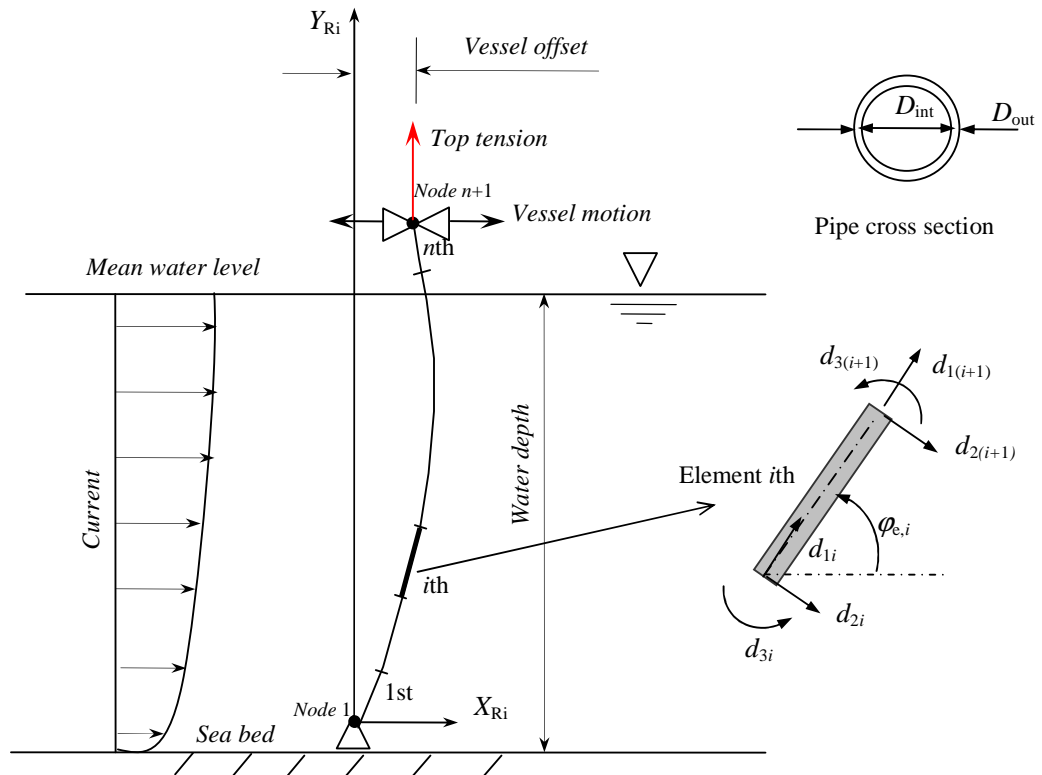
Figure 2.4. Riser model

2.3.2 Stiffness Model

In practice, drilling riser has a small diameter to length ratio and may operate under tension. Therefore, its stiffness is contributed by both elastic and geometric components. The flexural stiffness can be significant in shallow water and for the case of low tension. A suitable model for this contribution is the beam element. The geometric stiffness component is accounted for by considering the axial force. In FE application, the stiffness matrix is generically defined for each element based on the local coordinate system. In this study, 3 kinematic components (2 displacements and 1 rotation) at each end of a typical element are considered as shown in Figure 2.4.

The local stiffness matrix for each element $\mathbf{k}_i \in \mathbb{R}^{6 \times 6}$ is given by

$$\mathbf{k}_i = \left[\mathbf{k}_e + \mathbf{k}_g \right]_i \tag{2.8}$$

where $\mathbf{k}_e$ and $\mathbf{k}_g$ denote the elastic and geometric stiffness matrices, respectively. The elastic stiffness matrix is given by Przemieniecki (1968)

$$\mathbf{k}_e = \begin{bmatrix} \dfrac{EA}{l} & 0 & 0 & -\dfrac{EA}{l} & 0 & 0 \\[2mm] & \dfrac{12EI}{l^3} & \dfrac{6EI}{l^2} & 0 & -\dfrac{12EI}{l^3} & \dfrac{6EI}{l^2} \\[2mm] & & \dfrac{4EI}{l} & 0 & -\dfrac{6EI}{l^2} & \dfrac{2EI}{l} \\[2mm] & & & \dfrac{EA}{l} & 0 & 0 \\[2mm] & Sym. & & & \dfrac{12EI}{l^3} & -\dfrac{6EI}{l^2} \\[2mm] & & & & & \dfrac{4EI}{l} \end{bmatrix} \tag{2.9}$$

Different variations of the geometric stiffness matrix have been written and one that neglects the coupling effect between axial and flexural actions is

$$\mathbf{k}_{\text{g}} = \frac{T_{\text{e},i}}{l}
\begin{bmatrix}
0 & 0 & 0 & 0 & 0 & 0 \\
 & \dfrac{6}{5} & \dfrac{l}{10} & 0 & -\dfrac{6}{5} & \dfrac{l}{10} \\
 & & \dfrac{2l^2}{15} & 0 & -\dfrac{l}{10} & -\dfrac{l^2}{30} \\
 & & & 0 & 0 & 0 \\
 & \text{Sym.} & & & \dfrac{6}{5} & -\dfrac{l}{10} \\
 & & & & & \dfrac{2l^2}{15}
\end{bmatrix}
\tag{2.10}$$

where E is the Young's modulus of riser material, A the cross-sectional area of the riser pipe, I the second moment of inertia, l the element length, and $T_{\text{e},i}$ the effective tension.

When building the stiffness matrix, the effective tension $T_{\text{e},i}$ must be known. The effective tension at each element is given in API (1998) as

$$T_{\text{e},i} = T - A_{\text{int}} P_{\text{int},i} + A_{\text{out}} P_{\text{out},i} - w_i \tag{2.11}$$

where T is the tension at the top of the riser, A_{int} and A_{out} the internal and external cross-sectional areas, $P_{\text{int},i}$ and $P_{\text{out},i}$ the internal and external pressures of fluid at the node ith, and w_i the weight of the riser segment (steel pipe) above the node ith. Since the riser is originally vertical and the movements of the top end are small compared to the total riser length, it is assumed that the riser weight is in the riser line direction. The cross-sectional areas and pressures are given by

$$A_{\text{out}} = \frac{\pi D_{\text{out}}^2}{4}, \ A_{\text{int}} = \frac{\pi D_{\text{int}}^2}{4} \tag{2.12}$$

$$P_{\text{out},i} = \rho_{\text{w}} g h_i, \ P_{\text{int},i} = \rho_{\text{f}} g h_i \tag{2.13}$$

where D_{out} is the external diameter of riser pipe, D_{int} the internal diameter of riser pipe, ρ_{f} the density of internal fluid, ρ_{w} the density of surrounding water, g the acceleration due to gravity, and h_i the water depth of node ith.

To assemble the element matrices, all the matrices must first be expressed under a common coordinate system, which is the global coordinate system. The coordinate transformation matrix $\mathbf{T}_i \in \mathbb{R}^{6\times6}$ gives the relationship between the displacement vector $\mathbf{r}_{\text{e},i}$ based on the local coordinate system $X_{\text{Ri}}Y_{\text{Ri}}Z_{\text{Ri}}$ and the displacement vector $\mathbf{r}_i$ for the same element based on the global coordinate system $X_{\text{SB}}Y_{\text{SB}}Z_{\text{SB}}$. That is,

$$\mathbf{r}_i = \mathbf{T}_i^{\mathrm{T}} \mathbf{r}_{\mathrm{e},i} \tag{2.14}$$

where

$$\mathbf{r}_i = \begin{bmatrix} x_i & y_i & \alpha_i & x_i & y_{i+1} & \alpha_{i+1} \end{bmatrix}^T \tag{2.15}$$

$$\mathbf{r}_{\mathrm{e},i} = \begin{bmatrix} d_{1i} & d_{2i} & d_{3i} & d_{1(i+1)} & d_{2(i+1)} & d_{3(i+1)} \end{bmatrix}^T \tag{2.16}$$

$$\mathbf{T}_i = \begin{bmatrix} \cos\varphi_{\mathrm{e},i} & \sin\varphi_{\mathrm{e},i} & 0 & 0 & 0 & 0 \\ -\sin\varphi_{\mathrm{e},i} & \cos\varphi_{\mathrm{e},i} & 0 & 0 & 0 & 0 \\ 0 & 0 & 1 & 0 & 0 & 0 \\ 0 & 0 & 0 & \cos\varphi_{\mathrm{e},i} & \sin\varphi_{\mathrm{e},i} & 0 \\ 0 & 0 & 0 & -\sin\varphi_{\mathrm{e},i} & \cos\varphi_{\mathrm{e},i} & 0 \\ 0 & 0 & 0 & 0 & 0 & 1 \end{bmatrix} \tag{2.17}$$

The inclination $\varphi_{\mathrm{e},i}$ represents the direction the axial axis of element ith in the global coordinate system $X_{\mathrm{SB}}Y_{\mathrm{SB}}Z_{\mathrm{SB}}$ (see Figure 2.4).

The local stiffness matrix of each element is transformed to the global stiffness matrix through the transformation matrix $\mathbf{T}_i \in \mathbb{R}^{6\times 6}$ as

$$\mathbf{K}_i = \mathbf{T}_i^{\mathrm{T}} \mathbf{k}_i \mathbf{T}_i = \begin{bmatrix} \mathbf{K}_{11}^i & \mathbf{K}_{12}^i \\ \mathbf{K}_{21}^i & \mathbf{K}_{22}^i \end{bmatrix} \tag{2.18}$$

where $\mathbf{K}_{11}^i$, $\mathbf{K}_{12}^i$, $\mathbf{K}_{21}^i$ and $\mathbf{K}_{22}^i \in \mathbb{R}^{3\times 3}$ are the sub-matrices.

The total stiffness matrix for the whole riser is obtained by adding terms from the individual element stiffness matrices into their corresponding locations in the global stiffness matrix of the whole riser, $\mathbf{K}_{\mathrm{r}} \in \mathbb{R}^{3(n+1)\times 3(n+1)}$, where n is the number of elements considered. This can be represented as

$$\mathbf{K}_{\mathrm{r}} = \begin{bmatrix} \mathbf{K}_{11}^1 & \mathbf{K}_{12}^1 & 0 & 0 & .. & 0 & 0 & 0 & 0 \\ \mathbf{K}_{21}^1 & \mathbf{K}_{22}^1 + \mathbf{K}_{11}^2 & \mathbf{K}_{12}^2 & 0 & .. & 0 & 0 & 0 & 0 \\ 0 & \mathbf{K}_{21}^2 & \mathbf{K}_{22}^2 + \mathbf{K}_{11}^3 & \mathbf{K}_{12}^3 & .. & 0 & 0 & 0 & 0 \\ 0 & 0 & \mathbf{K}_{21}^3 & \mathbf{K}_{22}^3 + \mathbf{K}_{11}^4 & .. & 0 & 0 & 0 & 0 \\ .. & .. & .. & .. & .. & .. & .. & .. & .. \\ 0 & 0 & 0 & 0 & .. & \mathbf{K}_{22}^{n-3} + \mathbf{K}_{11}^{n-2} & \mathbf{K}_{12}^{n-2} & 0 & 0 \\ 0 & 0 & 0 & 0 & .. & \mathbf{K}_{21}^{n-2} & \mathbf{K}_{22}^{n-2} + \mathbf{K}_{11}^{n-1} & \mathbf{K}_{12}^{n-1} & 0 \\ 0 & 0 & 0 & 0 & .. & 0 & \mathbf{K}_{21}^{n-1} & \mathbf{K}_{22}^{n-1} + \mathbf{K}_{11}^{n} & \mathbf{K}_{12}^{n} \\ 0 & 0 & 0 & 0 & .. & 0 & 0 & \mathbf{K}_{21}^{n} & \mathbf{K}_{22}^{n} \end{bmatrix} \tag{2.19}$$

2.3.3 Inertia Model

The local mass matrix of element i, $\mathbf{m}_i \in \mathbb{R}^{6\times6}$, contains contributions from the structural mass of the riser $\mathbf{m}_s$ and the hydrodynamic added mass $\mathbf{m}_a$. The equivalent structural mass matrix is given in Przemieniecki (1968) as

$$\mathbf{m}_s = \rho_s A l \begin{bmatrix} \dfrac{1}{3} & 0 & 0 & \dfrac{1}{6} & 0 & 0 \\[2mm] & \dfrac{13}{35} & \dfrac{11l}{210} & 0 & \dfrac{9}{70} & -\dfrac{13l}{420} \\[2mm] & & \dfrac{l^2}{105} & 0 & \dfrac{13l}{420} & -\dfrac{l^2}{140} \\[2mm] & & & \dfrac{1}{3} & 0 & 0 \\[2mm] & Sym. & & & \dfrac{13}{35} & -\dfrac{11l}{210} \\[2mm] & & & & & \dfrac{l^2}{105} \end{bmatrix} \tag{2.20}$$

where ρ_s is the mass density of the riser.

The hydrodynamic added mass comes from the inertia forces on an accelerated circular cylinder in fluid (Faltinsen, 1990). For a fully submerged vertical element, the added mass associated with body acceleration is $\rho_w(C_m-1)A_{out}l$. The added mass matrix is then obtained as

$$\mathbf{m}_a = \rho_w \left(C_m - 1 \right) A_{out} l \begin{bmatrix} \dfrac{1}{3} & 0 & 0 & \dfrac{1}{6} & 0 & 0 \\[2mm] & \dfrac{13}{35} & \dfrac{11l}{210} & 0 & \dfrac{9}{70} & -\dfrac{13l}{420} \\[2mm] & & \dfrac{l^2}{105} & 0 & \dfrac{13l}{420} & -\dfrac{l^2}{140} \\[2mm] & & & \dfrac{1}{3} & 0 & 0 \\[2mm] & Sym. & & & \dfrac{13}{35} & -\dfrac{11l}{210} \\[2mm] & & & & & \dfrac{l^2}{105} \end{bmatrix} \tag{2.21}$$

where C_m is the inertial coefficient.

If fluid is present inside the drilling pipe, the element mass matrix must account for the contribution of the internal fluid given by

$$\mathbf{m}_f = \rho_f A_{int} l \begin{bmatrix} \dfrac{1}{3} & 0 & 0 & \dfrac{1}{6} & 0 & 0 \\[2mm] & \dfrac{13}{35} & \dfrac{11l}{210} & 0 & \dfrac{9}{70} & -\dfrac{13l}{420} \\[2mm] & & \dfrac{l^2}{105} & 0 & \dfrac{13l}{420} & -\dfrac{l^2}{140} \\[2mm] & & & \dfrac{1}{3} & 0 & 0 \\[2mm] & Sym. & & & \dfrac{13}{35} & -\dfrac{11l}{210} \\[2mm] & & & & & \dfrac{l^2}{105} \end{bmatrix} \qquad (2.22)$$

The total local mass matrix is obtained by summing the above matrices.

$$\mathbf{m}_i = \mathbf{m}_s + \mathbf{m}_a + \mathbf{m}_f \qquad (2.23)$$

The local element mass matrix is then transformed to the global coordinate system through the transformation matrix $\mathbf{T}_i$ as

$$\mathbf{M}_i = \mathbf{T}_i^T \mathbf{m}_i \mathbf{T}_i \qquad (2.24)$$

The global mass matrix of each element $\mathbf{M}_i$ is assembled into the total mass matrix $\mathbf{M}_r$ in the same manner as the stiffness matrix.

2.3.4 Damping Model

The damping experienced by the riser is a combination of the structural damping and hydrodynamic damping. Hydrodynamic damping is mainly caused by drag, which is a function of the relative velocity of riser and surrounding water. It is often considered together with the hydrodynamic loadings and hence discussed later.

Structural damping is comparatively smaller and may be approximated by *Rayleigh damping* model (Clough and Penzien, 2003) as

$$\mathbf{C}_r = a_1 \mathbf{M}_r + a_2 \mathbf{K}_r \qquad (2.25)$$

The coefficients a_1 and a_2 can be found by specifying two modal damping ratios, obtained either experimentally or from published literature. To facilitate the determination of the coefficients (2.25) is often expressed as a function of the damping ratio ξ_n and frequency ω_n of the nth mode,

$$\xi_n = \frac{a_1}{2\omega_n} + \frac{a_2\omega_n}{2} \tag{2.26}$$

Often, the same damping ratio is specified for the two selected modes (or control frequencies) due to lack of information on the variation of damping ratio with frequency. Equation (2.26) can be simplified as

$$\begin{Bmatrix} a_1 \\ a_2 \end{Bmatrix} = \frac{2\xi}{\omega_m + \omega_n} \begin{Bmatrix} \omega_m\omega_n \\ 1 \end{Bmatrix} \tag{2.27}$$

It is recommended that ω_m generally be taken as the fundamental frequency of the multi degrees of freedom system and that ω_n be set among the higher frequencies of the modes that contribute significantly to the dynamic response. A damping ratio of 5% (Larsen, 1976; Clough and Penzien, 2003) has been chosen for all the analyses carried out in this work.

2.3.5 Load Model

The forces acting on the riser are caused by vessel motions and hydrodynamic loads. The modified Morison's equation for moving cylinders (Faltinsen, 1990) is adopted to calculate the hydrodynamic load per unit length of a riser subjected to wave and current fields, written as

$$f_h = \frac{1}{2}\rho_w C_d D_{out} |v_w - \dot{r}|(v_w - \dot{r}) + \rho_w C_m \frac{\pi D_{out}^2}{4}\dot{v}_w - \rho_w (C_m - 1)\frac{\pi D_{out}^2}{4}\ddot{r} \tag{2.28}$$

where the velocities v_w and $\dot{v}_w$ are the water particle velocity and acceleration respectively, $\dot{r}$ the structure velocity, C_d the drag coefficient, and the remaining parameters are defined in the previous section. The last term of (2.28) is the added mass and is assembled in the element mass matrix. The second term is the fluid inertia force that is considered negligible in comparison with the drag force (Kirk et al., 1979 and Rustad et al., 2008). Hence, the hydrodynamic load due to the drag force per unit length of the riser at a particular location in depth is approximated as

$$f_h = \frac{1}{2}\rho_w C_d D_{out} |v_w - \dot{r}|(v_w - \dot{r}) \tag{2.29}$$

The load vector of each element is expressed with respect to the local coordinate frame. The force acting at each node of the element is obtained by integrating the force intensity with the assumed displacement shape function,

$$\mathbf{f}_i = \int_l \mathbf{N}^{\mathrm{T}} \mathbf{f}(x)\,dx \tag{2.30}$$

where $\mathbf{f}(x) \in \mathbb{R}^2$ is the distributed hydrodynamic load vector acting along the element in the normal and tangent directions, x the longitudinal coordinate of the element, and $\mathbf{N}^{\mathrm{T}} \in \mathbb{R}^{6\times2}$ is the matrix of shape functions given by (Przemieniecki, 1968)

$$\mathbf{N}^{\mathrm{T}} = \begin{bmatrix} 1-\dfrac{x}{l} & 0 \\[2mm] 0 & 1-3\dfrac{x^2}{l^2}+2\dfrac{x^3}{l^3} \\[2mm] 0 & x-2\dfrac{x^2}{l}+\dfrac{x^3}{l^2} \\[2mm] \dfrac{x}{l} & 0 \\[2mm] 0 & 3\dfrac{x^2}{l^2}-2\dfrac{x^3}{l^3} \\[2mm] 0 & -\dfrac{x^2}{l}+\dfrac{x^3}{l^2} \end{bmatrix} \tag{2.31}$$

The local force vector at each node is subsequently transformed into the global system through the transformation matrix $\mathbf{T}_i$.

$$\mathbf{F}_i = \mathbf{T}_i^{\mathrm{T}} \mathbf{f}_i \tag{2.32}$$

where $\mathbf{F}_i$ is the global force vector. $\mathbf{F}_i$ are then added into their corresponding locations in the total load vector $\mathbf{F}_{\mathrm{hydro}}$ of the whole riser.

2.3.6 Governing Equation of Motion in FE method

The differential equation of motion for a system with multi degrees of freedom can be written as

$$\mathbf{M}_{\mathrm{r}}(\mathbf{r})\ddot{\mathbf{r}} + \mathbf{C}_{\mathrm{r}}(\mathbf{r})\dot{\mathbf{r}} + \mathbf{K}_{\mathrm{r}}(\mathbf{r})\mathbf{r} = \mathbf{F}_{\mathrm{hydro}} \tag{2.33}$$

where $\mathbf{r}$ is the nodal displacement vector. The system mass matrix $\mathbf{M}_{\mathrm{r}}$, structural damping matrix $\mathbf{C}_{\mathrm{r}}$ and stiffness matrix $\mathbf{K}_{\mathrm{r}}$ have been defined in the previous sections. The drag force is included in $\mathbf{F}_{\mathrm{hydro}}$. The vessel motion is accounted for through the prescribed DOF at the top joint of the riser. The governing equation is written with respect to the global (sea-bed fixed frame) coordinate $X_{\mathrm{SB}}Y_{\mathrm{SB}}Z_{\mathrm{SB}}$ and the displacement vector $\mathbf{r} \in \mathbb{R}^{3(n+1)}$ is given by

$$\mathbf{r} = \begin{bmatrix} x_1 & y_1 & \alpha_1 & \cdots & x_{i+1} & y_{i+1} & \alpha_{i+1} & \cdots & x_{n+1} & y_{n+1} & \alpha_{n+1} \end{bmatrix}^{\mathrm{T}} \tag{2.34}$$

The matrix equation in (2.33) can be partitioned into unknown degrees of freedom (DOF) denoted by subscript A and known DOFs (denoted by subscript B) including the horizontal riser nodal translation at the surface. Hence, (2.33) becomes

$$\begin{bmatrix} \mathbf{M}_{AA} & \mathbf{M}_{AB} \\ \mathbf{M}_{BA} & \mathbf{M}_{BB} \end{bmatrix} \begin{bmatrix} \ddot{\mathbf{r}}_A \\ \ddot{\mathbf{r}}_B \end{bmatrix} + \begin{bmatrix} \mathbf{C}_{AA} & \mathbf{C}_{AB} \\ \mathbf{C}_{BA} & \mathbf{C}_{BB} \end{bmatrix} \begin{bmatrix} \dot{\mathbf{r}}_A \\ \dot{\mathbf{r}}_B \end{bmatrix} + \begin{bmatrix} \mathbf{K}_{AA} & \mathbf{K}_{AB} \\ \mathbf{K}_{BA} & \mathbf{K}_{BB} \end{bmatrix} \begin{bmatrix} \mathbf{r}_A \\ \mathbf{r}_B \end{bmatrix} = \begin{bmatrix} \mathbf{F}_{A\text{hydro}} \\ \mathbf{F}_{B\text{hydro}} \end{bmatrix} \tag{2.35}$$

The dynamic response of the riser structure can be written in terms of the unknown DOFs on the left hand side as

$$\mathbf{M}_{AA}\ddot{\mathbf{r}}_A + \mathbf{C}_{AA}\dot{\mathbf{r}}_A + \mathbf{K}_{AA}\mathbf{r}_A = \mathbf{F}_{A\text{hydro}} - \mathbf{M}_{AB}\ddot{\mathbf{r}}_B - \mathbf{C}_{AB}\dot{\mathbf{r}}_B - \mathbf{K}_{AB}\mathbf{r}_B \tag{2.36}$$

The right hand side of (2.35) facilitates the incorporation of the boundary condition at the riser top end, which must follow the surge motion of the surface platform. When the bottom of the riser is hinged at the wellhead, the second, third and fourth terms in the right hand side of (2.36) become the force required to cause the specified vessel motion at the surface $\mathbf{F}_{\text{vessel}}$. Hence, (2.36) can be re-written as

$$\mathbf{M}_{AA}\ddot{\mathbf{r}}_A + \mathbf{C}_{AA}\dot{\mathbf{r}}_A + \mathbf{K}_{AA}\mathbf{r}_A = \mathbf{F}_{A\text{hydro}} + \mathbf{F}_{\text{vessel}} \tag{2.37}$$

where

$$\mathbf{F}_{\text{vessel}} = -\mathbf{M}_{AB}\ddot{\mathbf{r}}_B - \mathbf{C}_{AB}\dot{\mathbf{r}}_B - \mathbf{K}_{AB}\mathbf{r}_B \tag{2.38}$$

$$\mathbf{r}_A = \begin{bmatrix} \alpha_1 & x_2 & y_2 & \alpha_2 & \cdots & x_i & y_i & \alpha_i & \cdots & x_n & y_n & \alpha_n & y_{n+1} & \alpha_{n+1} \end{bmatrix}^{\mathrm{T}} \tag{2.39}$$

$$\mathbf{r}_B = \begin{bmatrix} x_1 & y_1 & x_{n+1} \end{bmatrix}^{\mathrm{T}} = \begin{bmatrix} 0 & 0 & r_{\text{vessel}} \end{bmatrix}^{\mathrm{T}} \tag{2.40}$$

The DOFs in (2.39) that are removed from (2.34) are x_1 and y_1 corresponding to the bottom pin joint, and x_{n+1} corresponding to the vessel motion at the surface r_{vessel} (i.e. surge). Hence, the dimension of $\mathbf{r}_A$ reduces to $3n$, where n is the number of elements.

Various methods to solve (2.37) are available (Clough and Penzien, 2003) and for this problem where the drag force is dependent on the unknown velocities $\dot{\mathbf{r}}$, Newmark-β numerical time integration method with constant acceleration in each time step may be adopted. This method of analysis can account for the nonlinear drag loading (Fylling et al., 2005).

2.4   Multi-cable Mooring System

A moored vessel contains a number of mooring lines as shown in Figure 2.5, each attached to the vessel at one end usually via a winch system with the other end attached to a drag anchor or pile embedded in the seabed. As illustrated in Figure 2.6 of a semi-submersible, each mooring line leads from an anchor through pulley wheels (known as *Fairleads*) and to a tensioning device (known as *Winches*).
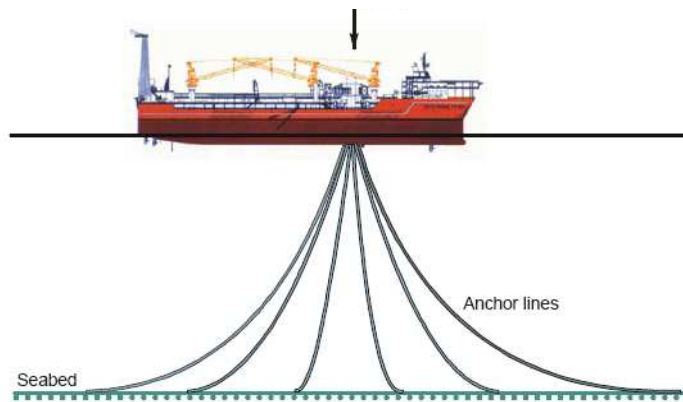
Figure 2.5. Vessel moored with anchor line system
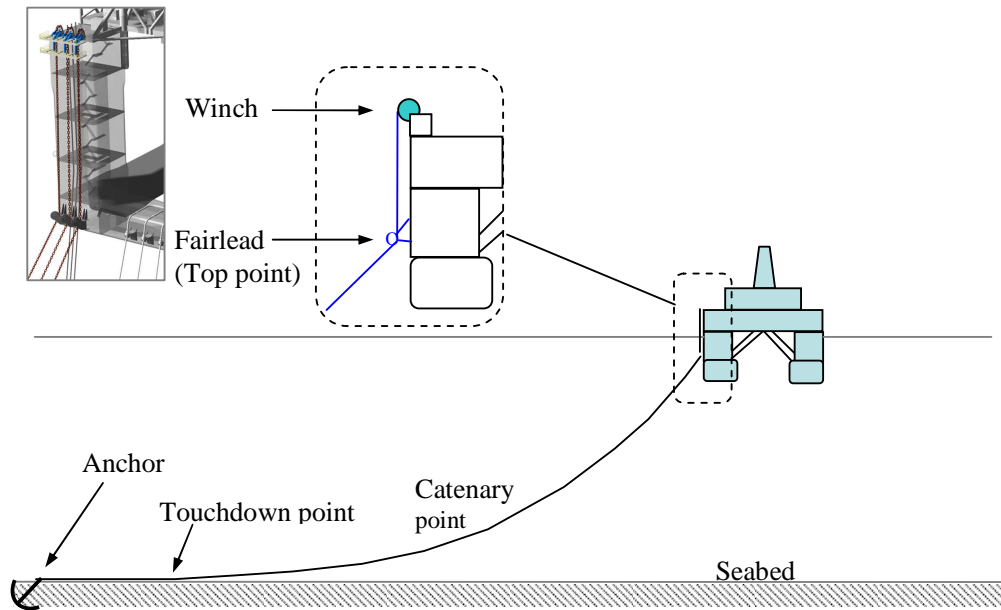
Figure 2.6. Arrangement of a mooring line

The lines are either in the form of chain, rope or a combination of both. Ropes can be made from steel, natural fibres and/or synthetic fibres. Segmented anchor lines, that is, cables comprising two or more lengths of different material, are used to achieve a heavy cable at the bottom and a lighter one close to the water surface. This achieves the effect of a stiffer and yet lighter anchor lines, compared to that using a single material. The initial tension in a cable is the result of winching the cable to position the platform in the desired configuration.

It should be mentioned that mooring lines in general are subjected to three types of excitations (Triantafyllou, 1990), namely large amplitude low frequency (LF) motions, medium amplitude wave frequency (WF) motions and small amplitude, very high frequency, vortex-induced vibrations. For the design of PM control system, it is simpler to consider the influence of the LF motion on the mooring lines and not to model the dynamic effects such as those induced by high frequency vortex-induced vibrations (Strand, 1999; Aamo and Fossen, 2001).

2.4.1 Force in a Mooring Line

The horizontal motion of the vessel is affected by the horizontal component of the tensile force at the top of each mooring cable attached to it. The horizontal force contribution $H_{\text{moor},i}$ of line i is a function of the horizontal distance between the top point and the anchor point of the line, denoted as $X_{\text{hor},i}$ as well as the line length $L_{\text{m},i}$. That is

$$H_{\text{moor},i} = f_i\left(X_{\text{hor},i}, L_{\text{m},i}\right) \tag{2.41}$$

When the position of the line's upper end, the anchor position and the static line length are known, the line tension and its horizontal component at the upper end can be obtained.

The profile of a mooring line is sketched in Figure 2.7. The elastic catenary equations of a single mooring line are used to express the static line characteristics and solve for the line tension T_{moor} and its horizontal component H_{moor}. These are (Triantafyllou, 1990)

$$H_{\text{moor}} \tan \varphi = V_{\text{moor}} - w_{\text{m}}\left(L_{\text{m}} - s\right) \tag{2.42}$$

$$V_{\text{moor}} = V_1 + w_{\text{m}} L_{\text{m}} \tag{2.43}$$

$$x = \frac{H_{moor}}{w_m} \left(\sinh^{-1} \left[\frac{V_{moor} - w_m(L_m - s)}{H_{moor}} \right] - \sinh^{-1} \left[\frac{V_{moor} - w_m L_m}{H_{moor}} \right] \right) + \frac{H_{moor} s}{E_m A_m} \tag{2.44}$$

$$z = \frac{H_{moor}}{w_m} \left(\sqrt{1 + \left(\frac{V_{moor} - w_m(L_m - s)}{H_{moor}} \right)^2} - \sqrt{1 + \left(\frac{V_{moor} - w_m L_m}{H_{moor}} \right)^2} \right)$$
$$+ \frac{1}{E_m A_m} \left(V_{moor} s + \frac{w_m}{2} \left[(L_m - s)^2 - L_m^2 \right] \right) \tag{2.45}$$

where L_m is the unstretched line length, w_m the weight in water per unit length, E_m the Young's modulus of elasticity, A_m the cross-sectional area of line, s a parameter running along the cable from 0 to L_m, $x(s)$ and $z(s)$ the spatial x- and z-coordinates of points along the cable respectively, $T_{moor} = \sqrt{V_{moor}^2 + H_{moor}^2}$ the line tension at the upper end, H_{moor} and V_{moor} the horizontal and vertical components of T_{moor} respectively at the upper end, φ the angle between the horizontal and tangent of the cable, and V_1 the vertical tension at the lower end.
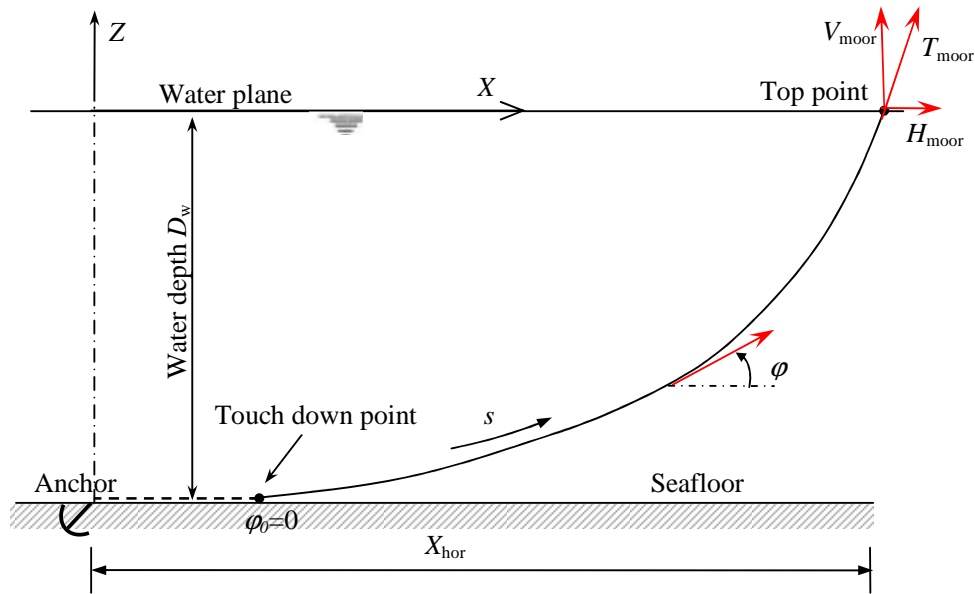
Figure 2.7. Static line characteristics

These catenary equations cannot be solved explicitly in almost every case. Aamo (1999) proposed an algorithm, namely the *shooting method*, to solve these equations for finding the configuration of a hanging cable submerged in water (Figure 2.7). The cable is supported by two fixed points; one on the sea floor (anchor point) and the other on the sea surface (top point). If the cable touches down on the seafloor at a point

other than the anchor point, this point is identified, and bottom friction forces act on the cable between the touchdown point and the anchor. Furthermore, the cable may consist of any number of segments, with individual characteristics, and clump weights (or buoys) are allowed between segments. Given the vertical force V_{moor} and the angle φ at the top point, the cable configuration is found by stepping through the segments from the top towards the anchor. Successive updates of V_{moor} and φ are performed until the anchor point hits the prescribed location defined by the water depth D_w and the horizontal displacement X_{hor}. The core algorithm can be summarized as follows (Aamo, 1999).

+ *Algorithm 1*: Steps are given as follows

    1. Given V_{moor} and φ at the top point, calculate H_{moor}, set $i = ns$, where *ns* is the number of segments.

    2. Based on V_{moor} and H_{moor}, calculate the horizontal and vertical displacement of segment *i* using the catenary equations given in (2.44) and (2.45).

    3. Update V_{moor} by subtracting the weight of segment *i*. If $i > 1$ go to step 2.

    4. Add up the displacements for all segments.

+ *Algorithm 2*: Depending on the result of Algorithm 1, V_{moor} and φ are adjusted one at a time. For given V_{moor}, a binary search is carried out on φ in order to hit the correct vertical displacement, which is the water depth D_w, as follows.

    1. Maximum angle φ_{max} is taken to be slightly less than 90°, and minimum angle is taken to be slightly more than 0°.

    2. Let $d = 0.5(\varphi_{max} - \varphi_{min})$. If *d* is less than an error tolerance, then stop. Otherwise set $\varphi = \varphi_{min} + d$, and perform Algorithm 1.

    3. If the vertical displacement is less than D_w, set $\varphi_{min} = \varphi$, otherwise set $\varphi_{max} = \varphi$. Go to step 2.

+ *Algorithm 3*: It remains to find V_{moor}, such that a binary search is again performed on V_{moor} until the horizontal displacement meets the prescribed value, which is the horizontal displacement X_{hor}, as follows.

    1. Take the total mass of the system as the initial guess for V_{moor}.

    2. Do Algorithm 2. If the resulting horizontal displacement is larger than X_{hor}, a touch down point is needed other than the anchor point, and the guess is upper bound. In this case, set $V_{max} = V_{moor}$ and V_{min} = the weight

of a piece of the upper end cable. Otherwise, the anchor point will have vertical load, and the guess is lower bound, that is $V_{\min} = V_{\text{moor}}$. In this case, increase V_{moor} by some percentage and do Algorithm 2 until the horizontal displacement is larger than X_{hor}. Set $V_{\max}$ to this value V_{moor}.

3. Let $d = 0.5(V_{\max} - V_{\min})$. If d is less than an error tolerance, then stop. Otherwise, set $V_{\text{moor}} = V_{\min} + d$.

4. Calculate the length of the suspended cable according to V_{moor}, and do Algorithm 2. Using the resulting horizontal tension at the bottom, calculate the length of the remaining part along the seafloor. Add the result to the horizontal displacement resulting from Algorithm 2.

5. If the horizontal is less than X_{hor}, set $V_{\min} = V_{\text{moor}}$. Otherwise, set $V_{\max} = V_{\text{moor}}$. Go to step 3.

The algorithms were written by Aamo (1999) in the C programming language and equipped with the MATLAB interface. Detailed algorithms and programs can be found in Aamo (1999). To verify the proposed method, Aamo (1999) compared the elastic catenary solutions to results from the MIMOSA program, which is a commercial program package of MARINTEK (SINTEF, Norway).

An example of line characteristics found by solving the catenary equations is illustrated in Figures 2.8 and 2.9. The mooring line consists of three segments in the water depth 380 m. Figure 2.8 shows the relationship given in (2.41), which obviously demonstrates the nonlinear relation of the line tension T_{moor}, its horizontal component H_{moor}, line length L_{m} and horizontal distance to the anchor X_{hor}. Two cases of line characteristics were carried out. In the first case as shown in the left of Figure 2.8, the horizontal distance to the anchor point X_{hor} was kept equal to 1234.5 m and the line characteristics (line tension T_{moor} and its horizontal component H_{moor}) were found through the catenary equations with various line lengths ($L_{\text{m}} = 1298$ m – 1445 m). In the second case as shown in the right of Figure 2.8, the line length L_{m} was kept equal to 1433 m and the line characteristics were solved with various horizontal distances to the anchor ($X_{\text{hor}} = 1084.5$ m – 1384.5 m). The profiles of the mooring line corresponding to these two cases are shown in Figure 2.9. The line profiles with various line lengths are plotted in the left of Figure 2.9 while the line profiles with various horizontal distances to the anchor are shown in the right of Figure 2.9.
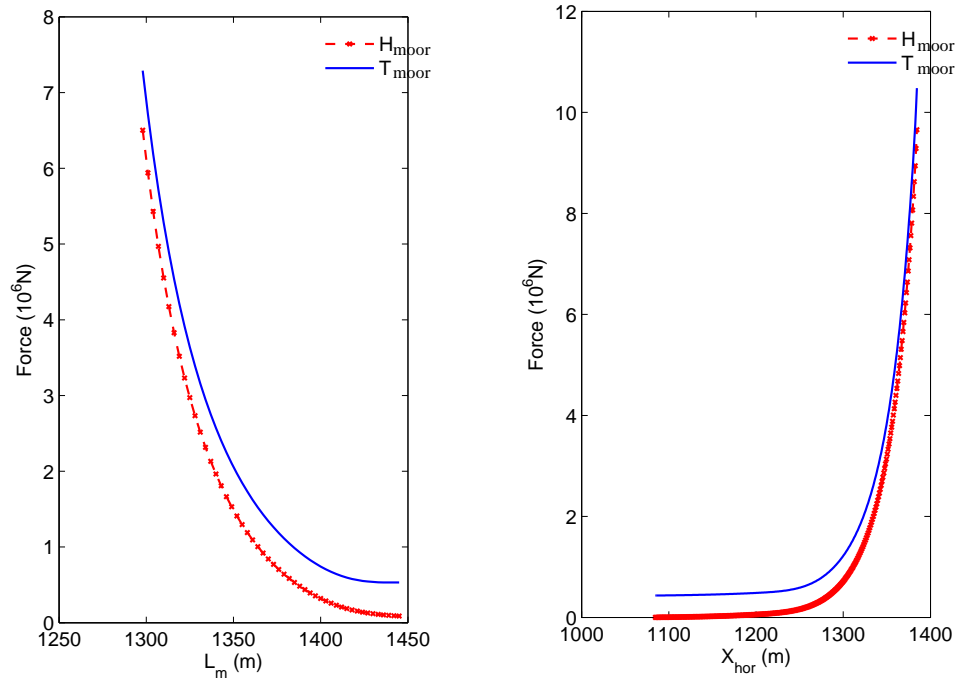
Figure 2.8. Line characteristics with line tension T_{moor} and its horizontal components H_{moor} at the top point as functions of line length L_m and horizontal distance to the anchor X_{hor}
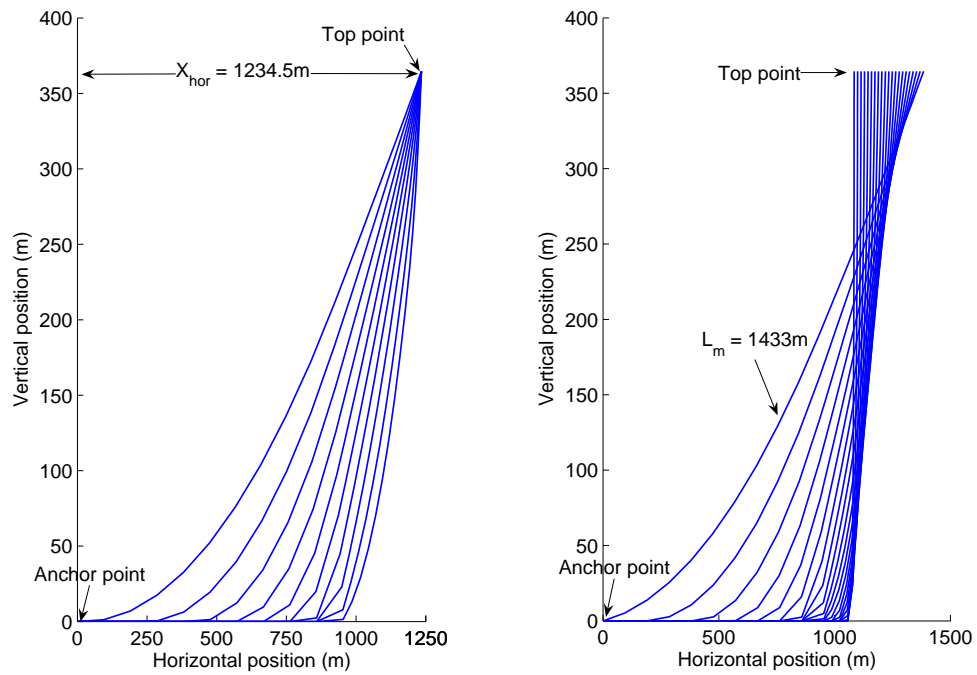
Figure 2.9. Line profiles with various line lengths L_m (left) and various horizontal distances to the anchor X_{hor} (right)

2.4.2 Restoring Force from Spread Mooring System

For convenience, the contribution of horizontal components of the line tension from all the lines can be assembled as a column vector, denoted as $\mathbf{H}_{\mathrm{moor}} = [H_{\mathrm{moor},i} \ldots H_{\mathrm{moor},N}]^{\mathrm{T}} \in \mathbb{R}^{N}$. As shown in Figure 2.10, the effect of the horizontal force component of mooring line i will produce an x, y and rotational component, which is related to the winch position ($\overline{x}_i$, $\overline{y}_i$) and planar angle β_i of the line given with respect to the Earth-fixed coordinate system, see Faltinsen (1990) and Strand et al. (1998) for more details. Hence, the effect of the mooring system on the surge, sway and yaw of the vessel is given by the column vector of restoring force $\mathbf{g}_{\mathrm{mo}} \in \mathbb{R}^{3}$ as

$$\mathbf{g}_{\mathrm{mo}} = \begin{bmatrix} g_{\mathrm{mo1}} & g_{\mathrm{mo2}} & g_{\mathrm{mo3}} \end{bmatrix}^{\mathrm{T}} = \sum_{i=1}^{N} \begin{bmatrix} H_{\mathrm{moor},i} \cos \beta_N \\ H_{\mathrm{moor},i} \sin \beta_N \\ H_{\mathrm{moor},i} (\overline{x}_i \sin \beta_i - \overline{y}_i \cos \beta_i) \end{bmatrix} \tag{2.46}$$

where N is the number of mooring lines. This can be re-written in compact form as

$$\mathbf{g}_{\mathrm{mo}} = \mathbf{T}(\boldsymbol{\beta}) \mathbf{H}_{\mathrm{moor}} \tag{2.47}$$

where $\mathbf{T}(\boldsymbol{\beta}) \in \mathbb{R}^{3 \times N}$ is the mooring line configuration matrix, given by

$$\mathbf{T}(\boldsymbol{\beta}) = \begin{bmatrix} \mathbf{t}_1, \ldots, \mathbf{t}_N \end{bmatrix} = \begin{bmatrix} \cos \beta_1 & \ldots & \cos \beta_N \\ \sin \beta_1 & \ldots & \sin \beta_N \\ \overline{x}_1 \sin \beta_1 - \overline{y}_1 \cos \beta_1 & \ldots & \overline{x}_N \sin \beta_N - \overline{y}_N \cos \beta_N \end{bmatrix} \tag{2.48}$$

in which $\boldsymbol{\beta} \in \mathbb{R}^{3}$ is the mooring line orientation vector comprising the moment arms ($\overline{x}_i$, $\overline{y}_i$) and the angle between the mooring line and the x-axis, β_i for $i = 1, \ldots, N$ (see Figure 2.10).
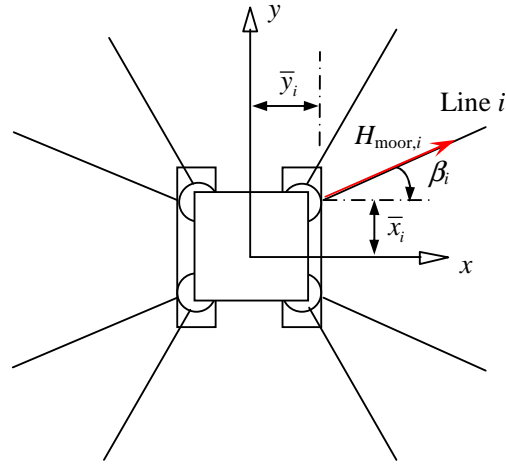
Figure 2.10. Spread mooring system of a platform

2.4.3 Total Contributions from Mooring System

Besides the restoring force, a mooring system as shown in Figure 2.11 also induces additional damping on the vessel motion, denoted as $\mathbf{D}_{mo} \in \mathbb{R}^{6\times6} = \text{diag}[d_{mo1}$ d_{mo2} 0 0 0 $d_{mo3}]$. This additional damping constitutes about 10 – 20% of critical damping of the entire system, depending on the water depth and the number of mooring lines (DNV, 2004). Therefore, a spread mooring model $\boldsymbol{\tau}_{moor} \in \mathbb{R}^{6}$ can be formulated in the body-fixed coordinate system as

$$\boldsymbol{\tau}_{moor} = -\mathbf{J}^{\mathrm{T}}\left(\boldsymbol{\eta}_2\right)\mathbf{G}_{mo}\left(\boldsymbol{\eta}\right) - \mathbf{D}_{mo}\left(\mathbf{v}\right) \tag{2.49}$$

where $\mathbf{J}(\boldsymbol{\eta}_2) \in \mathbb{R}^{6\times6}$ is the transformation matrix between the Earth- and body-fixed frames. In this study, it is assumed that a spread mooring system with symmetric pattern about the *xz*- and *yz*- plane only contributes forces in the horizontal plane (surge, sway and yaw). Hence, $\mathbf{G}_{mo} \in \mathbb{R}^{6\times6} = \text{diag}[g_{mo1} \ g_{mo2} \ 0 \ 0 \ 0 \ g_{mo3}]$, where g_{mo1}, g_{mo2} and g_{mo3} are three components of $\mathbf{g}_{mo}$ defined in (2.46). The damping component $\mathbf{D}_{mo}$ in (2.49) is usually added into the damping term of the LF vessel equation given in the next section.
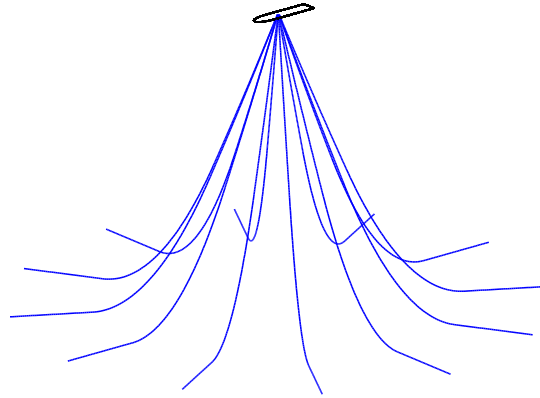
Figure 2.11. Typical spread mooring system

2.5   Model of Vessel Motion

In modelling the marine vessel dynamics, the ship motion is often decomposed into a wave frequency (WF) component riding on a low frequency (LF) component as shown in Figure 2.12. The WF motions are assumed to be caused by first-order wave loads whereas the LF motions are assumed to be caused by second-order mean and slowly varying wave loads, current loads, wind loads, mooring and thrust forces (Fossen, 2002; Sørensen, 2005b).
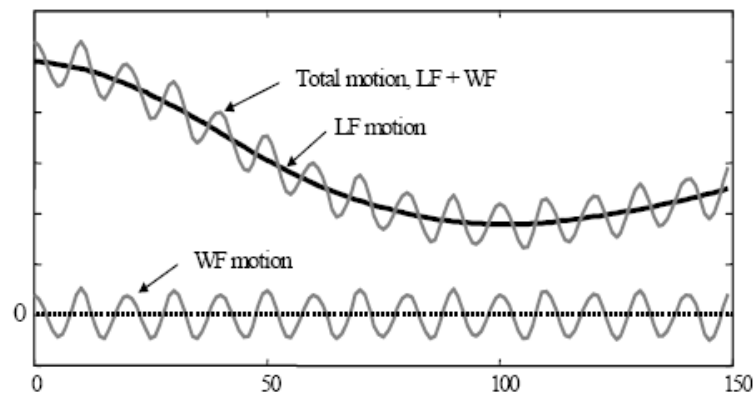
Figure 2.12. Total ship motion as sum of LF-motion and WF-motion

2.5.1 Low Frequency Vessel Model

The 6-DOF body-fixed coupled equations of the LF motions in surge, sway, heave, roll, pitch and yaw (see Figure 2.13) were formulated in the body-fixed frame by Fossen (2002) and Sørensen (2005b) as follows:

$$\mathbf{M}\dot{\mathbf{v}} + \mathbf{C}_{RB}(\mathbf{v})\mathbf{v} + \mathbf{C}_A(\mathbf{v}_r)\mathbf{v}_r + \mathbf{D}(\mathbf{v}_r) + \mathbf{G}(\boldsymbol{\eta}) = \boldsymbol{\tau}_{wave2} + \boldsymbol{\tau}_{wind} + \boldsymbol{\tau}_{moor} + \boldsymbol{\tau}_{thr} \qquad (2.50)$$

where $\mathbf{M} \in \mathbb{R}^{6\times6}$ is the system inertia matrix including added mass; $\mathbf{C}_{RB}(\mathbf{v}) \in \mathbb{R}^{6\times6}$ and $\mathbf{C}_A(\mathbf{v}_r) \in \mathbb{R}^{6\times6}$ the skew-symmetric Coriolis and centripetal matrices of the rigid body and the added mass; $\mathbf{D}(\mathbf{v}_r) \in \mathbb{R}^6$ the damping vector, which is a function of the relative velocity vector $\mathbf{v}_r$ between the vessel and current; $\mathbf{G}(\boldsymbol{\eta}) \in \mathbb{R}^6$ the generalized restoring vector caused the buoyancy and gravitation; $\boldsymbol{\tau}_{wave2}$, $\boldsymbol{\tau}_{wind}$ and $\boldsymbol{\tau}_{moor} \in \mathbb{R}^6$ the second-order wave load, wind load and mooring force vectors, respectively; and $\boldsymbol{\tau}_{thr} \in \mathbb{R}^6$ the vector consisting of forces and moments produced by the thruster system.
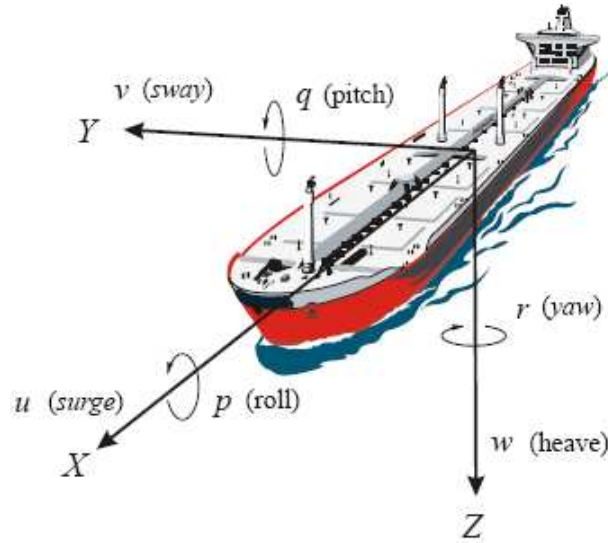
Figure 2.13. Definition of surge, sway, heave, roll, pitch and yaw modes of motion in body-fixed frame

2.5.1.1 Generalized Inertia Forces, $\mathbf{M}\dot{\mathbf{v}}$

The system inertia matrix $\mathbf{M} \in \mathbb{R}^{6\times6}$ including added mass is defined as

$$\mathbf{M} = \begin{bmatrix} m - X_{\dot{u}} & 0 & -X_{\dot{w}} & 0 & mz_G - X_{\dot{q}} & 0 \\ 0 & m - Y_{\dot{v}} & 0 & -mz_G - Y_{\dot{p}} & 0 & mx_G - Y_{\dot{r}} \\ -Z_{\dot{u}} & 0 & m - Z_{\dot{w}} & 0 & -mx_G - Z_{\dot{q}} & 0 \\ 0 & -mz_G - K_{\dot{v}} & 0 & I_x - K_{\dot{p}} & 0 & -I_{xz} - K_{\dot{r}} \\ mz_G - M_{\dot{u}} & 0 & -mx_G - M_{\dot{w}} & 0 & I_y - M_{\dot{q}} & 0 \\ 0 & mx_G - N_{\dot{v}} & 0 & -I_{zx} - N_{\dot{p}} & 0 & I_z - N_{\dot{r}} \end{bmatrix} \quad (2.51)$$

where m is the vessel mass; I_x, I_y and I_z the moments of inertia about the x-, y- and z-axes; $I_{xz} = I_{zx}$ the products of inertia and x_G, z_G the coordinates of the center of gravity in the body-fixed frame. If the origin of this frame is chosen to coincide with the center of gravity, then $x_G = z_G = 0$. The zero-frequency added mass coefficients $X_{\dot{u}}$, $X_{\dot{w}}$, $X_{\dot{q}}$, $Y_{\dot{v}}$, $Y_{\dot{p}}$, $Y_{\dot{r}}$, $Z_{\dot{u}}$, $Z_{\dot{w}}$, $Z_{\dot{q}}$, $K_{\dot{v}}$, $K_{\dot{p}}$, $K_{\dot{r}}$, $M_{\dot{u}}$, $M_{\dot{w}}$, $M_{\dot{q}}$, $N_{\dot{v}}$, $N_{\dot{p}}$, and $N_{\dot{r}}$ at low speed in surge, sway, heave, roll, pitch and yaw due to accelerations along the corresponding and the coupled axes are defined as in Faltinsen (1990). These coefficients are dependent on the vessel geometry and the frequency of vessel motions. They are normally computed through commercial software such as WAMIT (Faltinsen, 1990), which is a computer program based on a three dimensional panel method for analyzing hydro dynamic interactions with floating or submerged bodies in the presence of waves using potential theory.

2.5.1.2 Generalized Coriolis and Centripetal Forces, $\mathbf{C}_{RB}(\mathbf{v})\mathbf{v} + \mathbf{C}_A(\mathbf{v}_r)\mathbf{v}_r$

The matrix $\mathbf{C}_{RB}(\mathbf{v}) \in \mathbb{R}^{6\times6}$ is the skew-symmetric Coriolis and centripetal matrix, written as (Fossen, 2002).

$$\mathbf{C}_{RB}(\mathbf{v}) = \begin{bmatrix} 0 & 0 & 0 & c_{41} & -c_{51} & -c_{61} \\ 0 & 0 & 0 & -c_{42} & -c_{52} & -c_{62} \\ 0 & 0 & 0 & -c_{43} & -c_{53} & -c_{63} \\ -c_{41} & c_{42} & c_{43} & 0 & -c_{54} & -c_{64} \\ c_{51} & -c_{52} & c_{53} & c_{54} & 0 & -c_{65} \\ c_{61} & c_{62} & -c_{63} & c_{64} & c_{65} & 0 \end{bmatrix} \quad (2.52)$$

where

$$c_{41} = mz_G r \qquad c_{42} = mw \qquad c_{43} = m(z_G p - v)$$

$$c_{51} = m(x_G q - w) \quad c_{52} = m(z_G r + x_G p) \quad c_{53} = m(z_G q + u) \quad c_{54} = I_{xz} p - I_z r$$

$$c_{61} = m(v + x_G r) \quad c_{62} = -mu \qquad c_{63} = mx_G p \qquad c_{64} = I_y q$$

$$c_{65} = I_x p + I_{xz} r$$

$$(2.53)$$

The effect of current is divided into a potential and a viscous component (Wichers, 1993). The viscous part is included in the nonlinear damping term of $\mathbf{D}(\mathbf{v}_r)$ in (2.50). The potential part of the current load is modeled in the Coriolis and centripetal matrix of the added mass $\mathbf{C}_A(\mathbf{v}_r) \in \mathbb{R}^{6 \times 6}$ as follows

$$\mathbf{C}_A(\mathbf{v}_r) = \begin{bmatrix} 0 & 0 & 0 & 0 & -c_{a51} & -c_{a61} \\ 0 & 0 & 0 & -c_{a42} & 0 & -c_{a62} \\ 0 & 0 & 0 & -c_{a43} & -c_{a53} & 0 \\ 0 & c_{a42} & c_{a43} & 0 & -c_{a54} & -c_{a64} \\ c_{a51} & 0 & c_{a53} & c_{a54} & 0 & -c_{a65} \\ c_{a61} & c_{a62} & 0 & c_{a64} & c_{a65} & 0 \end{bmatrix} \tag{2.54}$$

where

$$c_{a42} = -Z_{\dot{w}}w - Z_{\dot{w}}u_r - Z_{\dot{q}}q \quad c_{a43} = Y_{\dot{p}}p + Y_{\dot{v}}v_r + Y_{\dot{r}}r$$

$$c_{a51} = Z_{\dot{q}}q + Z_{\dot{w}}w + X_{\dot{w}}u_r \quad c_{a53} = -X_{\dot{q}}q - X_{\dot{u}}u_r - X_{\dot{w}}w \quad c_{a54} = Y_{\dot{r}}v_r + K_{\dot{p}}p + N_{\dot{r}}r$$

$$c_{a61} = -Y_{\dot{v}}v_r - Y_{\dot{p}}p - Y_{\dot{r}}r \quad c_{a62} = X_{\dot{u}}u_r + X_{\dot{w}}w + X_{\dot{q}}q \quad c_{a64} = X_{\dot{q}}u_r + Z_{\dot{q}}w + M_{\dot{q}}q$$

$$c_{a65} = Y_{\dot{v}}v_r + K_{\dot{v}}p + K_{\dot{r}}r$$

$$(2.55)$$

The relative velocity vector between the vessel and current $\mathbf{v}_r \in \mathbb{R}^6$ is defined as

$$\mathbf{v}_r = \begin{bmatrix} u_r & v_r & w & p & q & r \end{bmatrix}^T = \begin{bmatrix} u - u_c & v - v_c & w & p & q & r \end{bmatrix}^T \tag{2.56}$$

where u_c and v_c are the horizontal surge and sway components of the current, which are calculated from the current velocity V_c and direction β_c as follows

$$u_c = V_c \cos(\beta_c - \psi)$$

$$v_c = V_c \sin(\beta_c - \psi)$$

$$(2.57)$$

2.5.1.3 Generalized Damping and Current Forces, $\mathbf{D}(\mathbf{v}_r)$

The damping vector may be divided into a linear and a nonlinear component according to

$$\mathbf{D}(\mathbf{v}_r) = \mathbf{D}_L \mathbf{v}_r + \mathbf{d}_{NL}(\mathbf{v}_r, \gamma_r) \tag{2.58}$$

For vessel velocities close to zero, linear damping becomes more significant than nonlinear damping. The strictly positive linear damping matrix $\mathbf{D}_L$ caused by linear wave drift damping and the laminar skin friction can be written as

$$\mathbf{D}_L = -\begin{bmatrix} X_u & 0 & X_w & 0 & X_q & 0 \\ 0 & Y_v & 0 & Y_p & 0 & Y_r \\ Z_u & 0 & Z_w & 0 & Z_q & 0 \\ 0 & K_v & 0 & K_p & 0 & K_r \\ M_u & 0 & M_w & 0 & M_q & 0 \\ 0 & N_v & 0 & N_p & 0 & N_r \end{bmatrix}$$

(2.59)

The damping coefficients in (2.59) can be found by model tests or a special software such as WAMIT (Faltinsen, 1990).

The nonlinear damping is assumed to be caused by turbulent skin friction and viscous eddy-making, also described as vortex shedding (Faltinsen, 1990). Assuming small vertical motion, the 6-dimensional nonlinear damping vector is often written as

$$\mathbf{d}_{NL} = 0.5\rho_w L_{pp} \begin{bmatrix} DC_{cx}(\gamma_r)|U_{cr}|U_{cr} \\ DC_{cy}(\gamma_r)|U_{cr}|U_{cr} \\ BC_{cz}(\gamma_r)|w|w \\ B^2 C_{c\phi}(\gamma_r)|p|p + z_{py}DC_{cy}(\gamma_r)|U_{cr}|U_{cr} \\ L_{pp}BC_{c\theta}(\gamma_r)|q|q + z_{px}DC_{cx}(\gamma_r)|U_{cr}|U_{cr} \\ L_{pp}DC_{c\psi}(\gamma_r)|U_{cr}|U_{cr} \end{bmatrix}$$

(2.60)

where ρ_w is the density of water; L_{pp} the length between the ship perpendiculars; D the draft of vessel; B the breadth of vessel; $C_{cx}(\gamma_r)$, $C_{cy}(\gamma_r)$, $C_{cz}(\gamma_r)$, $C_{c\phi}(\gamma_r)$, $C_{c\theta}(\gamma_r)$ and $C_{c\psi}(\gamma_r)$ are the non-dimensional drag coefficients estimated from model tests for the specific vessel under consideration (defined at specified location of the origin); U_{cr} the total relative current vector; and γ_r the relative drag angle. It should be noted that the viscous component of the effect of current is included here through the relative current vector. The second contributions to roll and pitch are the moments caused by the nonlinear damping and current forces in surge and sway, respectively, acting at the corresponding centers of pressure located at z_{py} and z_{px}. The total relative current vector is given by

$$U_{cr} = \sqrt{u_r^2 + v_r^2}$$

(2.61)

The relative drag angle is found from the following relation

$$\gamma_{\mathrm{r}} = \mathrm{atan}\, 2(-v_{\mathrm{r}}, -u_{\mathrm{r}}) \tag{2.62}$$

where atan2 is the four quadrant arctangent function of the real parts of the elements of X and Y, such that $-\pi \leq \mathrm{atan2}(Y, X) \leq \pi$; u_{r} and v_{r} are defined in (2.56).

2.5.1.4 *Generalized Restoring Forces,* $\mathbf{G}(\mathbf{\eta})$

According to Faltinsen (1990), when a body is freely floating, the restoring forces will be defined from hydrostatic and mass considerations. They are equivalent to the spring forces in a *mass-damper-spring* system. For the boxed shaped surface vessel used in this study, it is common to assume that the roll and pitch angles are small, such that the restoring vector in (2.50) can be linearized to $\mathbf{G}_{\mathrm{L}}\mathbf{\eta}$, where $\mathbf{G}_{\mathrm{L}} \in \mathbb{R}^{6 \times 6}$ is a matrix of linear generalized gravitation and buoyancy force coefficients, written as

$$\mathbf{G}_{\mathrm{L}} = -\begin{bmatrix} 0 & 0 & 0 & 0 & 0 & 0 \\ 0 & 0 & 0 & 0 & 0 & 0 \\ 0 & 0 & Z_z & 0 & Z_\theta & 0 \\ 0 & 0 & 0 & K_\phi & 0 & 0 \\ 0 & 0 & M_z & 0 & M_\theta & 0 \\ 0 & 0 & 0 & 0 & 0 & 0 \end{bmatrix} \tag{2.63}$$

where the coefficients are defined in Faltinsen (1990) as

$$Z_z = -\rho_{\mathrm{w}} g A_{\mathrm{WP}} \tag{2.64}$$

$$Z_\theta = M_z = \rho_{\mathrm{w}} g \iint\limits_{A_{\mathrm{WP}}} x dA \tag{2.65}$$

$$K_\phi = -\rho_{\mathrm{w}} g V (z_{\mathrm{G}} - z_{\mathrm{B}}) - \rho_{\mathrm{w}} g \iint\limits_{A_{\mathrm{WP}}} y^2 dA = -\rho_{\mathrm{w}} g V \overline{GM_{\mathrm{T}}} \tag{2.66}$$

$$M_\theta = -\rho_{\mathrm{w}} g V (z_{\mathrm{G}} - z_{\mathrm{B}}) - \rho_{\mathrm{w}} g \iint\limits_{A_{\mathrm{WP}}} x^2 dA = -\rho_{\mathrm{w}} g V \overline{GM_{\mathrm{L}}} \tag{2.67}$$

in which ρ_{w} is the density of water, g the acceleration due to gravity, A_{WP} the water plane area, $dA = dxdy$, z_{G} the z-coordinate of the centre of gravity, z_{B} the z-coordinate of the centre of buoyancy, V the displaced volume of water, and $\overline{GM_{\mathrm{T}}}$ and $\overline{GM_{\mathrm{L}}}$ the transverse and longitudinal meta-centric heights, respectively.

2.5.1.5 Environmental Loads

Wind Load $\boldsymbol{\tau}_{\text{wind}}$: The effects of wind may be divided into a mean, slowly-varying component and a rapidly-varying component. If the relative wind velocity is defined as

$$\mathbf{v}_{\text{rw}} = \left[u_{\text{rw}}, v_{\text{rw}}, w, p, q, r\right]^{\text{T}} = \left[u - u_{\text{w}}, v - v_{\text{w}}, w, p, q, r\right]^{\text{T}} \tag{2.68}$$

where u_{w} and v_{w} are components of wind velocities, defined as

$$u_{\text{w}} = V_{\text{w}}\cos(\beta_{\text{w}} - \psi), \ v_{\text{w}} = V_{\text{w}}\sin(\beta_{\text{w}} - \psi), \tag{2.69}$$

in which V_{w} is wind velocity, β_{w} wind direction, then the total relative wind velocity is given by

$$U_{\text{wr}} = \sqrt{u_{\text{rw}}^2 + v_{\text{rw}}^2} \tag{2.70}$$

The wind load is given by (Fossen, 2002)

$$\boldsymbol{\tau}_{\text{wind}} = 0.5\rho_{\text{a}} \begin{bmatrix} A_x C_{\text{wx}}(\gamma_{\text{w}})\left|U_{\text{rw}}\right|U_{\text{rw}} \\ A_y C_{\text{wy}}(\gamma_{\text{w}})\left|U_{\text{rw}}\right|U_{\text{rw}} \\ 0 \\ A_y L_{yz} C_{\text{wx}}(\gamma_{\text{w}})\left|U_{\text{rw}}\right|U_{\text{rw}} \\ -A_x L_{xz} C_{\text{wx}}(\gamma_{\text{w}})\left|U_{\text{rw}}\right|U_{\text{rw}} \\ A_y L_{\text{oa}} C_{\text{w}\psi}(\gamma_{\text{w}})\left|U_{\text{rw}}\right|U_{\text{rw}} \end{bmatrix} \tag{2.71}$$

where ρ_{a} is the density of air; A_x and A_y the lateral and longitudinal areas of the non-submerged part of the ship projected on the *xz*-plane and *yz*-plane; L_{oa} the overall length of vessel; L_{xz} and L_{yz} the vertical distances between transverse and longitudinal origin and the wind load centre of attack; $\gamma_{\text{w}} = \beta_{\text{w}} - \psi$ the relative wind angle; and $C_{\text{wx}}(\gamma_{\text{w}})$, $C_{\text{wy}}(\gamma_{\text{w}})$, and $C_{\text{w}\psi}(\gamma_{\text{w}})$ the non-dimensional wind coefficients in surge, sway and yaw respectively. These coefficients are often found by model testing or by semi-empirical formulas as presented in Isherwood (1972).

Second-order Wave Load $\boldsymbol{\tau}_{\text{wave2}}$: The wave drift loads contribute significantly to the total excitation force in the LF model. The second-order wave effects include mean loads, slowly-varying loads due to frequency difference and rapidly-varying wave loads due to frequency summation. The effects of rapidly-varying wave loads can be neglected for positioning control application. According to Faltinsen and Løken (1979) and Faltinsen (1990), the second-order wave force $\boldsymbol{\tau}_{wave2} \in \mathbb{R}^6$ can be approximated as a

summation of second-order 'transfer' functions of difference frequency wave components as

$$\tau_{wave2}^{i} = \sum_{j=1}^{N}\sum_{k=1}^{N} A_j A_k [T_{jk}^{\text{ic}} \cos((\omega_k - \omega_j)t + (\varepsilon_k - \varepsilon_j)) + T_{jk}^{\text{is}} \sin((\omega_k - \omega_j)t + (\varepsilon_k - \varepsilon_j))] \quad (2.72)$$

where $i = 1 - 6$ represents six components of $\boldsymbol{\tau}_{wave2}$, $\omega_{j,k}$ are the wave frequencies, $\varepsilon_{j,k}$ random phase angles, N the number of wave components considered; $A_{j,k} = \sqrt{2S(\omega_{j,k})\Delta\omega}$ the wave amplitudes determined from the wave spectrum $S(\omega)$; $\Delta\omega = (\omega_{\max} - \omega_{\min})/N$; and T_{jk}^{ic} and T_{jk}^{is} can be interpreted as second-order transfer functions for the difference frequency loads. Detailed calculations of the second-order wave load can be found in Faltinsen and Løken (1979) and Faltinsen (1990).

The wind and wave drift coefficients given in (2.71) and (2.72) are either found by model tests or computed by a dedicated and well recognized software package such as WAMIT (Faltinsen, 1990).

2.5.2 Linear Wave-frequency Vessel Model

In the mathematical modelling of vessel dynamics, it is common to separate the modelling into a LF model and WF model. However, vessel motions are not separated into the LF part and WF part in practice. Hence it is convenient to use both the LF and WF models, which are detailed enough to describe the main physical characteristics of the dynamic system. In vessel motion control systems, the position signals used in the feedback controller should not contain the WF part of the motion. In this case, the WF model is essential for studying wave filtering of control systems. According to Sørensen (2005b), the coupled equations of the WF motions in surge, sway, heave, roll, pitch and yaw are assumed to be linear, and can be formulated as

$$\mathbf{M}(\omega)\ddot{\boldsymbol{\eta}}_{\text{Rw}} + \mathbf{D}_{\text{p}}(\omega)\dot{\boldsymbol{\eta}}_{\text{Rw}} + \mathbf{G}\boldsymbol{\eta}_{\text{Rw}} = \boldsymbol{\tau}_{\text{wave1}} \tag{2.73}$$

$$\dot{\boldsymbol{\eta}}_{\text{w}} = \mathbf{J}(\bar{\boldsymbol{\eta}}_2)\dot{\boldsymbol{\eta}}_{\text{Rw}} \tag{2.74}$$

where $\boldsymbol{\eta}_{\text{Rw}} \in \mathbb{R}^6$ is the WF motion vector in the reference-parallel frame; $\boldsymbol{\eta}_{\text{w}} \in \mathbb{R}^6$ the WF motion vector in the Earth-fixed frame; $\bar{\boldsymbol{\eta}}_2 = \begin{bmatrix} 0 & 0 & \psi_{\text{d}} \end{bmatrix}^{\text{T}}$; $\boldsymbol{\tau}_{\text{wave1}} \in \mathbb{R}^6$ the first order wave excitation vector, which will be modified for varying vessel headings relative to the incident wave direction; $\mathbf{M}(\omega) \in \mathbb{R}^{6\times6}$ the system inertia matrix containing frequency dependent added mass coefficients in addition to the vessel's mass and moment of inertia; and $\mathbf{D}_{\text{p}} \in \mathbb{R}^{6\times6}$ the wave radiation (potential) damping matrix. The

linearized restoring coefficients matrix $\mathbf{G} \in \mathbb{R}^{6 \times 6}$ is due to gravity and buoyancy affecting heave, roll and pitch only. For anchored vessels, it is assumed that the mooring system will not influence the WF motions (Triantafyllou, 1990).

2.6   Concluding Remarks

The mathematical models of the riser, mooring system and vessel are presented in this chapter. In Chapter 3, the model of vessel-mooring-riser system given by (2.33), (2.49), (2.50) and (2.73) are used to propose a new control concept for minimizing the REAs in open water. These models are then used to study bending stresses of the riser in Chapter 4. In Chapter 5, the riser, mooring system and LF vessel models given by (2.33), (2.49) and (2.50) are used to examine the proposed control strategy in ice-covered sea.

CHAPTER 3. CONTROL OF RISER END ANGLES BY POSITION MOORING

3.1   Introduction

For normal drilling and work-over operations, the main objective is to minimize the rigid riser angles at the well-head and at the top joint. One way to realize this is to control the vessel's position. Shallow water drilling operations are normally carried out with a moored vessel. Under unfavourable environmental condition and with fixed lengths of mooring lines, the equilibrium position, which a PM vessel without control intervention moves to, may cause large riser end angle responses. Line tensioning control may be employed to reduce the end angles whenever possible as it consumes less energy than control using thrusters only.

This chapter mainly focuses on the control of marine riser end angles in PM system by adjusting the vessel's position through changing the lengths of mooring lines and controlling the vessel's heading by thruster assistance. The detailed structure of this control strategy is presented and its suitability verified through numerical simulations and experimental tests of a moored vessel.

3.2   Measurement of Top and Bottom Riser Angles

The vertical angles of the marine riser at the top and bottom joint are critical to the drilling operation because the drill string may wear against the pipe wall due to large angles with respect to vertical axis at these joints. Angle sensors such as inclinometers are installed on the riser next to the end joints for continuous monitoring during drilling operations. The angular information is also used by the riser angle position reference system to calculate the vessel offset from the wellhead (Figure 3.1). This system uses both the top riser angle (at the slip joint) and the bottom riser angle (at the ball joint) and the pre-programmed riser characteristics to adaptively compensate for the riser dynamics and provide the vessel offset estimates (API, 1998).

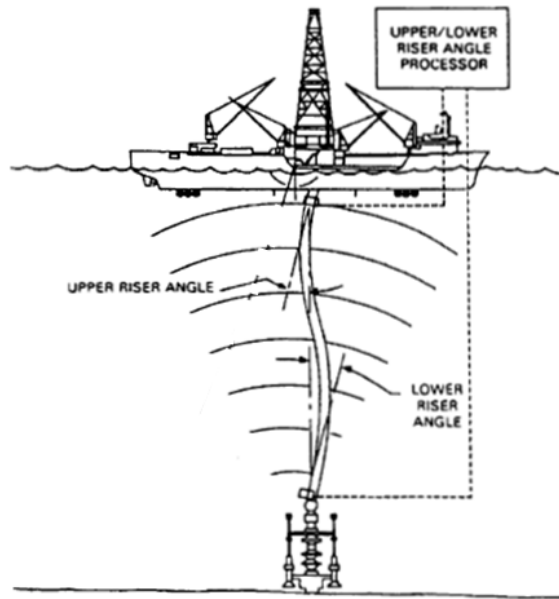Figure 3.1. Adaptive Riser Angle Reference System (API, 1998)

3.3   Structure of Control System

The structure of a real-time marine control system proposed by Sørensen (2005a) is given in Figure 3.2. Under individual vessel operational management, local optimization is done through high level plant control and low level actuator control.
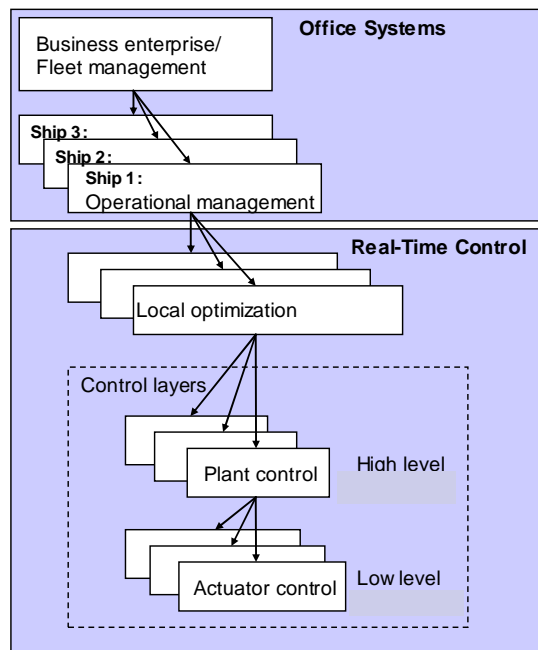
Figure 3.2. Real-time control structure (Sørensen, 2005a)

Low Level Actuator Control: Low level control can be realized by the common actuators in marine systems such as propellers, thrusters, rudders, stabilizing fins and mooring systems. Local control of propellers and thrusters may be done by controlling the speed (*rpm*), pitch, torque, and power or combination of these. For mooring systems, this can be implemented by changing the lengths of the mooring lines.

High Level Plant Control: In station keeping operations, the positioning system is supposed to counteract the disturbances caused by wave (mean and slowly varying), wind and current load acting on the vessel. The plant controller calculates the commanded surge and sway forces and yaw moment needed to compensate the disturbances. The actuator control then determines the command action of each actuator to implement such forces and moment (e.g., thrust allocation in DP system).

Local Optimization: Depending on the actual marine operations (such as gas transportation, drilling and pipe laying) that the vessel is involved, optimization of desired set-point is performed in conjunction with an appropriate reference model.

3.4   Control Plant Model of Vessel and Riser

For controller design, the characteristic of the dynamic system must be known and the response in the operating environment assessed. The optimal means is to use a simplified model of the system that is detailed enough to describe the main physical characteristics of the system. Such a model is known as *control plant model*. In this section, the control plant models of the vessel and the riser will be derived by simplifying the process plant models presented in Chapter 2. Since the riser considered in this study is operating in shallow water, a simplification of the riser model described by (2.37) will be used to obtain the relationship between the angular riser response and vessel offset. The riser angle control plant model includes the flexural bending stiffness that may be significant in shallow water.

3.4.1 Control Plant Model of Vessel

As shown in Chapter 2, due to the range of frequency content exhibited by the environmental disturbances, the modelling of marine vessel is separated into a LF model and a WF model. The LF model features the wave drift, wind and current loads while the WF model accounts for the first-order wave loads.

LF control plant model: For the purpose of model-based controller design it is convenient to derive a simplified mathematical model, which nevertheless is detailed enough to include the main physical characteristics of the dynamic system. In station keeping, it can be assumed that the vessel velocities are small. Hence, $\mathbf{C}_{\mathrm{RB}}$ and $\mathbf{C}_{\mathrm{A}}$ approximate to 0; and $\mathbf{D}_{\mathrm{L}}$, which is caused by linear wave drift damping and laminar, is considerably larger than $\mathbf{D}_{\mathrm{NL}}$ (Sørensen et al., 1999). Based on these simplifications, $\mathbf{C}_{\mathrm{RB}}(\mathbf{v})\mathbf{v}$, $\mathbf{C}_{\mathrm{A}}(\mathbf{v}_{\mathrm{r}})\mathbf{v}_{\mathrm{r}}$ and $\mathbf{d}_{\mathrm{NL}}(\mathbf{v}_{\mathrm{r}},\gamma_{\mathrm{r}})$ are negligible in the LF model (2.50). Neglecting heave, roll and pitch motions and considering only surge, sway and yaw motions (in-plane motions), the nonlinear LF control plant model is given by (Sørensen, 2005b).

$$\mathbf{M}\dot{\mathbf{v}} + \mathbf{D}\mathbf{v} = \boldsymbol{\tau}_{\mathrm{c}} + \mathbf{R}^{\mathrm{T}}(\psi)\mathbf{b} \qquad (3.1)$$

where $\mathbf{v} = \begin{bmatrix} u & v & r \end{bmatrix}^{\mathrm{T}}$, $\boldsymbol{\tau}_{\mathrm{c}} \in \mathbb{R}^{3}$ is the control input including control forces of mooring lines $\boldsymbol{\tau}_{\mathrm{cmoor}} \in \mathbb{R}^{3}$ and thrusters $\boldsymbol{\tau}_{\mathrm{thr}} \in \mathbb{R}^{3}$, $\mathbf{R}(\psi) \in \mathbb{R}^{3\times3}$ the rotation matrix introduced in (2.6), and $\mathbf{b} \in \mathbb{R}^{3}$ the bias vector describing the slowly-varying environmental forces and moment due to second-order wave loads, current and wind. Notice that the control plant model is nonlinear because of the rotation matrix $\mathbf{R}(\psi)$. $\mathbf{M}$ and $\mathbf{D} \in \mathbb{R}^{3\times3}$ are given as

$$\mathbf{M} = \begin{bmatrix} m - X_{\dot{u}} & 0 & 0 \\ 0 & m - Y_{\dot{v}} & mx_{\mathbf{G}} - Y_{\dot{r}} \\ 0 & mx_{\mathbf{G}} - N_{\dot{v}} & I_{z} - N_{\dot{r}} \end{bmatrix} \qquad (3.2)$$

$$\mathbf{D} = \mathbf{D}_{\mathrm{L}} + \mathbf{D}_{\mathrm{mo}} = \begin{bmatrix} -X_{u} + d_{\mathrm{mo1}} & 0 & 0 \\ 0 & -Y_{v} + d_{\mathrm{mo2}} & -Y_{r} \\ 0 & -N_{v} & -N_{r} + d_{\mathrm{mo3}} \end{bmatrix} \qquad (3.3)$$

The damping effect of the mooring system $\mathbf{D}_{\mathrm{mo}}$ is included in the damping matrix $\mathbf{D}$. The parameters in (3.2) and (3.3) are defined in Sections 2.4 and 2.5 of Chapter 2.

A first-order *Markov* model is frequently used to model the bias for marine control applications, written as (Fossen and Strand, 1999)

$$\dot{\mathbf{b}} = -\mathbf{T}_{\mathrm{b}}^{-1}\mathbf{b} + \mathbf{E}_{\mathrm{b}}\mathbf{w}_{\mathrm{b}} \qquad (3.4)$$

where $\mathbf{T}_{\mathrm{b}} \in \mathbb{R}^{3\times3}$ is a user specified diagonal matrix of bias time constants, $\mathbf{E}_{\mathrm{b}} \in \mathbb{R}^{3\times3}$ a diagonal scaling matrix, and $\mathbf{w}_{\mathrm{b}} \in \mathbb{R}^{3}$ a zero-mean Gaussian white noise vector.

The kinematics and the state vectors in (2.6) are used to obtain the transformation between the Earth-fixed and body-fixed frame,

$$\dot{\boldsymbol{\eta}} = \mathbf{R}(\psi)\mathbf{v} \tag{3.5}$$

WF control plant model: The control plant model for the WF model is obtained by assuming (2.73) to be a second-order linear model driven by white noise, given by Sørensen (2005b). The WF control plant model is essential for the design of wave filtering.

$$\dot{\mathbf{p}}_w = \mathbf{A}_w\mathbf{p}_w + \mathbf{E}_w\mathbf{w}_w \tag{3.6}$$

$$\boldsymbol{\eta}_w = \mathbf{C}_w\mathbf{p}_w \tag{3.7}$$

where $\boldsymbol{\eta}_w \in \mathbb{R}^3$ is the position and orientation measurement vector, $\mathbf{w}_w \in \mathbb{R}^3$ zero-mean Gaussian white noise vector, and $\mathbf{p}_w \in \mathbb{R}^6$ the state of WF model. The system matrix $\mathbf{A}_w \in \mathbb{R}^{6\times6}$, the disturbance matrix $\mathbf{E}_w \in \mathbb{R}^{6\times3}$ and the measurement matrix $\mathbf{C}_w \in \mathbb{R}^{3\times6}$ may be formulated as (Fossen, 2002)

$$\mathbf{A}_w = \begin{bmatrix} \mathbf{0}_{3\times3} & \mathbf{I}_{3\times3} \\ -\boldsymbol{\Omega}^2 & -2\boldsymbol{\Lambda}\boldsymbol{\Omega} \end{bmatrix} \tag{3.8}$$

$$\mathbf{C}_w = \begin{bmatrix} \mathbf{0}_{3\times3} & \mathbf{I}_{3\times3} \end{bmatrix} \tag{3.9}$$

$$\mathbf{E}_w = \begin{bmatrix} \mathbf{0}_{3\times3} \\ \mathbf{K}_w \end{bmatrix} \tag{3.10}$$

where $\boldsymbol{\Omega} = \text{diag}\{\omega_1, \omega_2, \omega_3\}$, $\boldsymbol{\Lambda} = \text{diag}\{\zeta_1, \zeta_2, \zeta_3\}$, $\mathbf{K}_w = \text{diag}\{K_{w1}, K_{w2}, K_{w3}\}$, ω_i ($i = 1,2,3$) is the dominating wave frequency, ζ_i ($i = 1,2,3$) the relative damping ratio and K_{wi} ($i = 1,2,3$) a parameter related to the wave intensity. Typically, the wave periods T_i are in the range of 5 to 20 s in North Sea for wind generated seas. The relative damping ratio ζ_i will be in the range 0.05 – 0.10 (Sørensen, 2005b). According to Grimble and Johnson (1988), a linear second-order WF model is considered to be sufficient for representing the WF-induced motions. Fossen and Strand (1999) and Sørensen (2005a) employed this model and concluded that it is accurate enough to model the WF-induced motions. Higher order wave transfer function approximations can also be used in Grimble et al. (1980) and Fung and Grimble (1983). According to Fossen and Strand (1999) and Fossen (1994), the main reason for choosing higher order of the WF model is that a more precise approximation to the actual wave spectrum, e.g. the

67

JONSWAP spectra can be obtained. However, this also increases the number of model parameters to be determined and the dimension of observer gain matrices.

The output of the control plant model, $\mathbf{y} \in \mathbb{R}^3$, is the position and heading of the vessel, assumed to be a superposition of the LF and WF motion, as follows

$$\mathbf{y} = \boldsymbol{\eta} + \boldsymbol{\eta}_w \tag{3.11}$$

3.4.2 Control Plant Model of Riser Angles

In order to minimize the REAs by vessel positioning, the control scheme must be implemented according to the riser angle response criterion to provide a set-point to effect an optimal position of the vessel. The use of such set-point function has been proposed by Sørensen et al. (2001). Using the riser finite element method (FEM) model, the vessel offset position can be obtained as a function of the REAs.

The riser in this study is applicable for shallow water where its natural periods are lower than 25 seconds, whereas the LF range of the vessel in surge and sway is around 1 – 2 minutes. For simplicity, it is assumed that the natural periods of the riser are located away from the LF range (Sørensen et al., 2001). Thus the damping and inertia terms can be neglected in (2.37) and (2.38). Such assumption is acceptable for shallow water application. In deep water, dynamic effects will become more important since the lowest frequency of the riser may approach the LF range. Based on the riser FEM model (given in (2.36)), the incremental change in riser displacement vector $\Delta \mathbf{r}_A$ is related to the in-plane increment in surface vessel position vector $\Delta \mathbf{r}_B$ as follows

$$\Delta \mathbf{r}_A = -\mathbf{K}_{AA}^{-1} \mathbf{K}_{AB} \Delta \mathbf{r}_B \tag{3.12}$$

where $\Delta \mathbf{r}_A$ and $\Delta \mathbf{r}_B$ are obtained from (2.39) and (2.40) as

$$\Delta \mathbf{r}_A = \begin{bmatrix} \Delta \alpha_1 & \Delta x_2 & \Delta y_2 & \Delta \alpha_2 & ... & \Delta x_n & \Delta y_n & \Delta \alpha_n & \Delta y_{n+1} & \Delta \alpha_{n+1} \end{bmatrix}^T \tag{3.13}$$

$$\Delta \mathbf{r}_B = \begin{bmatrix} \Delta x_1 & \Delta y_1 & \Delta x_{n+1} \end{bmatrix}^T = \begin{bmatrix} 0 & 0 & \Delta r_{vessel} \end{bmatrix}^T \tag{3.14}$$

$\mathbf{K}_{AA}$ and $\mathbf{K}_{AB}$ are sub-matrices of the total system stiffness matrix given in (2.35), $\mathbf{K}_{AA}$ is the riser stiffness matrix corresponding to the unknown DOFs (x, y and α) given in (3.13), $\mathbf{K}_{AB}$ the stiffness matrix coupling the in-plane vessel motion Δr_{vessel} (i.e. surge or sway) to the remaining DOFs $\Delta \mathbf{r}_B$. The DOFs x_1 and y_1 correspond to the bottom pin-joint of the riser.

The bottom angle corresponds to the first component in the displacement vector $\Delta \mathbf{r}_A$ whereas the top angle corresponds to the last component in $\Delta \mathbf{r}_A$. From (3.12), the relationship of the riser end angles and the vessel position can be extracted and given by

$$\Delta \alpha_b = -\left(\mathbf{K}_{AA}^{-1} \mathbf{K}_{AB} \right)_1 \Delta r_{\text{vessel}} = -c_b \Delta r_{\text{vessel}}$$
$$\Delta \alpha_t = -\left(\mathbf{K}_{AA}^{-1} \mathbf{K}_{AB} \right)_{3n} \Delta r_{\text{vessel}} = -c_t \Delta r_{\text{vessel}} \tag{3.15}$$

where the coefficients c_t and c_b represent, respectively, the change in angle given a unit change of the vessel position and are established *a priori* based on the static profile of the riser, and $\Delta \alpha_t$ and $\Delta \alpha_b$ are the change in top and bottom riser angles.

3.5   Plant Control of Vessel-riser-mooring System

Based on the control plant model of vessel and riser angles in Section 3.4 as well as the mooring system discussed in Section 2.4, the control algorithm of the PM system is proposed. The main components of high level controller such as nonlinear observer, line tensioning control and heading control are presented for a moored vessel in this section.

3.5.1 Nonlinear Passive Observer

Filtering and state estimation are important features of both DP and PM systems as there will be temporarily loss of position and heading measurements. The slowly-varying disturbances should be counteracted by the positioning system. The WF part of the motion should not be compensated to minimize fatigue failure. In such situations, the purpose of the observer is to estimate the LF position and velocity and filter out the WF motions. In this study, the nonlinear passive observer for PM system proposed by Fossen and Strand (1999) is employed. The observer of the physical system is typically derived from the control plant model of LF and WF model given in (3.1) to (3.7). The output of the control plant model, $\mathbf{y}$, can be used to steer the state of the observer. When designing the observer, it is convenient to assume that zero-mean Gaussian white noises are omitted in the observer model since the estimator states are driven by the estimation error instead (Fossen and Strand, 1999). By copying the control plant model introduced in Section 3.4.1 and neglecting the white noise term in (3.4) and (3.6) (replacing by the estimation error term), the observer is given as

$$\mathbf{M}\dot{\hat{\mathbf{v}}} + \mathbf{D}_{L}\hat{\mathbf{v}} = \mathbf{R}^{T}(\psi)\hat{\mathbf{b}} + \boldsymbol{\tau}_{moor} + \boldsymbol{\tau}_{thr} + \mathbf{R}^{T}(\psi)\mathbf{K}_{1}\tilde{\mathbf{y}} \qquad (3.16)$$

$$\dot{\hat{\mathbf{b}}} = -\mathbf{T}_{b}\hat{\mathbf{b}} + \mathbf{K}_{2}\tilde{\mathbf{y}} \qquad (3.17)$$

$$\dot{\hat{\boldsymbol{\eta}}} = \mathbf{R}(\psi)\hat{\mathbf{v}} + \mathbf{K}_{3}\tilde{\mathbf{y}} \qquad (3.18)$$

$$\dot{\hat{\mathbf{p}}}_{w} = \mathbf{A}_{pw}\hat{\mathbf{p}}_{w} + \mathbf{K}_{4}\tilde{\mathbf{y}} \qquad (3.19)$$

$$\hat{\mathbf{y}} = \hat{\boldsymbol{\eta}} + \mathbf{C}_{pw}\hat{\mathbf{p}}_{w} \qquad (3.20)$$

where $\tilde{\mathbf{y}} = \mathbf{y} - \hat{\mathbf{y}}$ is the estimation error. The variables of a state observer are commonly denoted by a "hat" to distinguish them from the variables of the equations satisfied by the physical system. When designing the observer, additional terms $\mathbf{K}_{i}\tilde{\mathbf{y}}$ ($i = 1 - 4$) are included to ensure the purpose of the observer is to reduce the estimation error to zero. $\mathbf{K}_{1}$, $\mathbf{K}_{2}$, $\mathbf{K}_{3} \in \mathbb{R}^{3\times3}$ and $\mathbf{K}_{4} \in \mathbb{R}^{6\times3}$ are the observer gain matrices. By analyzing the stability of the observer, Fossen and Strand (1999) defined these matrices as follows

$$\mathbf{K}_{1} = \text{diag}\{k_{1}, k_{2}, k_{3}\}, \quad \mathbf{K}_{2} = \text{diag}\{k_{4}, k_{5}, k_{6}\}, \qquad (3.21)$$

$$\mathbf{K}_{3} = \text{diag}\{k_{7}, k_{8}, k_{9}\}, \quad \mathbf{K}_{4} = \begin{bmatrix} \text{diag}\{k_{10}, k_{11}, k_{12}\} \\ \text{diag}\{k_{13}, k_{14}, k_{15}\} \end{bmatrix} \qquad (3.22)$$

in which k_{1}, k_{2} and k_{3} should be sufficiently high (such as 10^{6}, 3×10^{6} and 10^{8}) to ensure proper bias estimation. If k_{1}, k_{2} and k_{3} are small, the observer may not follow the change in environmental disturbances. The noise may be considerable when these parameters are too high. The parameters of $\mathbf{K}_{2}$ are larger than those of $\mathbf{K}_{1}$ by $10 - 100$ times (such as $25k_{1}$, $20k_{2}$ and $50k_{3}$). For example, Figure 3.3 shows the environmental loads and bias estimations with different observer gain matrix $\mathbf{K}_{1}$. When $\mathbf{K}_{1} = \text{diag}(10^{6}, 3\times10^{6}, 10^{8})$ the observer follows quite well the environmental loads in comparison with lower gain matrix $\mathbf{K}_{1}/10$.
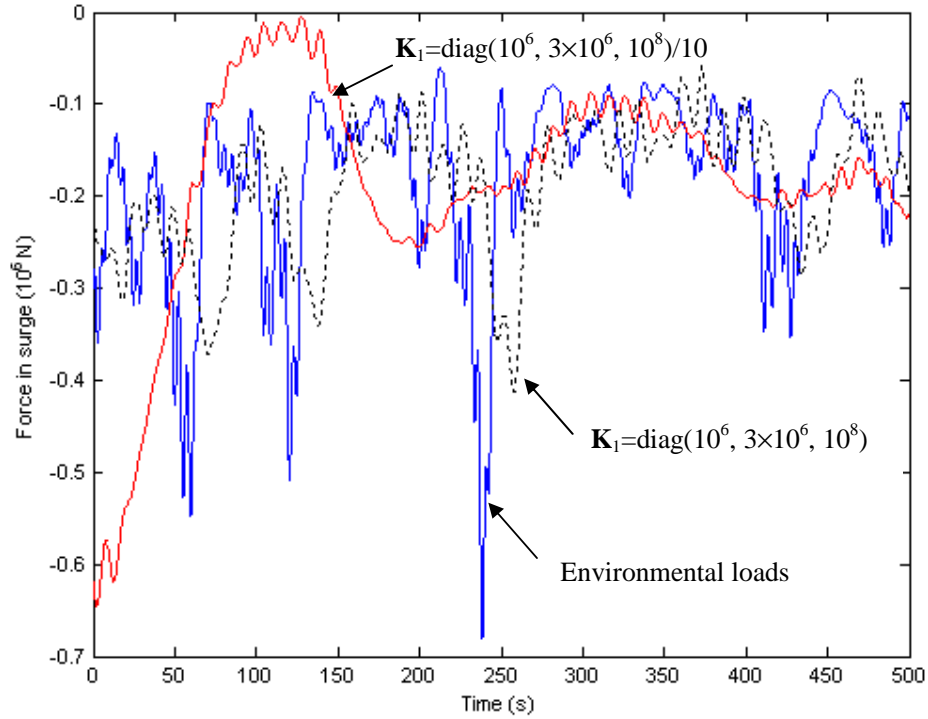
Figure 3.3. Bias estimation with two different values of observer gain matrix $\mathbf{K}_1$

The components of $\mathbf{K}_3$ and $\mathbf{K}_4$ are defined as

$$k_i = \omega_{c,i} \ , \ i = 7,8 \text{ and } 9 \tag{3.23}$$

$$k_i = -2\left(\zeta_{n,i} - \zeta_i\right)\frac{\omega_{c,i}}{\omega_i} \ , \ i = 10,11 \text{ and } 12 \tag{3.24}$$

$$k_i = 2\omega_i\left(\zeta_{n,i} - \zeta_i\right)\frac{\omega_{c,i}}{\omega_i} \ , \ i = 13,14 \text{ and } 15 \tag{3.25}$$

where $\omega_{c,i} > \omega_i$ is the filter cut-off frequency, ω_i the dominating wave frequency or peak frequency component in sea state, $\zeta_{n,i} > \zeta_i$ is a tuning parameter to be set between $0.1 - 1$. All these parameters are chosen based on the stability of the observer (Fossen and Strand, 1999).

3.5.2 Control of Mooring Line Tension

For most mooring systems, the main aim is to control the slowly varying LF motions of the vessel subject to environment disturbances (Sørensen, 2005b) rather

than the WF motions. In PM system, the vessel will be kept in station by the mooring lines as shown in Figure 3.4.
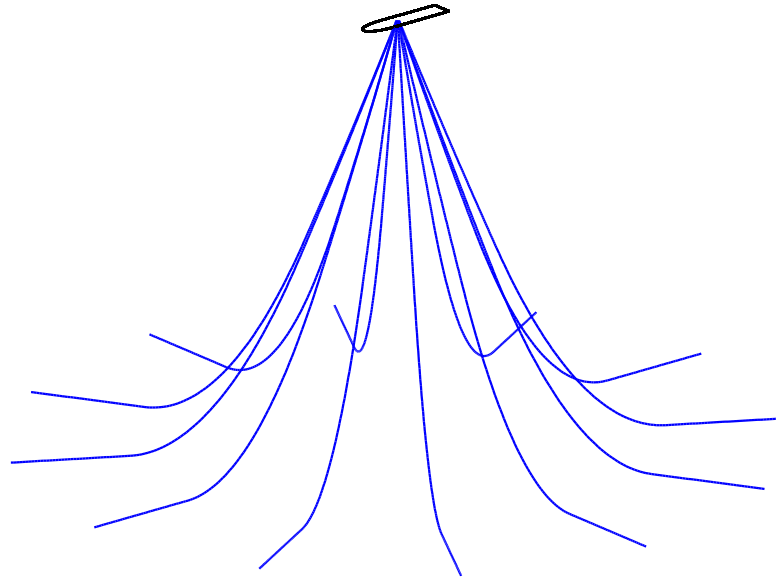
Figure 3.4. Twelve-line spread mooring system

The dominant effect of the mooring system is to passively provide a reactive force to compensate for the mean drift loads of the environment due to wind, wave and current. In this study, the vessel position is controlled by changing the lengths of the mooring lines to produce the required tension. This is done by winches attached on the vessels to pull the cables. In this context, the control of line lengths must be done to compensate the mean rather than the detailed dynamics of the environmental load. This will minimize wear and tear, and reduce the energy for the control of line tensioning. To achieve this, the control force is designed using an integral control law. In proportional–integral–derivative (PID) controller, the contribution from the integral term is proportional to both the magnitude and duration of the error. The integral term will eliminate the residual steady-state error between the desired position and the existing position of the vessel according to the equation

$$\boldsymbol{\tau}_{\text{cmoor}} = -\mathbf{K}_{\text{I}}\mathbf{R}^{\text{T}}\left(\psi\right)\int_0^t\left(\hat{\boldsymbol{\eta}}-\boldsymbol{\eta}_{\text{d}}\right)d\tau \tag{3.26}$$

where $\left(\hat{\boldsymbol{\eta}}-\boldsymbol{\eta}_{\text{d}}\right)\in\mathbb{R}^3$ is the estimated error, $\boldsymbol{\eta}_{\text{d}}$ the desired position vector, $\mathbf{K}_{\text{I}}\in\mathbb{R}^{3\times3}$ the non-negative integral gain matrix and $\mathbf{R}(\psi)$ as defined in (2.6). The control strategy is shown in Figure 3.5.
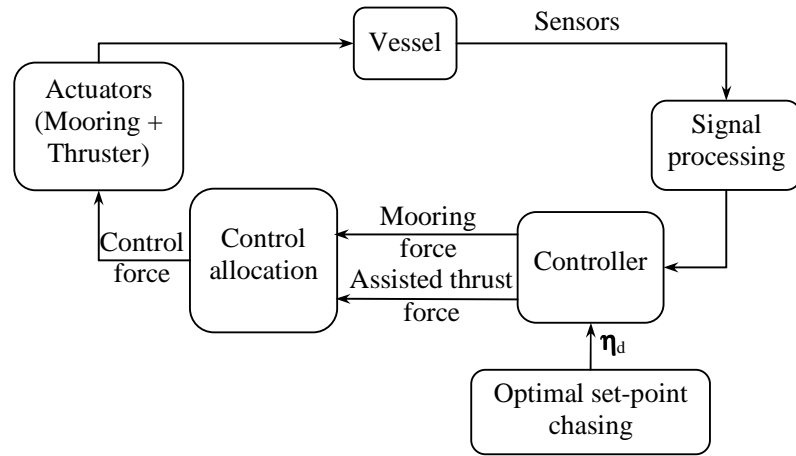
Figure 3.5. Block diagram of control strategy

For instance, when there is no disturbance, the platform is at the equilibrium position (field zero point). Under a specified direction of environmental disturbances in Figure 3.6, the platform will move to another position with a mean offset (Figure 3.7). In order to compensate the mean offset and keep the platform at the field zero point, lines 3, 4, 5 and 6 can be shortened. Additionally, lines 1, 2, 7 and 8 also can be lengthened to ensure the tension of lines 3, 4, 5 and 6 not to increase considerably.
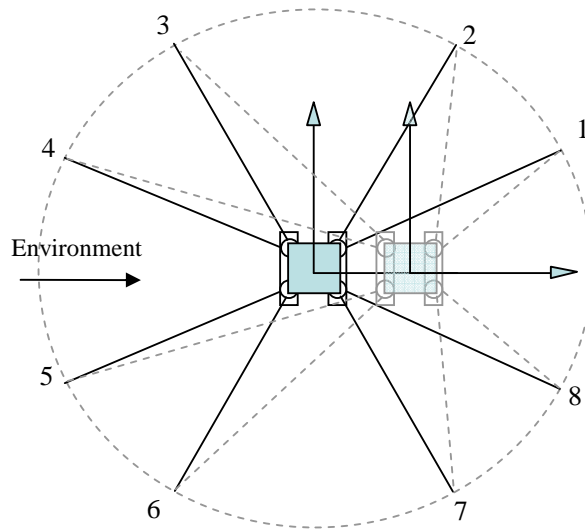
Figure 3.6. Spread mooring system
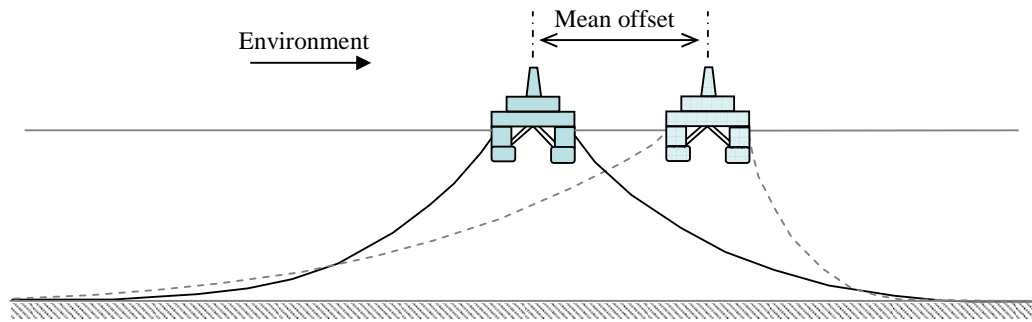
Figure 3.7. Platform offset under environment loading

3.5.3 Mooring Line Allocation

After the high-level plant controller has calculated the commanded forces needed to compensate the mean disturbance loads, the next task is to find the corresponding individual force in the mooring lines such that their cumulative value equals to the command force $\tau_{cmoor} \in \mathbb{R}^3$ (see Figure 3.8). This is the subject of mooring line allocation. For DP system, the thrust allocation for propellers has been investigated by Sørdalen (1997), Fossen (2002) and Johansen et al. (2007).
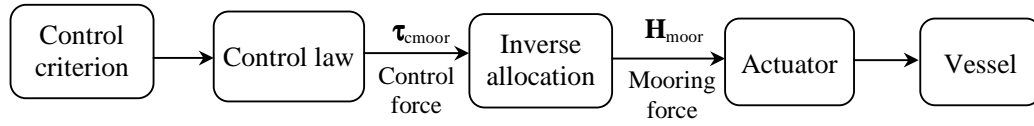
Figure 3.8. Allocation block in control system

The relationship between the control vector $\boldsymbol{\tau}_{\text{cmoor}} \in \mathbb{R}^3$ and the resultant horizontal force from N mooring lines $\mathbf{H}_{\text{moor}} \in \mathbb{R}^N$ has been discussed in Section 2.4 and is given by

$$\boldsymbol{\tau}_{\text{cmoor}} = \mathbf{T}(\boldsymbol{\beta})\mathbf{H}_{\text{moor}} \tag{3.27}$$

where $\mathbf{T}(\boldsymbol{\beta}) \in \mathbb{R}^{3 \times N}$ is defined in (2.48) as functions of the mooring line orientations and moment arms (see Figure 3.9).
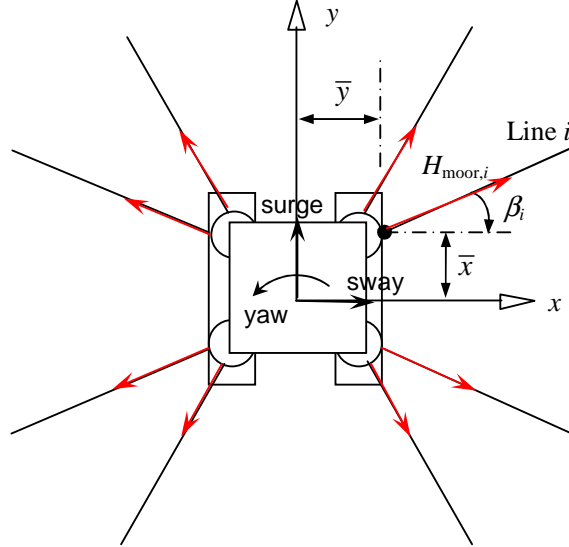
Figure 3.9. Mooring line configuration

Disregarding tension loss, the force provided by mooring line i can be calculated using the catenary equations (given in (2.42) to (2.45)), which relate the horizontal

distance between the anchor point and the top point of mooring line, line lengths and forces.

Conventional spread mooring system of a moored vessel contains from 8 to as many as 16 mooring lines. The mooring spread can assist the vessel to withstand environmental loading from any direction. The allocation problem is normally simple because all control forces produced by the mooring lines are fixed in directions. The mooring line configuration matrix $\mathbf{T}(\boldsymbol{\beta}) \in \mathbb{R}^{3 \times N}$ may not be a square matrix, as there are more control inputs than controllable degrees of freedom (DOFs) such as surge, sway and yaw. In this context, it is possible to find an optimal distribution of control forces by using an explicit method. Fossen (2002) introduced an explicit solution to the *Least Square Optimization* problem using *Lagrange Multipliers* for control allocation of non-rotatable actuators. This method is adopted to calculate the command control action provided by the mooring lines. Hence from (3.27), the resulting horizontal force vector from N mooring lines is written as

$$\mathbf{H}_{\text{moor}} = \mathbf{T}^{+}(\boldsymbol{\beta})\, \boldsymbol{\tau}_{\text{cmoor}} \tag{3.28}$$

where $\mathbf{T}^{+}(\boldsymbol{\beta}) \in \mathbb{R}^{N \times 3}$ is the pseudo-inverse of the mooring line configuration matrix (Fossen, 2002), given by

$$\mathbf{T}^{+} = \mathbf{T}^{\mathrm{T}} \left(\mathbf{T}\mathbf{T}^{\mathrm{T}} \right)^{-1} \tag{3.29}$$

Mooring Actuator: Based on the required force of each mooring line obtained from the control allocation of (3.28), the catenary equations are used to determine the required line length. The relationship between horizontal distance, line length and mooring force in (2.41) is used to obtain the line length from the required control force, as follows

$$H_{\text{moor},i} = f_i\left(X_{\text{hor},i}, L_i \right) \Rightarrow L_i = f_i^{-1}\left(X_{\text{hor},i}, H_{\text{moor},i} \right) \tag{3.30}$$

As illustrated in Figure 3.10, for a given horizontal vessel position X_{hor} and the required force of each mooring line H_{moor} obtained from the control allocation, the required line length L_2 can be determined from the catenary equations given from (2.42) to (2.45). The actuator is activated to shorten the length L_1 to the desired length L_2.
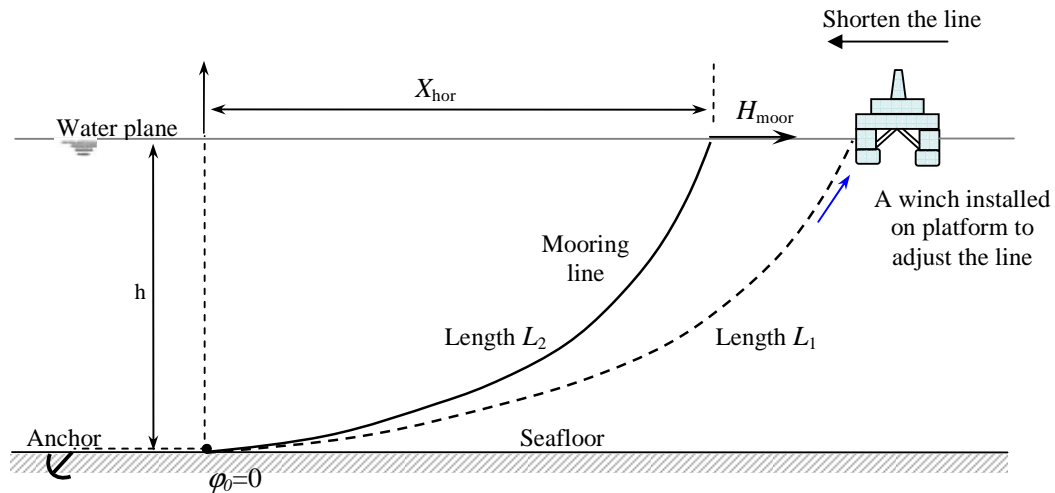
Figure 3.10. Static catenary configuration showing the relations of X_{hor}, H_{moor} and L

Mooring winches (Figure 3.11) installed on the platform are then used to obtain the required lengths by pulling or releasing the lines. In marine application, this equipment is a hydraulic or electric onboard machine. The main components of a winch are the cable drum and the rolling motor. Where practical and appropriate, winch drums are to be designed with a length sufficient to reel up the rope with less than 7 layers of wire. The ratio between winch drum diameter and wire diameter is usually determined by the wire manufacturer. However, the ratio should not be lower than 16 (DNV, 2004). The capacities of mooring winches depend on the minimum breaking strength of the relevant anchor line, wire diameter and required rolling speed.

Figure 3.11. Mooring winch (www.coastalmarineequipment.com)

77

3.5.4 Heading Control by Thrusters

Heading control by thruster is activated by disabling the control forces in surge and sway, and enabling the control moment in the horizontal plane using the PID control law, according to Nguyen and Sørensen (2009c) as follows

$$\dot{\boldsymbol{\xi}} = \tilde{\boldsymbol{\eta}} \tag{3.31}$$

$$\boldsymbol{\tau}_{\text{PID}}^{\psi} = -\mathbf{H}_{\text{i}}^{\psi} \mathbf{K}_{\text{i}} \mathbf{R}^{\text{T}} \left(\psi_y \right) \boldsymbol{\xi} - \mathbf{H}_{\text{p}}^{\psi} \mathbf{K}_{\text{p}} \mathbf{R}^{\text{T}} \left(\psi_y \right) \tilde{\boldsymbol{\eta}} - \mathbf{H}_{\text{d}}^{\psi} \mathbf{K}_{\text{d}} \tilde{\mathbf{v}} \tag{3.32}$$

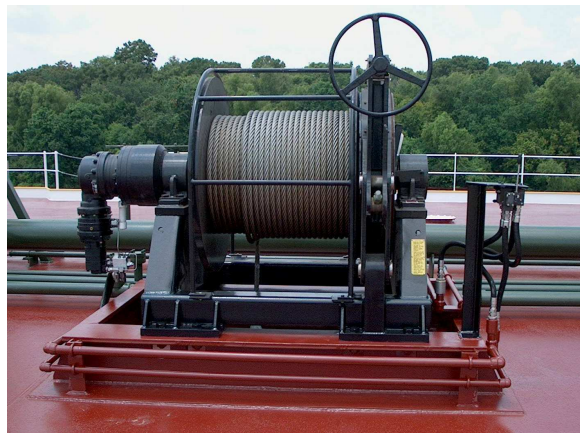where $\tilde{\boldsymbol{\eta}} = \hat{\boldsymbol{\eta}} - \boldsymbol{\eta}_{\text{d}}$, $\tilde{\mathbf{v}} = \hat{\mathbf{v}} - \mathbf{v}_{\text{d}}$, $\boldsymbol{\eta}_{\text{d}}$ and $\mathbf{v}_{\text{d}}$ are the desired position and velocity vector, $\mathbf{H}_{\text{i}}^{\psi} = \mathbf{H}_{\text{p}}^{\psi} = \mathbf{H}_{\text{d}}^{\psi} = \text{diag}(0,0,1)$, $\mathbf{K}_{\text{p}}$, $\mathbf{K}_{\text{i}}$ and $\mathbf{K}_{\text{d}} \in \mathbb{R}^{3\times 3}$ are the non-negative P, I and D controller gain matrices.

3.6   Local Optimization: Optimal Set-point Chasing

For drilling and work-over operations, the main positioning objective is to minimize the riser angle magnitudes at the well-head on the subsea structure and at the top of the riser. In normal control design, it is essential to define the desired vessel position, namely *set-point*, for providing the plant control system to follow. In this case, the vessel position must be optimized based on the riser angle response criterion to ensure low REAs during vessel operations. The purpose of this section is to present the optimal criterion, which is on the local optimization level of the control structure (Figure 3.2) defining set-point to the high level controller presented in Section 3.5.

3.6.1 Optimal Vessel Position accounting for Riser Angle Criterion

In order to minimize the REAs by vessel positioning, the control scheme must be implemented according to the riser angle response criterion to provide a set-point to effect an optimal position of the vessel. The use of such criterion has been proposed by Sørensen et al. (2001), in which the updated Earth-fixed vessel position and heading set-point vector is given as follows

$$\boldsymbol{\eta}_{\text{r}}^{*} = \boldsymbol{\eta}_{\text{r}} + \Delta r_{\text{vessel}}^{*} \begin{bmatrix} 1 & 0 & 0 \end{bmatrix}^{\text{T}} \tag{3.33}$$

where $\boldsymbol{\eta}_{\text{r}} = \begin{bmatrix} x_{\text{r}} & y_{\text{r}} & \psi_{\text{r}} \end{bmatrix}^{\text{T}}$ is the reference position and heading vector in the Earth-fixed frame and $\Delta r_{\text{vessel}}^{*}$ the optimal vessel incremental position, which is determined according to the criterion of REA minimization.

Using the riser FEM model, the vessel offset position can be obtained as a function of the REAs, which is given in (3.15). For obtaining $\Delta r_{\text{vessel}}^*$, a quadratic loss function based on the instantaneous measured REAs and incremental REA components has been introduced by Sørensen et al. (2001) as

$$L = w_t \left[(\Delta\alpha_t + \alpha_t)^2 \right] + w_b \left[(\Delta\alpha_b + \alpha_b)^2 \right] \tag{3.34}$$

where w_t and w_b are the corresponding weight factors of the top angle α_t and bottom angle α_b.

By substituting (3.15) into (3.34) and enforcing the partial derivatives with respect to the vessel increment is zero, the optimal vessel incremental position accounting for the REAs is given as

$$\Delta r_{\text{vessel}}^* = \frac{w_t c_t \alpha_t + w_b c_b \alpha_b}{w_t c_t^2 + w_b c_b^2} \tag{3.35}$$

3.6.2 Reference Model

In order to minimize the top and bottom riser angles which become unfavourable due to change in environmental conditions, a target position, namely *set-point* $\boldsymbol{\eta}_r^*$, can be computed by (3.33). In optimal set-point chasing, the vessel moves from a current position $\boldsymbol{\eta}_r$ to the set-point $\boldsymbol{\eta}_r^*$. However, the motion from the current to the target position is not instantaneous and cannot be too abrupt. Hence, the vessel cannot be moved to the target position instantaneously. Instead, a smooth transition is required. To transit smoothly from one set-point to another along the path which the vessel is intended to follow, a reference model taking into account the dynamic characteristics of the system is formulated. This has been proposed by Sørensen et al. (1996) and is given by

$$\mathbf{a}_d^e + \boldsymbol{\Omega}\mathbf{v}_d^e + \boldsymbol{\Gamma}\mathbf{x}_d^e = \boldsymbol{\Gamma}\boldsymbol{\eta}_r^* \tag{3.36}$$

where $\mathbf{a}_d^e$, $\mathbf{v}_d^e$ and $\mathbf{x}_d^e \in \mathbb{R}^3$ define the desired vessel acceleration, velocity and position trajectories in the Earth-fixed frame. The vector $\boldsymbol{\eta}_r^* \in \mathbb{R}^3$ defines the set-point coordinates. The transition generated in (3.36) is illustrated in Figure 3.12. The design parameters in the reference model consist of a non-negative diagonal damping matrix $\boldsymbol{\Omega} \in \mathbb{R}^{3\times3}$ and a diagonal stiffness matrix $\boldsymbol{\Gamma} \in \mathbb{R}^{3\times3}$ written as

$$\mathbf{\Omega} = \mathrm{diag}\{2\zeta_i\omega_i\}\ ,\quad i=1,2,3$$
$$\mathbf{\Gamma} = \mathrm{diag}\{\omega_i^2\}\ ,\quad i=1,2,3 \qquad\qquad (3.37)$$

where ζ_i is the relative damping ratio, and ω_i the frequency. These parameters are defined based on the performance of reference model such that the model can provide smooth transition without overshoot in the response (Sørensen et al., 1996).
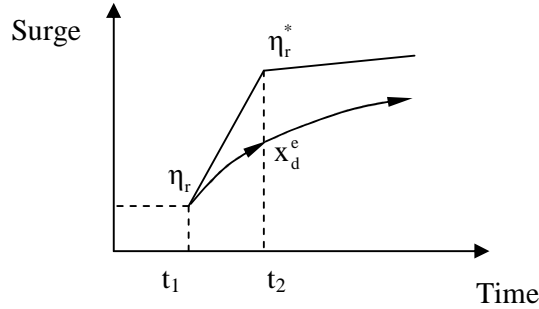

Figure 3.12. Smooth transition by reference model

3.7   Numerical Simulations

3.7.1 Problem Definition

Simulations of a turret moored vessel operating in the Norwegian Sea were carried out to demonstrate the effect of mooring line tension control algorithm. The mean drift motion was controlled by changing the mooring lengths while the thrusters control the vessel's heading. The simulations were conducted using the Marine Systems Simulator (MSS) developed by Fossen and Perez (2004) at the Norwegian University of Science and Technology (NTNU). It is a simulator for marine systems and contains basic libraries written in Matlab/Simulink® platform, based on which examples for the guidance, navigation and control of vessel models governed by (2.50) and (2.73) in Section 2.5 have been developed. Details of the MSS can be found in Appendix B. In this study, the multi-cable mooring system and riser FEM model were added in the MSS to execute the proposed control strategy of the marine riser system.

The main parameters of vessel are given in Table 3.1. The mooring system consists of 12 cables connected to the vessel through the turret, with anchor points distributed evenly on a circle (Figure 3.13). Each line consists of three segments. The

parameters of each segment are presented in Table 3.2. The vessel operates at a water depth of 380 m and has a riser which is subjected to a vertical tension of 60 tons at its top end. Detailed specifications of the riser are given in Table 3.3.
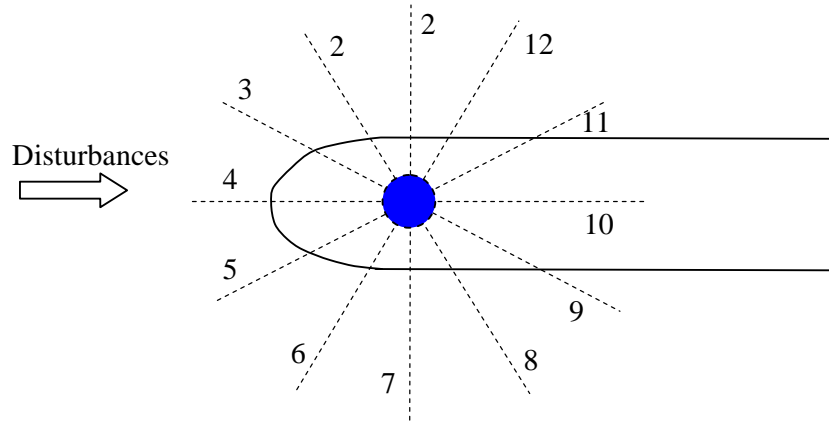
Figure 3.13. Moored vessel with 12 anchor lines used in simulations

Table 3.1. Vessel main parameters

Parameter	Unit	Value
Mass	ton	119600
Overall length	m	271
Breadth	m	41
Design draught	m	15.5
Turret diameter	m	9

Table 3.2. Properties of mooring lines

Parameter	Unit	Segment 1 (near surface)	Segment 2 (middle)	Segment 3 (near seabed)
Modulus of elasticity	10^5 kN/m^2	838.5	1126	979.7
Unstretched length	m	954	342	72
Diameter	m	0.137	0.121	0.114
Cable density	kg/m	1178	1265	1178
Added mass coefficient		1.5	1.5	1.5
Normal drag coefficient		2.5	2.5	2.5

Table 3.3. Properties of riser

Parameter	Unit	Value
Top tension	ton	60
Modulus of elasticity	10^7 kN/m^2	20.2
Sea water density	kg/m^3	1025
Riser pipe density	kg/m^3	7850
Mud density	kg/m^3	800
Outer diameter	m	0.3
Inner diameter	m	0.285
Added mass coefficient		2
Normal drag coefficient		1
Total submerged weight of riser (including mud)	ton	13

The moored vessel in this study was subjected to environmental disturbances due to wind, wave and current. The simulation was performed with a significant wave height, H_s = 5 m, wave period, T_p = 14.18 s (JONSWAP distributed wave), wind velocity, v_{10} = 22.41 m/s, and surface current velocity, v_c = 0.5 m/s.

3.7.2 Effect of Vessel Offset on REAs

In drilling operation, it is difficult to keep both REAs within the allowable limit (ideally, ±2°). In most cases, these angles usually exceed the limit due to the surface vessel offset. Figures 3.14 and 3.15 show the static deformations of the riser and the REAs under vertically uniform current of 0.5 m/s for various vessel offsets (from 0 m to 30 m) of the vessel.
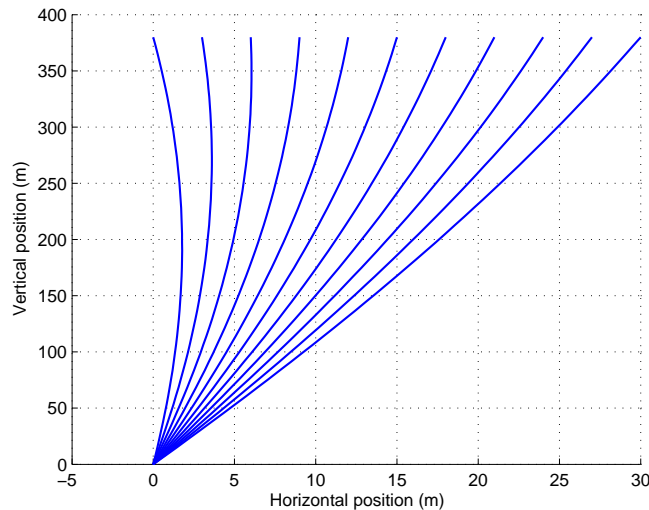

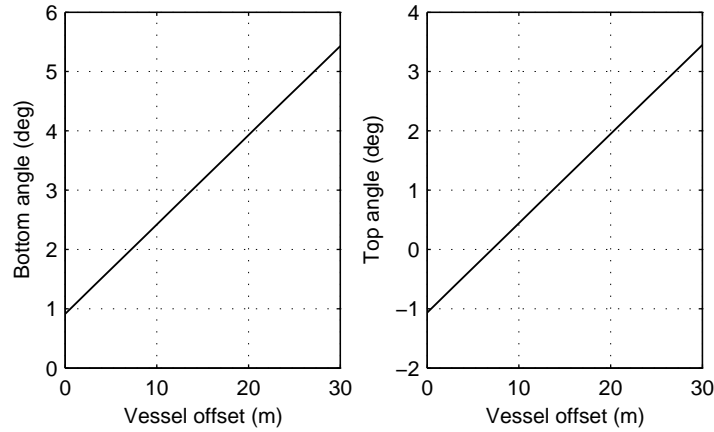Figure 3.14. Riser deflections with different vessel offsets (0 m – 30 m)

Figure 3.15. Bottom and top riser angle with different vessel offsets

When the vessel offset is zero, meaning that the vessel is right above the well-head, the bottom and top angles are 1° and -1°, respectively, due to riser deformation caused by vertical uniform current 0.5 m/s. When the vessel offset increases, the REAs also increase, where the bottom and top angles can reach values of 5.4^o and 3.4^o for vessel offset of 30 m. According to Chen (2001), within a considered offset range, the relation between static angular response and vessel offset is close to linear for both the top and bottom angles.

3.7.3 Effect of Position Mooring Control

Ideally, the set-point chasing introduced in Section 3.6 should be automatically activated and implemented in real-time to ensure small REAs. In actual practice, the set-point chasing may also be activated manually by the operator when he observes the REAs increasing. Once the set-point chasing is activated, it is operated in real-time. In this study, to highlight the importance of the control algorithm, the set-point chasing is automatically activated when the REAs are large. To control both angles, (3.35) was used to obtain the optimal vessel position in the simulations. The desired heading was set against the direction of the resultant environmental loads. Heading control was maintained by thrusters.

To demonstrate the effect of control, the model was simulated without line tensioning control for the first 3000 s, before activating line tensioning control for the next 6000 s as shown in Figures 3.16 − 3.20. Figure 3.16 shows the vessel position and heading. Under the environmental disturbances, the vessel has experienced a drift of 27.4 m (mean offset) in the direction of external loads, and both REAs increased to 4°

and 6° (see Figure 3.17) without line tensioning control, where all line lengths were kept equal at 1368 m.
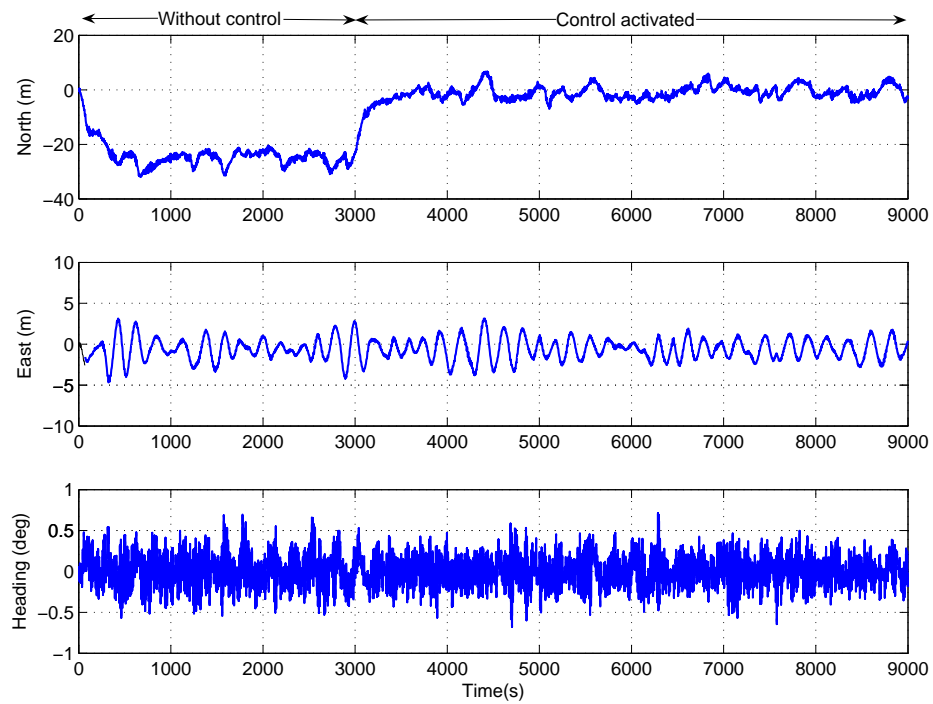

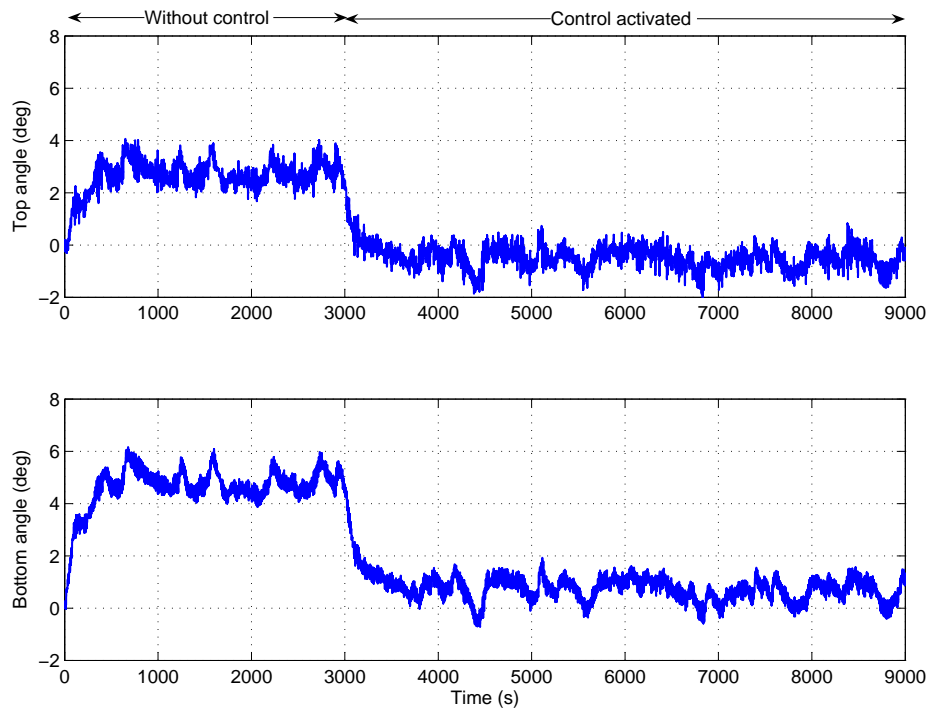Figure 3.16. Vessel motion in surge, sway and yaw (simulation)

Figure 3.17. Top and bottom end riser angles (simulation)

When the line tensioning control was activated after 3000 s, the optimal set-point was generated based on the measured REAs. The mooring line lengths were changed to keep the mean position at the optimal set-point. As shown in Figure 3.16, when the control was activated, the drift of the vessel decreased gradually from 27.4 m to the optimal value around the well-head (0 m). The riser angle responses were kept within $\pm 2^{o}$ as shown in Figure 3.17, illustrating the effectiveness of line tension control. In Figure 3.18, snapshots of the riser profile in the simulations are shown. During the control operation, the riser profiles are found to be at the desired areas obtained from the optimal set-point chasing algorithm to ensure the small REAs. The different line lengths generated after activating the controller are shown in Figure 3.19. Figure 3.20 shows the time history of maximum and minimum tension of mooring line. It indicates that there was no significant change in tension of mooring lines in comparison to uncontrolled stage. Hence the line breakage may be prevented during control operations.

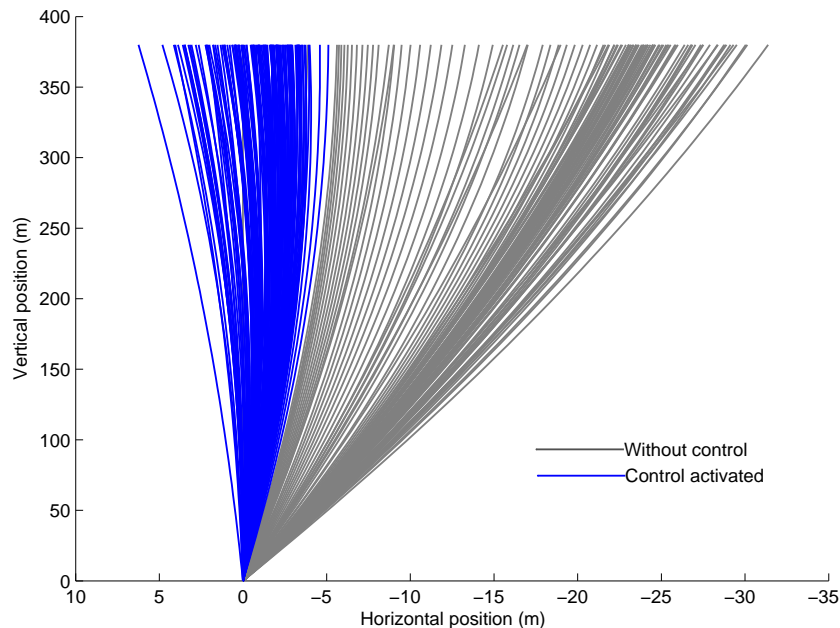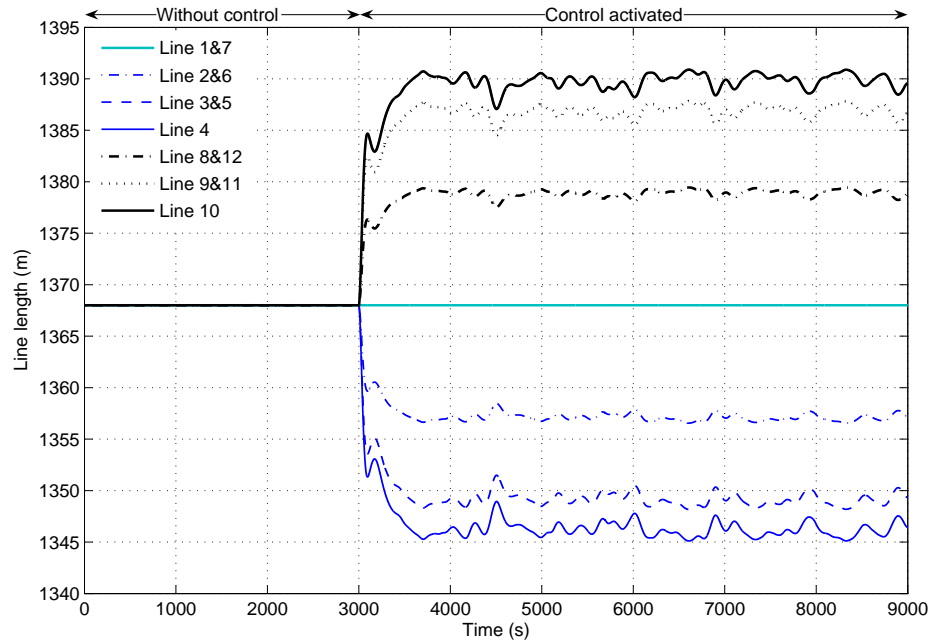Figure 3.18. Riser snapshots under vessel motions (simulation)

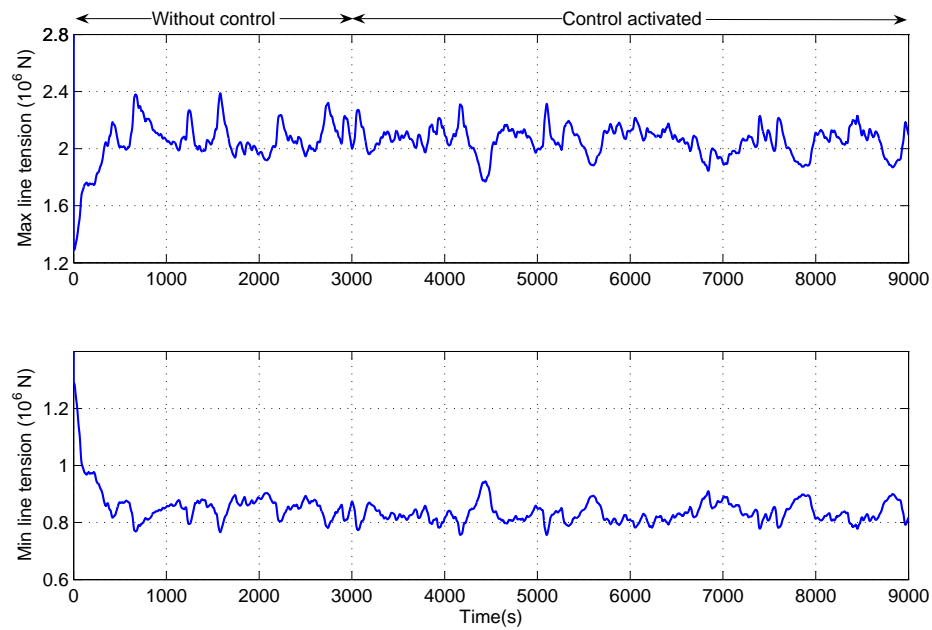Figure 3.19. Variation of line lengths in PM control (simulation)

Figure 3.20. Time history of maximum and minimum tension of mooring lines (simulation)

3.7.4 Comparison with DP System

In PM operations, most of the station keeping in surge and sway is provided by the mooring system. In contrast to PM system, DP operation is used for non-anchored

86

vessel, where station keeping is controlled entirely by the thrusters. The thrusters are used in PM system mainly for damping the surge, sway and yaw oscillatory motions and for keeping the desired heading. However, the thrusters may not be necessary under normal environmental condition. Hence, the use of mooring systems should result in lower thrust capacity and less fuel consumption. Three cases have been simulated to demonstrate the energy reduction when using line tension control under the sea state having significant wave height $H_s = 5$ m and peak period $T_p = 14.18$ s, namely,

1. PM + heading control,
2. PM + heading control + damping by thrusters,
3. DP.

Table 3.4 shows the simulation results in terms of the normalized values obtained from the control forces of thrusters for the above cases. In Case 1, the mean vessel offset was compensated only by the mooring forces. In Case 2, when the oscillatory motions were significant, the thrusters were activated to induce damping to reduce the oscillations. It can be seen that when using thrusters together with line tensioning to reduce the oscillatory motions, the thrusters' forces are considerably less than the case of DP system only (Case 3), thus demonstrating the lower fuel consumption when mooring lines are employed to compensate for the mean environmental loads.

Table 3.4. Force of thrusters (normalized using values obtained by Case 3)

Case	Case 1	Case 2	Case 3
Mean force in surge	0	0.08	1
Mean force in sway	0	0.15	1
Max force in surge	0	0.21	1
Max force in sway	0	0.28	1

3.8   Experimental Tests

Scaled experiments were performed to validate the proposed PM control strategy under normal sea state. The experimental results have been converted and presented in terms of full scale values in this section. The geometric scale of the experimental

model is 1:120. All the issues with regards to the scale factor of the scaled model, Cybership 3, were investigated and addressed in a study of Nilsen (2003).

3.8.1 Experimental Set-up

The experiments were carried out in the Marine Cybernetics Laboratory (MCLab) at the NTNU, using the model vessel, Cybership 3, having a mass, $m = 75$ kg, length, $L = 2.27$ m, and breath, $B = 0.4$ m. The experimental set-up of a floating moored system comprising the vessel, mooring lines and drilling riser is shown in Figures 3.21 and 3.22 and the mooring system model was adopted from Guedes et al. (2005) as shown in Figure 3.23. Four cables were connected to the vessel through the turret at the bow to simulate the effect of the catenary system. Each cable has one end fixed to the turret and the other to the wall of the basin; a mass with submerged weight 8 N was suspended between these two points. The equivalent line spring stiffness of the mooring system is 28 N/m. Strain gauges were attached to the lines to measure the tensions during the experiment. Sail winches installed on the turret of the vessel were used to obtain the required lengths by pulling or releasing the lines. Each winch can rotate forward or backward up to 2.5 turns, depending on the input voltage. Each turn will wind about 120 mm of the line. The drilling riser was modelled by a plastic pipe with outer diameter of 6 mm. To provide higher mass, lead was put inside the riser pipe. The riser was subjected to tension at the top, which was modelled by a tensioned spring. The riser was installed just below the turret. In order to measure the REAs, two reflected light markers were attached at the top and bottom of the riser. An underwater camera (see Figure 3.21) at the bottom of the water tank was used to capture these marker motions. From these signals, the REAs can be computed. The internal hardware architecture was controlled by an onboard computer which can communicate with an onshore PC in the control room through a WLAN. Like vessel position cameras, the underwater camera captured responses of REAs during the experiment and sent the signals to the onboard computer. The controller used this signal to compute the set-up and keep the vessel in position. More details of the MCLab and Cybership 3 can be found in Appendix A.
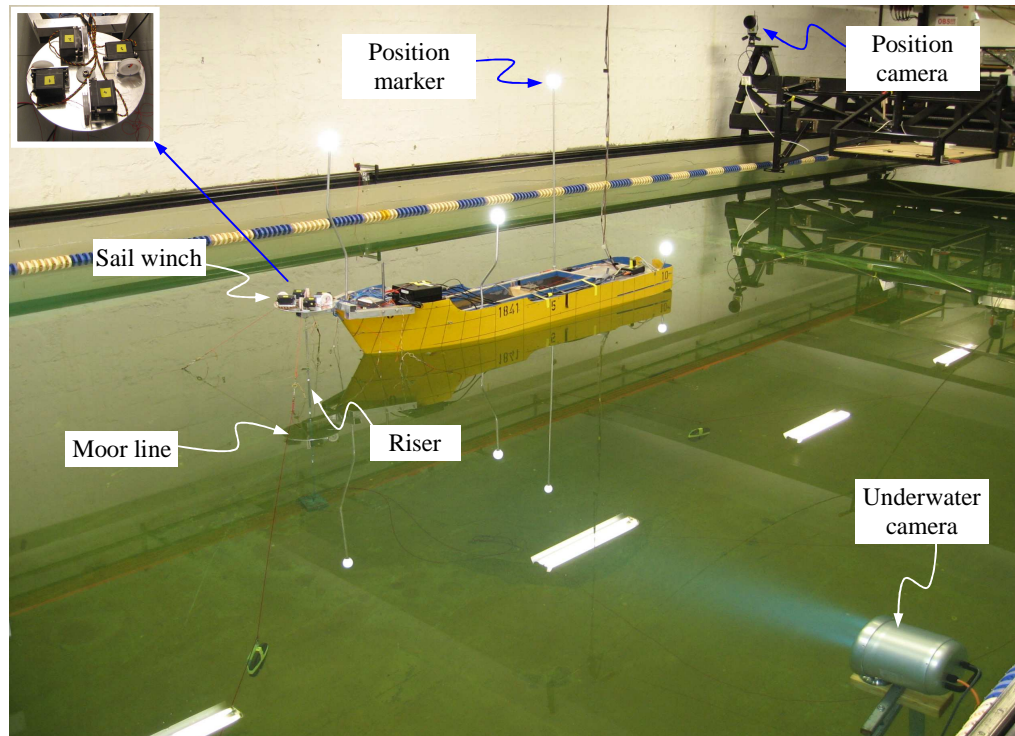
Figure 3.21. Experimental set-up

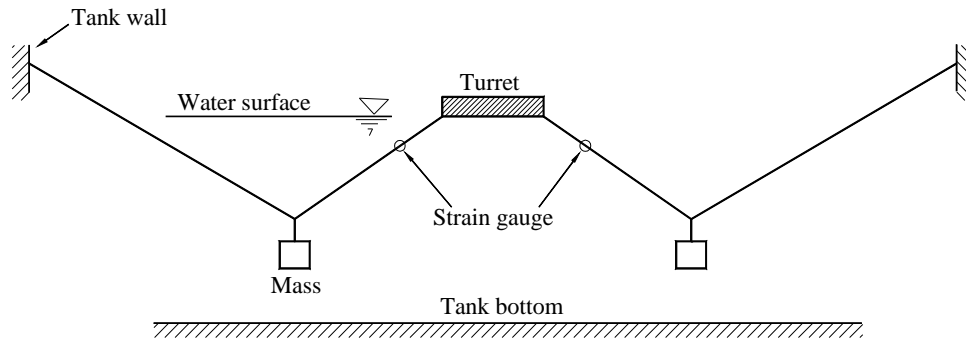Figure 3.22. Close-up view of turret with 4 sail winches

Figure 3.23. Mooring line arrangement in experiment

3.8.2 Experimental Results

Similar to the numerical simulations, the experiments were performed in 2 stages. No control was intentionally activated during the first 3000 s to demonstrate the effectiveness of the control system. Figure 3.24 shows the measured vessel position in which the PM control was activated after 3000 s. Under wave and current, the vessel was pushed off the initial position to other positions around 20 m. Under control operation, the set-point was generated based on the REAs and the surge was drastically reduced to maintain low REAs. The effect of PM control on the REAs is clearly shown in Figure 3.25, with the bottom REA decreasing from 6° to 0.4^o, and the top REA decreasing from 5.3^o to -0.2^o. Hence, reducing the offset of the vessel through the set-point chasing algorithm is effective in maintaining small REAs. The results compared well with those obtained in the simulations.

The advantage of controlling only the LF motions can be observed in Figure 3.26, which shows the variation in line lengths in the experiment. The controller is able to generate the necessary changes in line lengths to obtain the appropriate vessel positions and yet the changes do not contain significant oscillations. Hence the wear and tear of mooring lines is somewhat minimized with lower energy and yet able to fulfill the control objective.
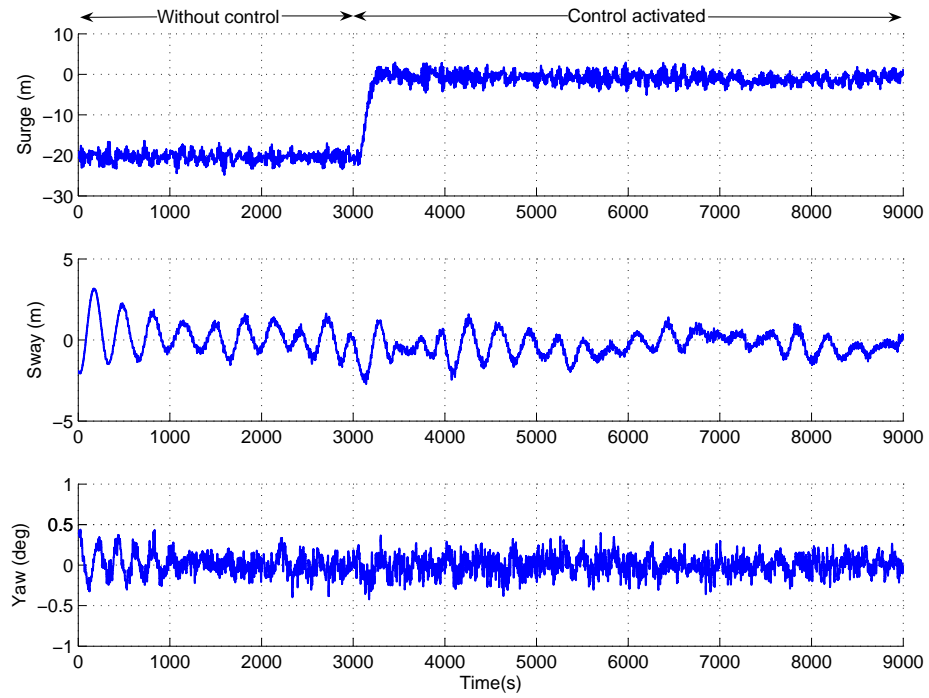
Figure 3.24. Measured vessel motions in experiment
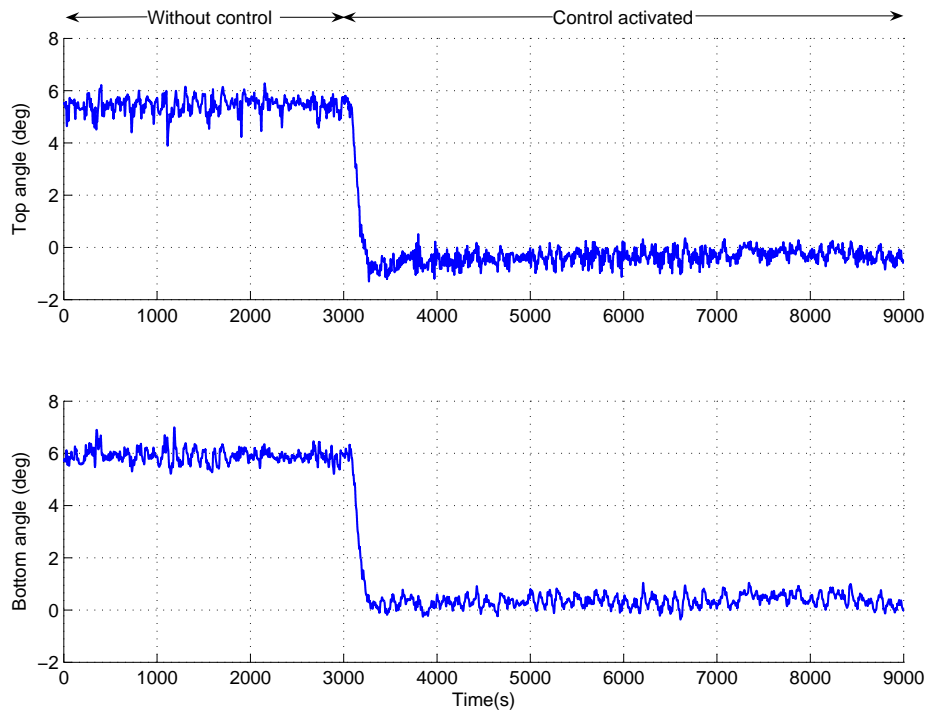
Figure 3.25. Measured top and bottom end riser angles in experiment
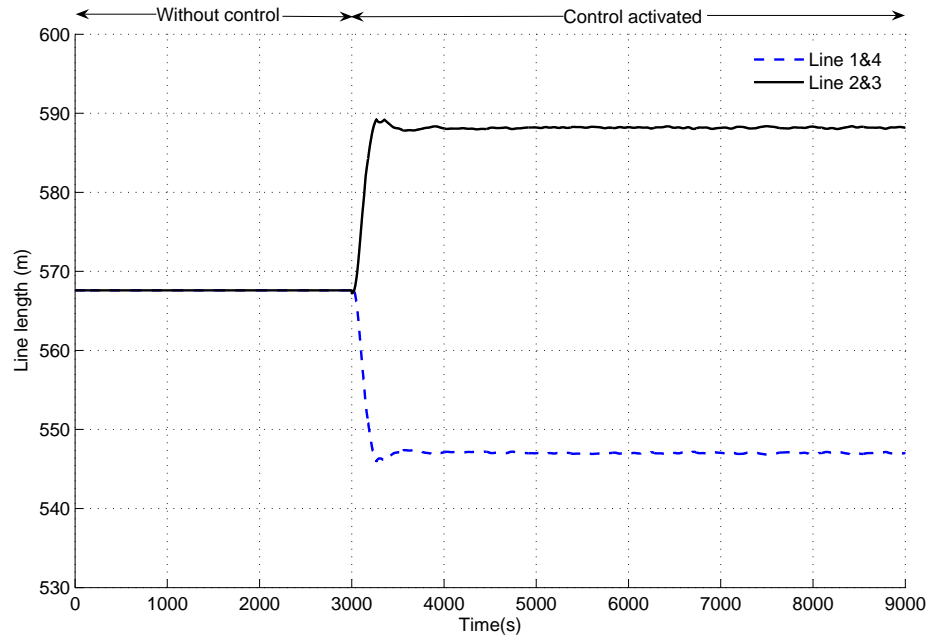
Figure 3.26. Changes of line lengths in experiment

3.9   Conclusions

In this chapter, a new control strategy for PM system was proposed to reduce the REAs in shallow water depth through tension adjustment in the mooring lines to move to an optimized set-point. The beam element was used to model the riser since the bending stiffness may be significant in shallow water applications. An optimal set-point chasing based on the REAs as the control criterion was formulated. Numerical simulations and experiments performed indicated that it is possible to reduce the REAs by maintaining the position of the PM vessel at the desired position through controlling the lengths of the mooring lines. Basically, the mooring system provides the mean force to compensate the mean drift loads of the environment due to wind, wave and current. By letting the line tensioning counteract the mean loads arising from the disturbances, considerable reduction in fuel consumption can be achieved, compared to the case of using thrusters control continuously for both position and heading as in DP systems. The control strategy proposed herein can be applicable for moderate sea states. In extreme sea states, a different control scheme should be applied. In such control scheme, the control strategy proposed herein may require more

fuel consumption by the thruster operation to reduce the vessel oscillations and the risk of mooring line breakage becomes significant.

CHAPTER 4. MINIMIZATION OF RISER BENDING STRESSES

4.1   Introduction

In Chapter 3, the PM control strategy has been proposed in which the REAs were used as the control criterion. In terms of horizontal and vertical motions of the riser, the bottom end at the seabed is restrained in both the horizontal and vertical directions whereas the top end is constrained by vessel motions. With regards to rotation, the end boundary conditions are modeled to be free in rotation corresponding to the case where the ends are connected by ball-joints. This implies that the bending stresses at the riser ends can be taken as negligible.

Besides the end angles, performance failure of the riser system can be caused by excessive stresses and hence is also an important response parameter for control considerations. To address this, two approaches are taken in this chapter with regards to the bending stresses of the riser. Firstly, bending stresses along the riser are monitored and examined when the vessel positions are controlled using the REAs criterion in Section 3.6. Secondly, the case where bending stiffeners are provided at the riser ends is studied. Assuming that the rotational stiffness at the riser ends are high, the REAs can be taken as zero. The control criteria will then be based on end bending stresses rather than end angles.

4.2   Calculation of Riser Bending Stresses

In Chapter 2, the entire riser is discretized into elements and then solved via FEM. The force resultants of an element can be determined from the state of deformation and stiffness of the riser. For a plain round pipe, the bending stress σ due to an in-plane bending moment M_b acting on the section is

$$\sigma = \frac{M_b D_{out}}{2I} \tag{4.1}$$

where I is the second moment of inertia, which is calculated from the external diameter D_{out} and internal diameter D_{int} of riser pipe, as follows

$$I = \frac{\pi}{64}\left(D_{out}^4 - D_{int}^4\right)$$ (4.2)

According to riser design criteria of API (1998), for plain round pipe, the von Mises equivalent stress σ_e including radial, hoop and axial stresses (σ_{pr}, $\sigma_{p\theta}$ and σ_{pz}) should be less than the allowable stress defined by the right hand side of the following inequality.

$$\sigma_e = \frac{1}{\sqrt{2}}\sqrt{\left(\sigma_{pr} - \sigma_{p\theta}\right)^2 + \left(\sigma_{p\theta} - \sigma_{pz}\right)^2 + \left(\sigma_{pz} - \sigma_{pr}\right)^2} \le C_f C_a \sigma_y$$ (4.3)

where

$$\sigma_{pr} = \frac{\left(P_{out}D_{out} + P_{int}D_{int}\right)}{D_{out} + D_{int}}; \quad \sigma_{p\theta} = \left(P_{int} - P_{out}\right)\frac{D_{out}}{2t_w} - P_{int}; \quad \sigma_{pz} = \frac{T_e}{A} \pm \sigma$$ (4.4)

$C_f = 1$ is the design case factor, $C_a = 2/3$ the allowable stress factor, $\sigma_y = 235$ MPa the yield strength of steel, σ the bending stress given in (4.1), t_w the wall thickness of riser pipe. Other parameters such as external pressure P_{out}, internal pressure P_{int} and effective tension T_e are defined in Section 2.3.2 of Chapter 2.

4.3   Control Criterion based on End Angles

4.3.1 Problem Statements

Consider the case where the riser is assumed to be hinge-connected at its two ends. The desired vessel optimal positions are computed based on the REA criterion, which ensures the angles at both end of the riser to be minimized. The bending stresses along the riser are then examined. There are two possibilities. First, by enforcing the REAs, the bending stresses are automatically below the allowable limit. In such a case, REAs is a stricter criterion and is sufficient in terms of performance. The second possibility is when the bending stresses may be exceeded even though the REAs are within the allowable limit. A study is thus needed to establish the allowable REA limit for such case so that it can be used as a limiting criterion, eliminating the need to check for bending stresses during implementation.

As an illustration, simulations are carried out with a moored vessel, having a mass, $m = 166 \times 10^3$ tons, length $L = 217$ m, breath $L = 41$ m, and draft $D = 15.5$ m. The mooring system consists of 12 lines in a water depth of 380 m. The riser has a top

tension of 60 tons, outer diameter of 0.3 m, inner diameter of 0.285 m, material density of 7850 kg/m^3 and modulus of elasticity of 20.2×10^7 kN/m^2. The simulation is performed with a significant wave height, H_s = 5 m, wave period, T_p = 14.18 s, wind velocity, v_{10} = 22.41 m/s, and surface current velocity, v_c = 0.5 m/s. In the simulations, the entire riser was divided into 50 elements.

4.3.2 Simulation Results and Discussions

The model was simulated without line tensioning control for the first 2000 s, before activating automatic line tensioning control for the next 2000 s as shown in Figures 4.1 − 4.6. The vessel motions, REAs and variation of line lengths are shown in Figures 4.1 − 4.3. When the control was activated at 2000s, the controller generated the optimal vessel positions and maintained small REAs consistent with the results in Chapter 3. Figure 4.4 shows the bending stresses at three selected locations along the riser, specifically, near the bottom end (node 6), at the middle (node 24) and near the top end (node 43). Figures 4.5 and 4.6 present snapshots and corresponding bending stress profiles of the riser subjected to vertical current and LF vessel motion at the top end. When automatic control is activated, the riser profiles are found to be at the desired areas (around the well-head) obtained from the optimal set-point chasing algorithm. By comparing the bending stresses when the vessel is operating without and with automatic control as shown in Figures 4.4 and 4.6, it is seen that the bending stress level along the riser is reduced with PM control. As shown in Figure 4.4, after 2000s when automatic control is activated, the maximum values of bending stresses are 1.9 MPa, 2.77 MPa and 3.36 MPa obtained at nodes 6, 24 and 43 respectively. The corresponding von Mises equivalent stresses including radial, hoop and axial stresses computed by using (4.3) are 93.1 MPa, 90.4 MPa and 89 MPa, which are below the allowable stress (C_f $C_a\sigma_y$) given in (4.3). This demonstrates that by controlling REAs at the appropriate limit, bending stress levels is automatically controlled. Once the REA limit is established, through extensive numerical simulation or finding a relationship between the REAs and the maximum bending stresses for a given configuration, the control procedure follows that outline in Chapter 3.
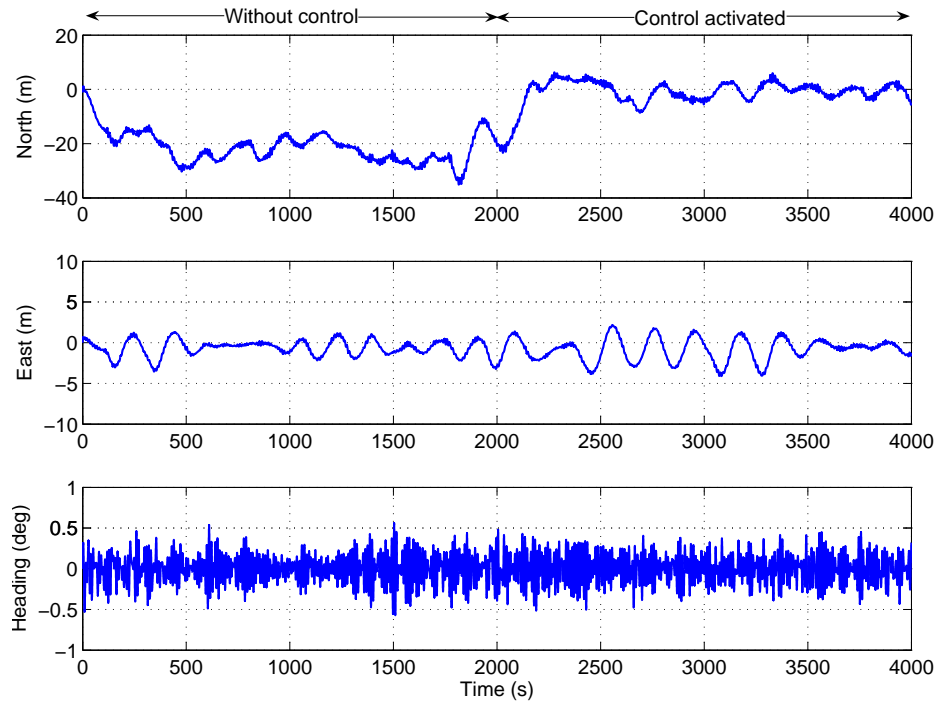
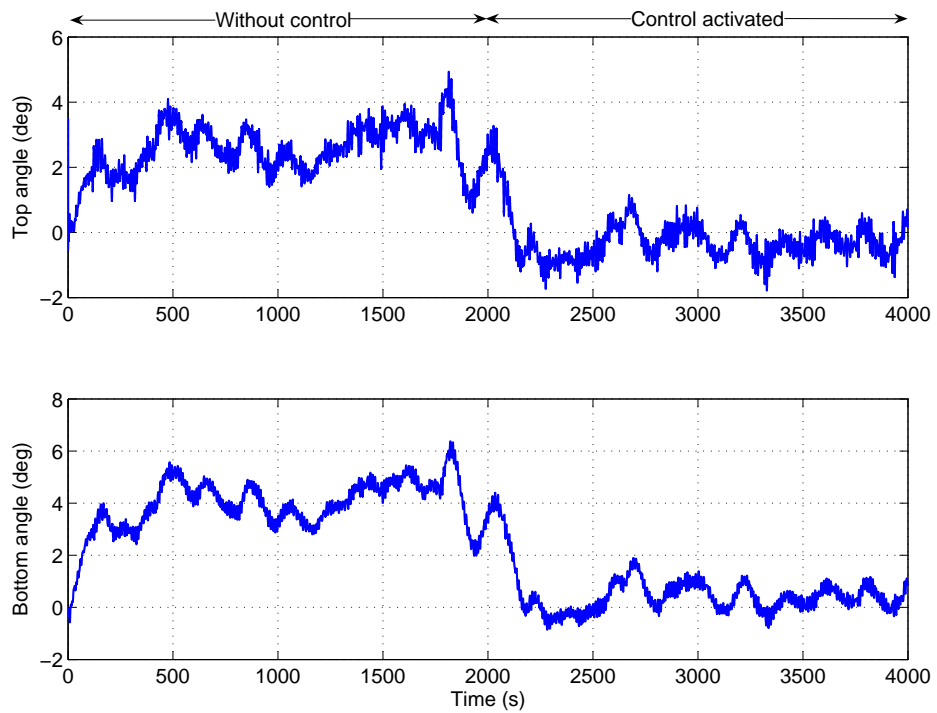Figure 4.1. Vessel motion in surge, sway and yaw

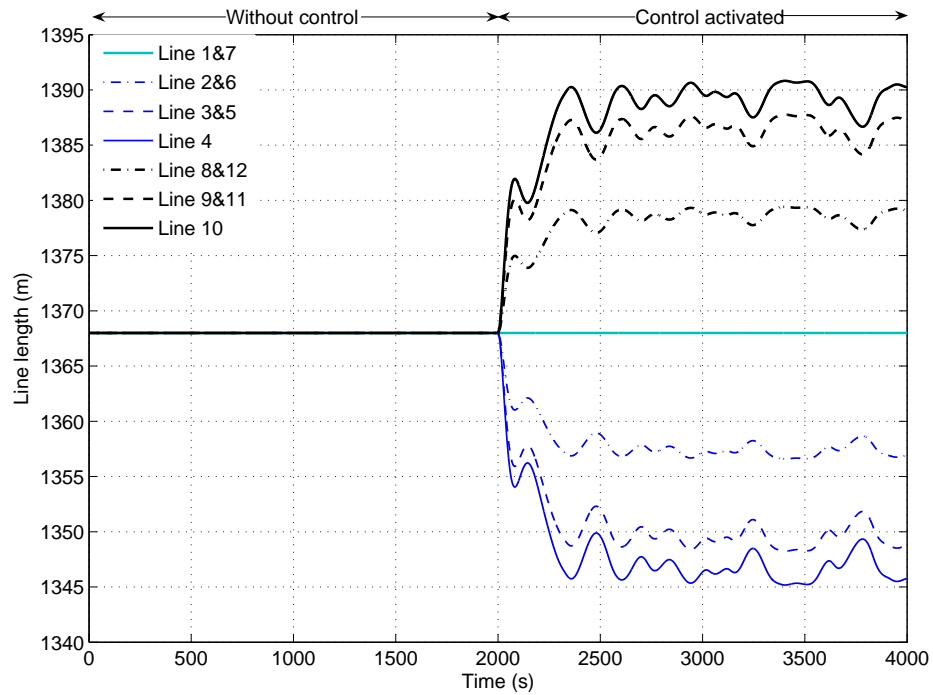Figure 4.2. Top and bottom end riser angles

Figure 4.3. Variation of line lengths in PM control
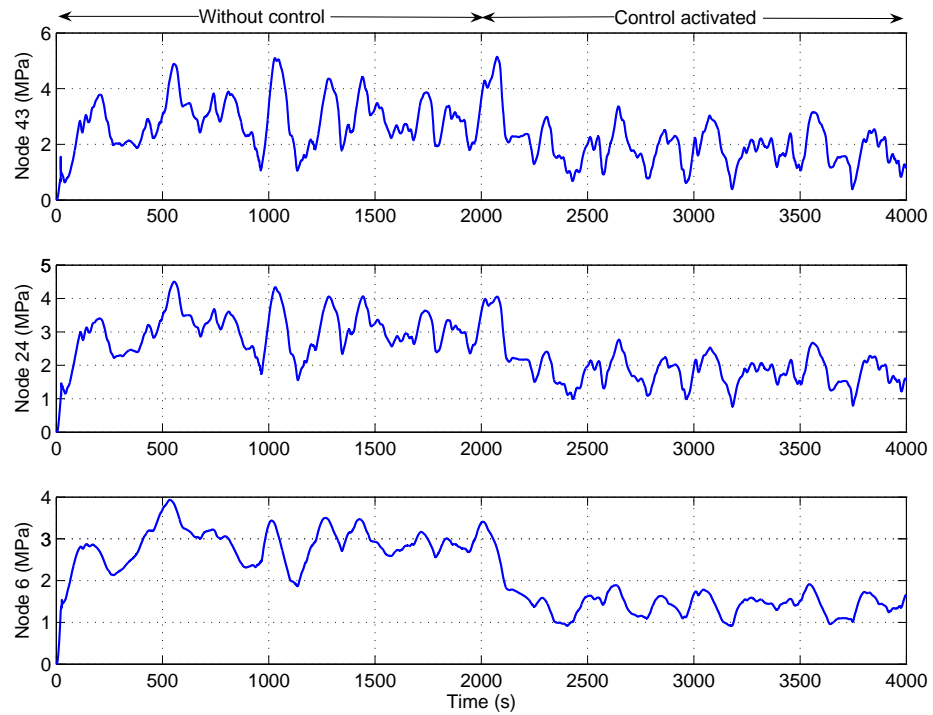
Figure 4.4. Time history of bending stresses along riser
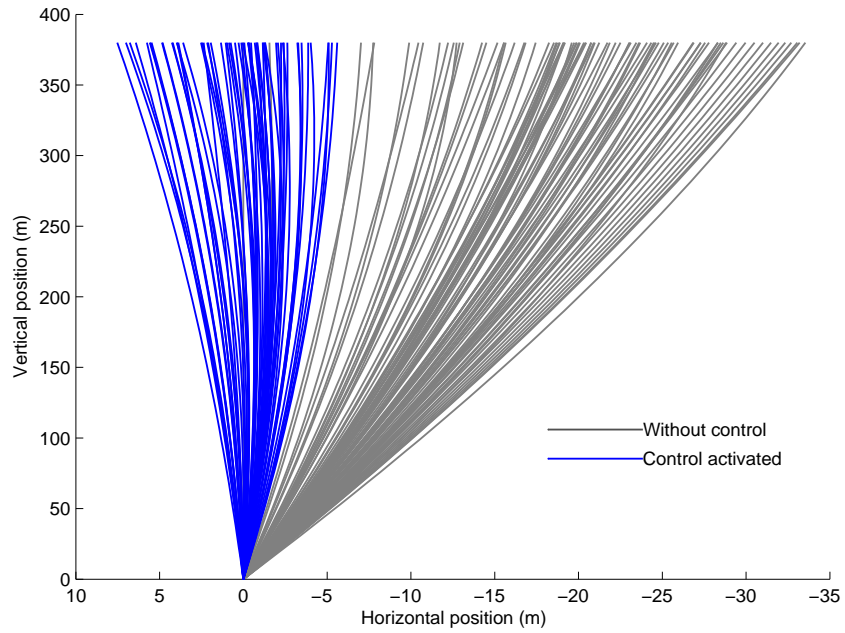
Figure 4.5. Riser snapshots (hinge connection at both ends)
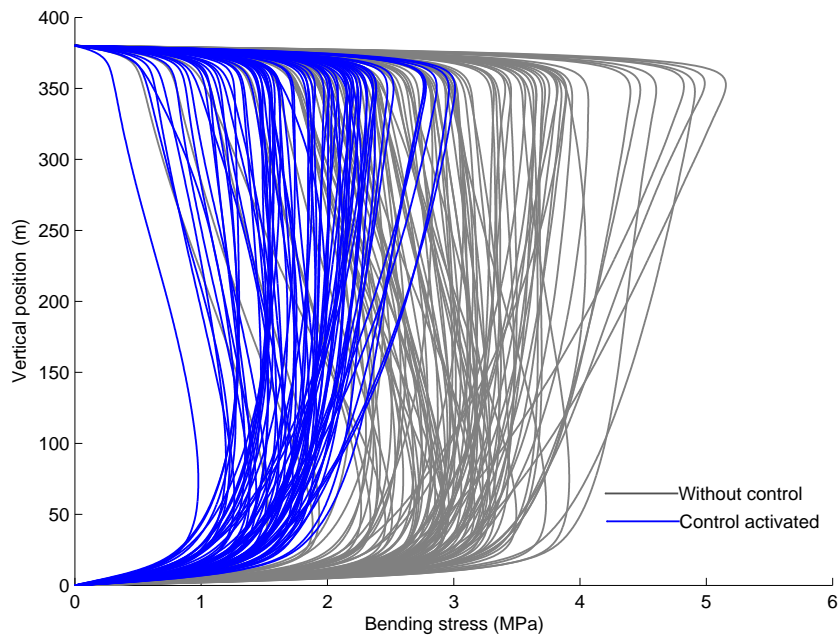
Figure 4.6. Bending stress profiles corresponding to riser snapshots

4.4   Control Criterion based on End Bending Stresses

In the second case, the control algorithm for optimal positioning proposed in Chapter 3 may be extended to cover other types of riser configurations (e.g. top-tensioned production riser). In such cases, risers with bending stiffener (stress joints) (see Figure 4.7) may be installed at both ends for rigid riser end fitting. These conically shaped mouldings add local stiffness to the riser. The end angles are then forced to constantly zero. The main purpose of the bending stiffener is to increase and distribute bending stiffness the riser pipe as well as limit curvature (API, 1998).
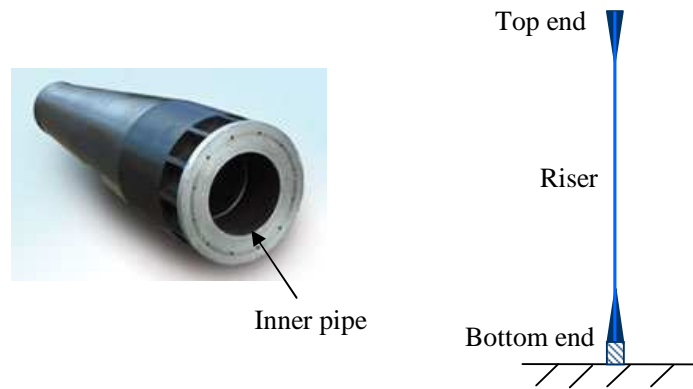
Figure 4.7. Bending stiffener (stress joint)

4.4.1 Optimal Set-point Chasing

When introducing the bending stiffener, the boundary conditions at two ends of the riser model in Section 2.3 need to be modified such that the angles at both ends of the riser are zero. Subsequently, end bending stresses, which are normal stresses caused by end bending moments, are computed by (4.1). The control criterion in the control scheme is then based on end bending stresses rather than end angles. That is, (3.35) is replaced by the following optimal vessel incremental position given by

$$\Delta r_{vessel}^{*} = \frac{w_t c_t \sigma_t + w_b c_b \sigma_b}{w_t c_t^2 + w_b c_b^2} \tag{4.5}$$

where σ_t and σ_b are the bending stresses at the top and bottom end of riser, the coefficients c_t, c_b, w_t and w_b are as defined in (3.15) and (3.34).

4.4.2 Simulation Results and Discussions

The same vessel, riser and mooring system in Section 4.3 is used for the numerical simulations, except that the two ends of the riser are each installed with a bending stiffener having an outer diameter of 0.34 m. Initially, the vessel was passively positioned by the mooring system under the external disturbances. After 2000 s, automatic control based on set-point chasing was activated. The optimal vessel position was then generated based on the measured end bending stresses. The mooring line lengths were actively changed to keep the mean position at the optimal set-point. The control objective, in which the vessel position is optimized by the control criterion based on the end bending stresses, is identical to the case where the set-point chasing is based on the REAs. Figures 4.8 and 4.9 show the vessel motions and end bending stresses of the riser, respectively. Significant reduction in bending stresses at both ends of the riser was achieved when set-point chasing control was activated. As shown in Figure 4.9, the maximum absolute value of end bending stresses after activating set-point chasing control is 52 MPa. The corresponding von Mises stress computed by (4.3) is 137.4 MPa, which is below the allowable stress ($C_f\ C_a\sigma_y$) given in (4.3). This demonstrates the effect of the proposed control strategy.
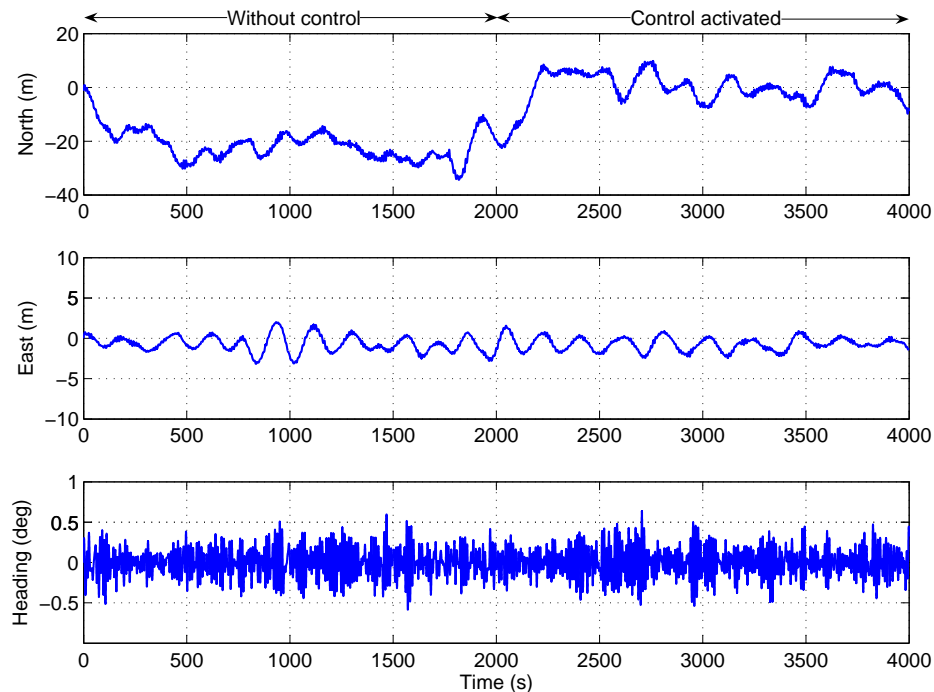
Figure 4.8. Vessel motion in surge, sway and yaw
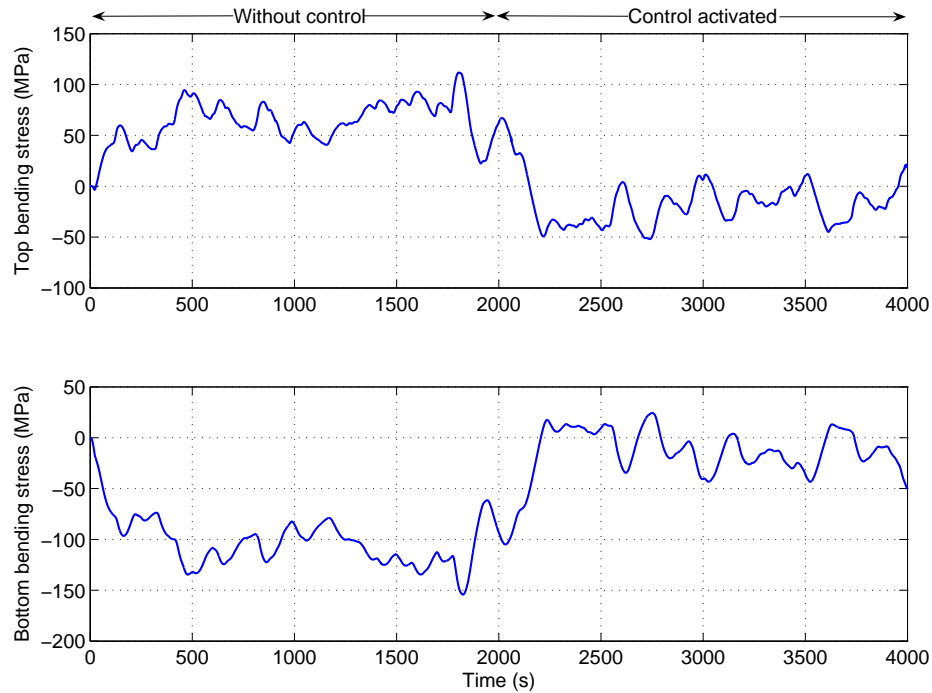
Figure 4.9. Bending stresses at top and bottom end of riser

The different line lengths generated after activating the controller are shown in Figure 4.10. In Figure 4.11, snapshots of the riser profile in the simulations are shown. It is noted that the profile in Figure 4.11 is slightly different with that in Figure 4.5. As the riser end connections are rigid, the angles at both ends are then forced to constantly zero. Figure 4.12 shows the time history of bending stresses along the riser (node 43: near the top end, node 24: at the middle and node 6: near the bottom end). Prior to automatic control (that is, before 2000 s), the riser profiles are on the right at a significant deviation from the vertical position. The bending stresses corresponding to these profiles are shown in Figure 4.12, which can be as high as 3.2 MPa, 4.6 MPa and 5.2 MPa at nodes 6, 24 and 43 respectively. After 2000s when automatic control is activated, the riser profile is closer to the vertical and on the left of Figure 4.11. The bending stresses are significantly reduced where maximum values of 1.8 MPa, 2.8 MPa and 3.4 MPa are obtained at nodes 6, 24 and 43 respectively. The corresponding von Mises equivalent stresses including radial, hoop and axial stresses computed by using (4.3) are 93 MPa, 90.4 MPa and 89.1 MPa. This is below the maximum tensile and compressive yield stresses of the riser material given in (4.3). The riser length is very much larger than the riser diameter. Hence the maximum bending stress normally

occurs at both ends where the bending stiffeners located. For other locations along the riser, the bending stresses are quite similar to that obtained from the case of hinge connection at both ends (REA control).
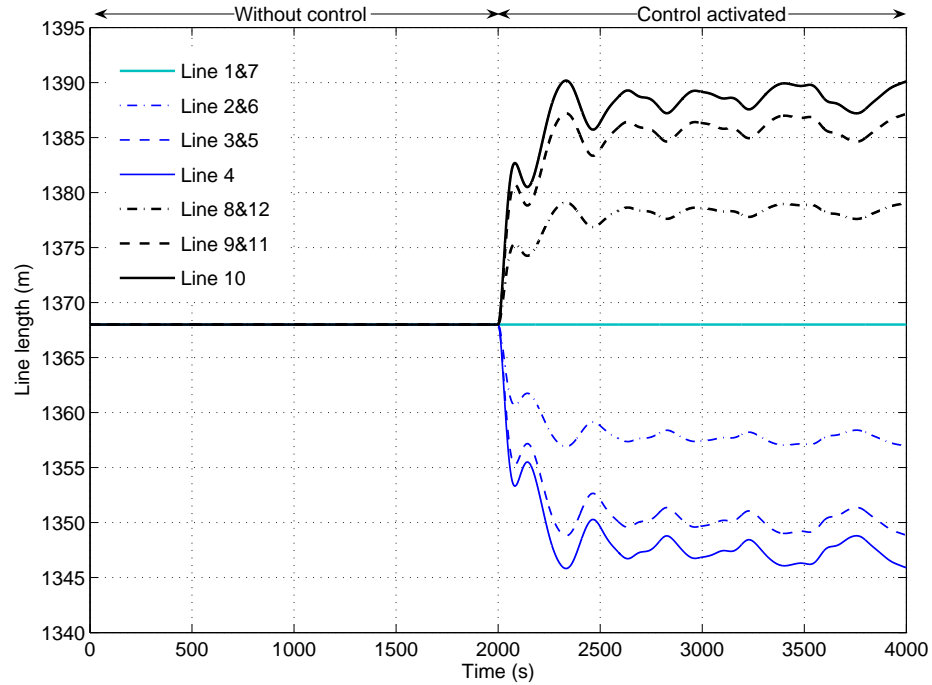
Figure 4.10. Variation of line lengths in PM control
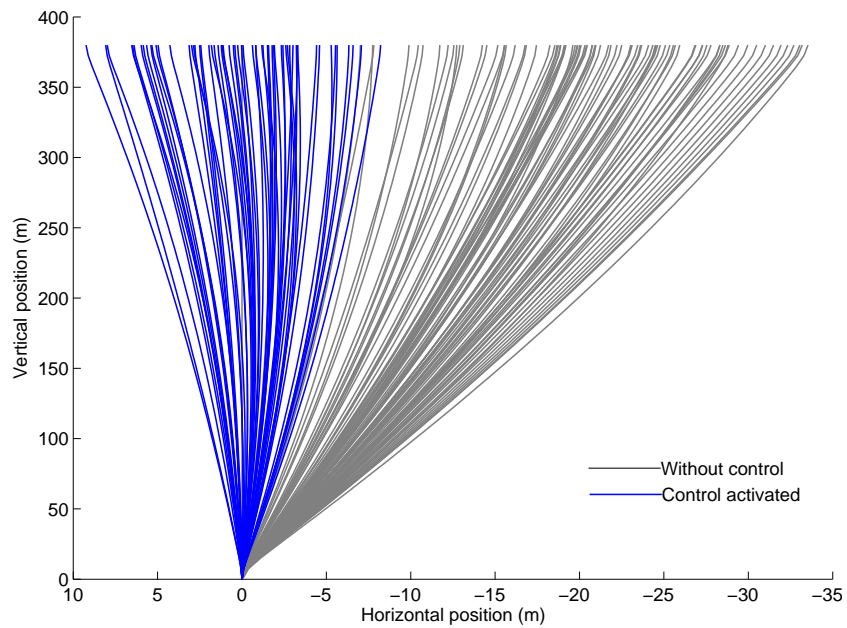
Figure 4.11. Riser snapshots (rigid connection at both ends)
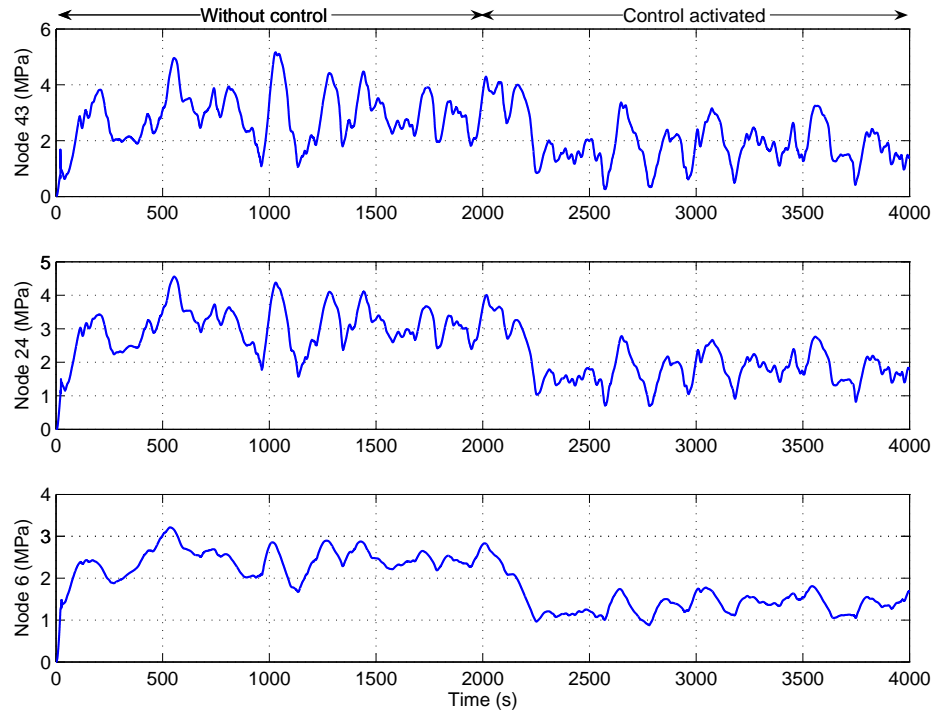
Figure 4.12. Time history of bending stresses along riser

4.5   Conclusions

In this chapter, the suitability of the control algorithm for PM system proposed in Chapter 3 was examined with regards to the bending stresses induced in the riser. For the case where the riser is hinge-connected at the sea bed and to the vessel, using REA control leads to lowering of the bending stresses along the riser. Hence, if the REAs corresponding to the maximum allowable stresses are established, the appropriate limiting REAs can be imposed as the control criterion which will ensure that the critical stress value is not exceeded. The second case considers the use of bending stiffeners to increase and distribute bending stiffness in specific areas of flexible riser pipes as well as to provide a gradual transition between the flexible pipe and the rigid well-head. The REAs are virtually zero and hence bending stresses are used as the criterion in the control algorithm. The optimal set-point is based on the incremental displacement computed using end bending stresses rather than end angles. The simulation results illustrate the effectiveness of the control and reducing the stresses

signification such that it is below the maximum allowable tensile and compressive stresses.

CHAPTER 5. CONTROL OF POSITION MOORING SYSTEMS IN ICE-COVERED SEA

5.1   Introduction

The Arctic region still remains one of the "last frontiers" for the search of oil and gas. According to Kuehnlein et al. (2009), the Arctic region is one of the most difficult areas to work in due to its remoteness, extreme cold, and presence of dangerous sea ice. Figure 5.1 shows the Canmar Explorer I drill ship, which is one of the early drill ships operating in the Arctic region.

Figure 5.1. Canmar Explorer I drill ship in Beaufort Sea (http://www.mms.gov)

Traditionally, DP systems are designed for open water conditions. Therefore, their design and operation under ice conditions remains a challenging issue, yet to be adequately proven as optimal or safe compared to non-ice conditions. The application of PM systems is relatively more popular in the Arctic region. Bonnemaire et al. (2007) pointed out that moored floating vessel concepts may show to be the most attractive solutions in an Arctic environment. Although there are several examples of moored systems in ice-covered sea, little has been done up to now in terms of active control of the vessel motions. Similarly, few (if any) studies have been conducted on the control of riser end angles (REAs) in PM systems under ice-covered sea. During

operation under ice conditions, ice-breakers are normally employed manually to mitigate ice impact. Usually, there are some operational delays until the ice condition improves. Therefore, operational downtime can be significant.

The work in this chapter is motivated by the potential of keeping the downtime low through the use of PM system with automatic control to maintain small REAs during operation under ice impact. The mathematical model of level ice following Nguyen et al. (2009a) is adopted to simulate the ice-vessel interaction. Since the sea state is generally calm in ice-covered sea (Hinkel et al., 1988), a low frequency wave model is employed in the simulation of the system dynamics. The proposed PM control is numerically investigated using a drill ship operating in and out of level ice regime. The simulations are conducted using the Marine System Simulator (MSS) developed by the Norwegian University of Science and Technology (NTNU).

5.2   Level Ice Load Model

Nguyen et al. (2009a) proposed a mathematical model for simulating the behaviour of a DP vessel operating in level ice. The derivations was mainly based on the ice-breaking process and calculations given by Kerr (1976), Enkvist et al. (1979), Lindqvist (1989), Valanto (2001) and Wang (2001). Recently, Biao et al. (2010) used an ice failure model similar to that derived in Wang (2001) to simulate ship maneuvers in level ice. Normally forces acting on vessels of a moving ice plate depend primarily on the physical concepts of ice-hull interaction. The detailed icebreaking process (see Figure 5.2) was presented in Valanto (2001). When the ice plate first comes into contact with the ship hull, some initial crushing failures occur at the ice edge. This results in force component at the contact surface along and perpendicular to the plane of the ice sheet. Crushing continues with increasing contact area and reactive force from the vessel. The vertical component of the force induces bending moment on the ice sheet increasing from zero at the contact surface. When the force is sufficiently large such that the flexural capacity of the ice is exceeded at some distance away from the contact surface, the ice will break. The broken piece of ice will then rotate and slide along the wet surface of the hull until it is fully submerged. It then continues to slide underneath the hull until it loses contact and leaves the hull.
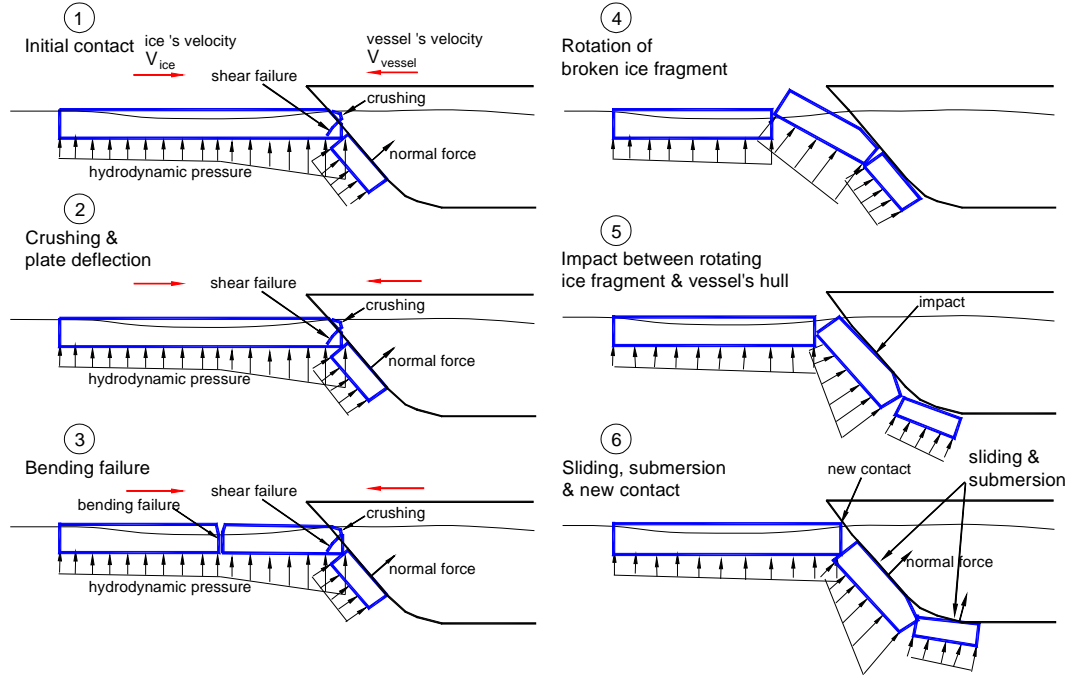
Figure 5.2. Ice-breaking process

To derive an expression for the ice loads acting on the hull, some assumptions are adopted as follows:

- The level ice is a semi-infinite plate moving at a constant speed relative to the Earth-fixed frame.
- The crushing ice load increases linearly from zero at the instant of contact to the value when breakage due to bending occurs.
- The contact surface between vessel hull and ice is flat during crushing.
- The shape of a broken ice floe in bending mode is circular, known as haft-moon shaped piece (Valanto, 2001).
- The ice load caused by bending, submersion, and motion (velocity dependence) is constant and can be calculated from the ice resistance (Lindqvist, 1989).

Based on the above, the ice load can be simplified as the sum of various components. The first component is the vector of ice crushing load (in units of force), denoted as $\boldsymbol{\tau}_{\mathrm{cr}} = [\tau_{\mathrm{cr}}^{X}, \tau_{\mathrm{cr}}^{Y}, \tau_{\mathrm{cr}}^{Z}, \tau_{\mathrm{cr}}^{K}, \tau_{\mathrm{cr}}^{M}, \tau_{\mathrm{cr}}^{N}]^{\mathrm{T}}$, in which $\tau_{\mathrm{cr}}^{X}, \tau_{\mathrm{cr}}^{Y}, \tau_{\mathrm{cr}}^{Z}$ are the corresponding

forces in and $\tau_{cr}^{K}, \tau_{cr}^{M}, \tau_{cr}^{N}$ the corresponding moments about the *X*, *Y*, *Z* axes respectively.

The second component is the resistance provided by the ice sheet against flexural failure. Lindqvist (1989) presented an empirical expression for this component of ice resistance, given by

$$R_{\mathrm{b}} = 0.003\sigma_{\mathrm{f}} BH_{\mathrm{ice}}^{1.5}\left(\tan\psi_{\mathrm{ves}} + \mu_{\mathrm{ice}}\frac{\cos\phi_{\mathrm{ves}}}{\sin\alpha_{\mathrm{ves}}\cos\psi_{\mathrm{ves}}}\right)\left(1+\frac{1}{\cos\psi_{\mathrm{ves}}}\right) \qquad (5.1)$$

where σ_{f} is the bending strength of ice, *B* the breadth of the vessel, H_{ice} the ice thickness, μ_{ice} the friction coefficient between the vessel hull and ice, ϕ_{ves} the stem angle, α_{ves} the waterline entrance angle, ψ_{ves} the slope angle of vessel hull defined as the angle between the normal of the vessel hull and vertical. According to Lindqvist (1989), the slope angle is slightly different from the stern angle and can be determined from the stern angle and waterline entrance angle (ψ_{ves} = atan(tanϕ_{ves} / sinα_{ves}). The main dimensions and angles are illustrated in Figure 5.3.

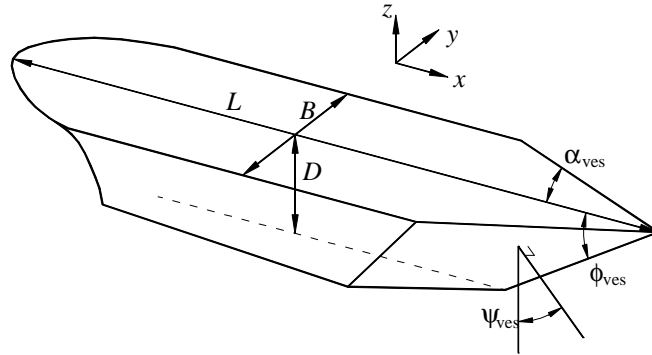
Figure 5.3. Model of vessel hull form

Another component of ice resistance is that against submersion, which in effect is a horizontal force exerted by the ice. The total submersion resistance R_{s} is calculated as the sum of the resistance against the loss in potential energy of the submerged ice floes and the friction between the ice floes and the hull (Lindqvist, 1989), given by

$$R_{s} = \delta_{\rho} g H_{ice} B \left[D \frac{B+D}{B+2D} \right.$$
$$\left. + \mu_{ice} \left(0.7L - \frac{D}{\tan \phi_{ves}} - 0.25 \frac{B}{\tan \alpha_{ves}} + D \cos \phi_{ves} \cos \psi_{ves} \sqrt{\frac{1}{\sin^{2} \phi_{ves}} + \frac{1}{\tan^{2} \alpha_{ves}}} \right) \right] \tag{5.2}$$

where δ_{ρ} is the density difference between water and ice, g the acceleration of gravity, D the draft of the vessel and L the length of the vessel.

Lindqvist (1989) recognized the forces due to flexural failure and submersion seem to increase fairly linearly with the speed. An additional empirical term was proposed to account for the speed dependence of these resistances, given by

$$R_{v} = 1.4 v_{ice} \frac{R_{b}}{\sqrt{gH_{ice}}} + 9.4 v_{ice} \frac{R_{s}}{\sqrt{gL}} \tag{5.3}$$

where v_{ice} is the velocity of the ice floe.

Hence, the final expression for the load due to level ice experienced by the hull is approximated as

$$\tau_{ice} = \tau_{cr} + \mathbf{R}_{b,s,v} \tag{5.4}$$

where $\mathbf{R}_{b,s,v}$ the vector of the ice resistances due to bending and submersion coupled with motion, given by

$$\mathbf{R}_{b,s,v} = [R_{b} + R_{s} + R_{v}, 0, 0, 0, 0, 0]^{T} \tag{5.5}$$

In this study, it is assumed that the ice sheet and ship are moving in the same direction (X-direction). In such a case, the forces R_{b}, R_{s} and R_{v} describe the resistances of the ship in ice and these forces are expressed in the direction of ship and ice motion. The difference between the model and actual measurement is illustrated in Figure 5.4. The figure clearly shows the icebreaking process described in Figure 5.2. When there is contact between the ice sheet and vessel hull, the ice edge is initially crushed at the ice cusp resulting in localized failure (Stage 1). The local crushing continues until the contact zone is sufficient to initiate a global failure, which produces an ice floe (Stage 2). The crushing force then reaches the maximum value (Stage 3). Subsequently, the ice floe rotates, slide and clear away from the vessel hull (Stages 4 and 6). In the ice load given by Valanto (2001), there is a second force peak in the icebreaking process. According to Valanto (2001), this force peak is caused by the sudden change of the

rotary motions of the ice floe at the end of the icebreaking cycle. However for simplicity, the second force peak in the ice load is usually not modeled since it is complicated and the first peak is much more significant. In many recent models of ice load, such as in Wang (2001), Riska (2007), Nguyen et al. (2009), Biao et al. (2010) and Liu et al. (2010), the second peak is not mentioned. Instead, only the first maximum value in the ice crushing process is considered for simulating the ice-vessel interaction. The methodology for simulating dynamic crushing load in time, τ_{cr}, is presented in the following subsections.
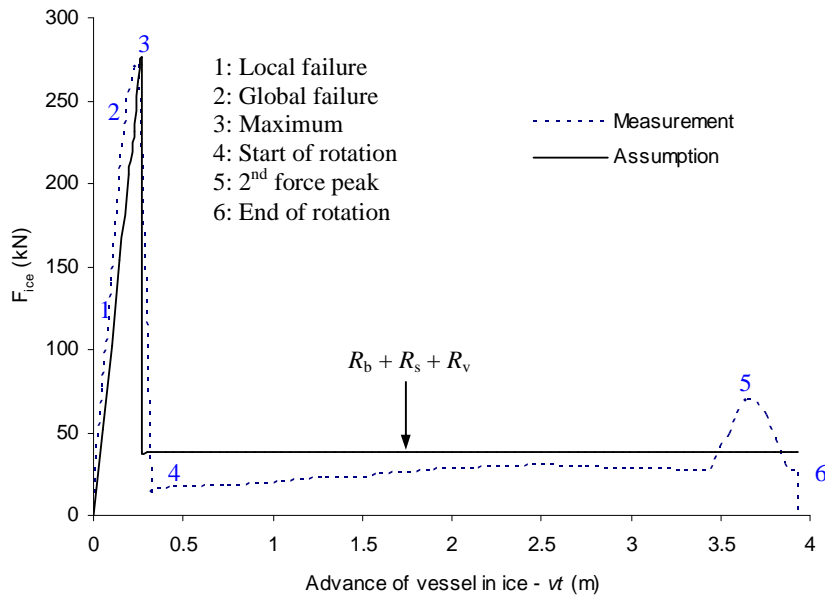
Figure 5.4. Assumed and measured (Valanto, 2001) level ice loads on vessel hull

5.2.1 Determination of Contact

The vessel hull and ice edge are discretized into a number of nodes in the simulation program written for this research. The nodal coordinates are defined in the ice fixed frame, as shown in Figure 5.5. The matrix $\mathbf{x}_{ves} \in \mathbb{R}^{N_{ves} \times 2}$ defines the x, y-position of the vessel hull nodes; and the matrix $\mathbf{x}_{ice} \in \mathbb{R}^{N_{ice} \times 2}$ defines the x, y-position of the ice edge nodes; where N_{ice} is the number of ice nodes, and N_{ves} is the number of vessel nodes. At each time step, the distance between the jth ice node and the kth vessel node, D_{jk}, is calculated and checked for contact between the vessel hull and the ice edge.

Figure 5.5 shows the updated ice edge after there are some crushing failures and broken ice pieces in the ice sheet. The initial ice edge is assumed in regular shape (horizontal line) when contacting the vessel hull.
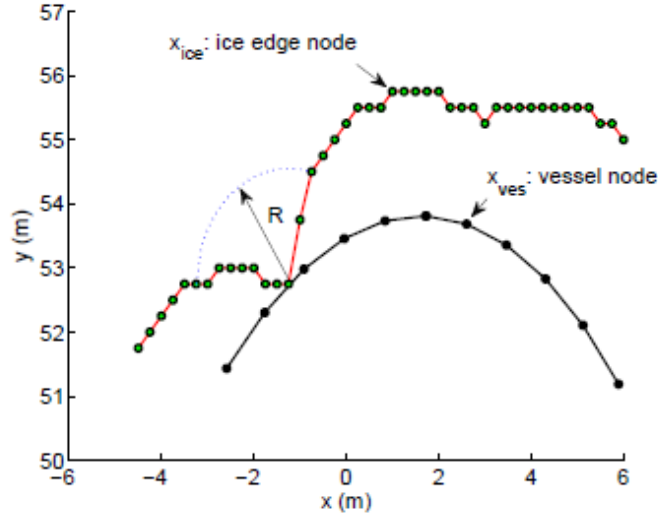
Figure 5.5. Discretization of vessel hull and ice edge (Nguyen et al., 2009a)

5.2.2 Crushing and Bending Failure

Before flexural bending failure, crushing failure occurs first. The crushing force normal to the contact area is given by (Wang, 2001)

$$\tau_{cr}^n = \sigma_c A_c \tag{5.6}$$

where σ_c is the crushing strength of ice and A_c is the contact area.

At each time step, when crushing occurs, the ice edge will penetrate the waterline of the vessel hull. The computation of contact area can be divided into two different possibilities shown in Figure 5.6 as.

$$
\begin{aligned}
A_c &= \frac{1}{2} B_c \frac{L_c}{\cos\psi_{ves}} \quad \text{if } L_c \tan\psi_{ves} \leq H_{ice} \\[2mm]
A_c &= \frac{1}{2}\left(B_c + B_c \frac{L_c - H_{ice}/\tan\psi_{ves}}{L_c} \right) \frac{H_{ice}}{\sin\psi_{ves}} \quad \text{if } L_c \tan\psi_{ves} > H_{ice}
\end{aligned}
\tag{5.7}
$$

where B_c is the length of crushing area determined from the distance between adjacent hull nodes, L_c the crushing depth determined from the distance between the contacting ice nodes and hull nodes; and ψ_{ves} the slope of the vessel hull (see Figures 5.6 and 5.7).

Figure 5.6. Contact area when crushing

Figure 5.7. Ice wedge and crushing at contact area

As shown in Figure 5.8, the crushing force has a horizontal component τ_{cr}^{hor} and vertical component τ_{cr}^{Z}, which are calculated according to the normal crushing force τ_{cr}^{n} and friction coefficient μ_{ice} between the vessel hull and ice, as follows

$$\tau_{cr}^{hor} = \tau_{cr}^{t} \sin\left(\psi_{ves} + \gamma\right) \tag{5.8}$$

$$\tau_{cr}^{Z} = \tau_{cr}^{t} \cos\left(\psi_{ves} + \gamma\right) \tag{5.9}$$

$$\gamma = \arctan \mu_{ice} \tag{5.10}$$

$$\tau_{cr}^{t} = \tau_{cr}^{n} / \cos \gamma \tag{5.11}$$

Other components of the crushing force vector, i.e. τ_{cr}^{X}, τ_{cr}^{Y}, τ_{cr}^{K}, τ_{cr}^{M}, τ_{cr}^{N}, can be determined from τ_{cr}^{hor} and τ_{cr}^{Z} according to the coordinates of hull nodes in the body-fixed frame.
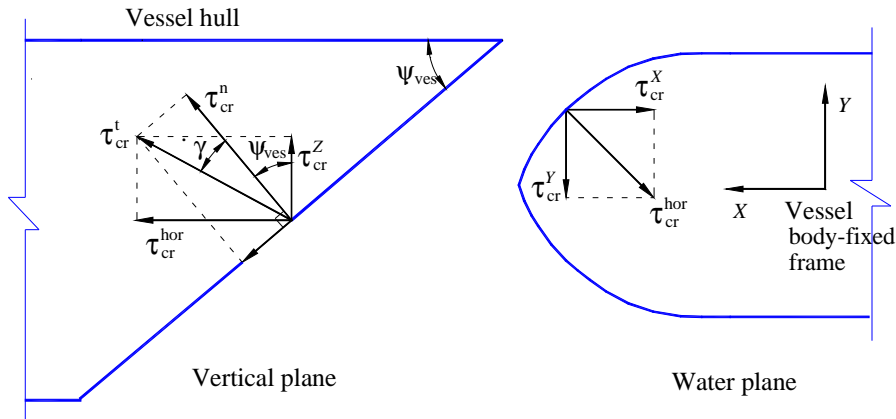
Figure 5.8. Crushing force components

With the vertical component of the crushing force, another failure mechanism comes into play. Theoretically, with a semi-infinite sheet of material where the edge is subjected to a vertical line load, bending moment will be induced with zero value at the edge and increasing with distance away from the load. The same occurs here. When the crushing continues, the vertical force component will increase in magnitude and the induced moment will increase to a point where the ice sheet will break at some distance from the ice-hull contact surface. Kerr (1976) presented Kashtelyan's study on the bearing capacity of floating ice plates which was based on the bending theory of

ice plate on a static foundation. The breaking failure force of an ice wedge with opening angle φ_{ice} (see Figure 5.7) is given by

$$P_{\text{b}} = C_{\text{b}} \left(\varphi_{\text{ice}} / \pi \right)^2 \sigma_{\text{f}} H_{\text{ice}}^2 \tag{5.12}$$

where C_{b} is an empirical parameter which Kerr (1976) proposed as 1/0.966.

In the ice-breaking process, the floes are idealized by ice wedges with a radius which has been proposed by Wang (2001) as

$$R_{\text{break}} = C_{\text{l}} l_{\text{c}} \left(1 + C_{\text{v}} v_{\text{n,rel}} \right) \tag{5.13}$$

where C_{l} and C_{v} are empirical parameters, $v_{\text{n,rel}}$ the normal component of the relative velocity between the ice and hull nodes, and l_{c} the characteristic length of ice which is given by

$$l_{\text{c}} = \left(\frac{E_{\text{ice}} H_{\text{ice}}^3}{12 \left(1 - \upsilon^2 \right) \rho_{\text{w}} g} \right)^{1/4} \tag{5.14}$$

in which E_{ice} is the Young modulus of ice, υ the Poisson coefficient and ρ_{w} the water density.

At each time step, the vertical crushing force and the flexural capacity are used to check whether bending failure has occurred. If the vertical crushing force reaches the failure limit given in (5.12), an ice wedge is created. The ice wedge then rotates and slides along the hull surface. Subsequently, the ice edge is updated to facilitate calculations for the next time step.

5.3   Vessel-ice Interaction Model

Under the ice regime, the sea state is generally calm and the effect of wave is generally not a concern and hence disregarded in the modeling. The low frequency model of the vessel can be written as (Sørensen, 2005b)

$$\mathbf{M}\dot{\mathbf{v}} + \mathbf{C}_{\text{RB}} \left(\mathbf{v} \right) \mathbf{v} + \mathbf{C}_{\text{A}} \left(\mathbf{v}_{\text{r}} \right) \mathbf{v}_{\text{r}} + \mathbf{D} \left(\mathbf{v}_{\text{r}} \right) + \mathbf{G} \left(\boldsymbol{\eta} \right) = \boldsymbol{\tau}_{\text{wind}} + \boldsymbol{\tau}_{\text{moor}} + \boldsymbol{\tau}_{\text{thr}} + + \boldsymbol{\tau}_{\text{ice}} \tag{5.15}$$

where $\boldsymbol{\tau}_{\text{ice}} \in \mathbb{R}^6$ is the vector of level ice load given in (5.4), and the other parameters are defined in (2.50) in Chapter 2.

The dynamic interaction between the vessel and the level ice plate is embedded in (5.15) through the ice load computation and the updating of the vessel kinetics simultaneously, and described in the block diagram of Figure 5.9. As shown in Figures 5.5 and 5.7, the ice edge and vessel hull are discretized into a number of nodes with the coordinates defined by the vectors $\mathbf{x}_{\mathrm{ice}}$ and $\mathbf{x}_{\mathrm{ves}}$ respectively. At a specific time step t_i, the distance between the ice nodes and vessel nodes D_{jk} are calculated to check whether contact occurs. When there is a contact between the ice edge and vessel hull, the crushing and breaking failure forces are calculated according to (5.6) $-$ (5.12). Subsequently, the vertical crushing force τ_{cr}^{Z} and breaking failure force P_{b} are used to check whether the ice sheet is broken. If $\tau_{\mathrm{cr}}^{Z} < P_{\mathrm{b}}$, bending failure is unlikely to occur and the ice sheet is assume to crush at the cusp. The ice node coordinate vector $\mathbf{x}_{\mathrm{ice}}$ remains identical to the previous time step. If $\tau_{\mathrm{cr}}^{Z} \geq P_{\mathrm{b}}$, bending failure occurs. The ice wedge is taken as broken and cleared from the ice sheet. The radius of ice wedge R_{break} is then determined from (5.13) based on the vessel velocity obtained from the previous time step. When an ice breaking event occurs, the remaining ice edge is updated with a new ice edge $\mathbf{x}_{\mathrm{ice}}^{\mathrm{new}}$ based on the radius of ice wedge for checking the next region of contact. The computed ice load is subsequently used to solve for the vessel kinetics at this time step and the process is repeated for the next time step. An example of level ice load with 0.9 m ice thickness acting on the vessel is shown in Figure 5.10. The ice load includes a constant ice resistance and a sequence of crushing events, which are discussed in the previous sections.
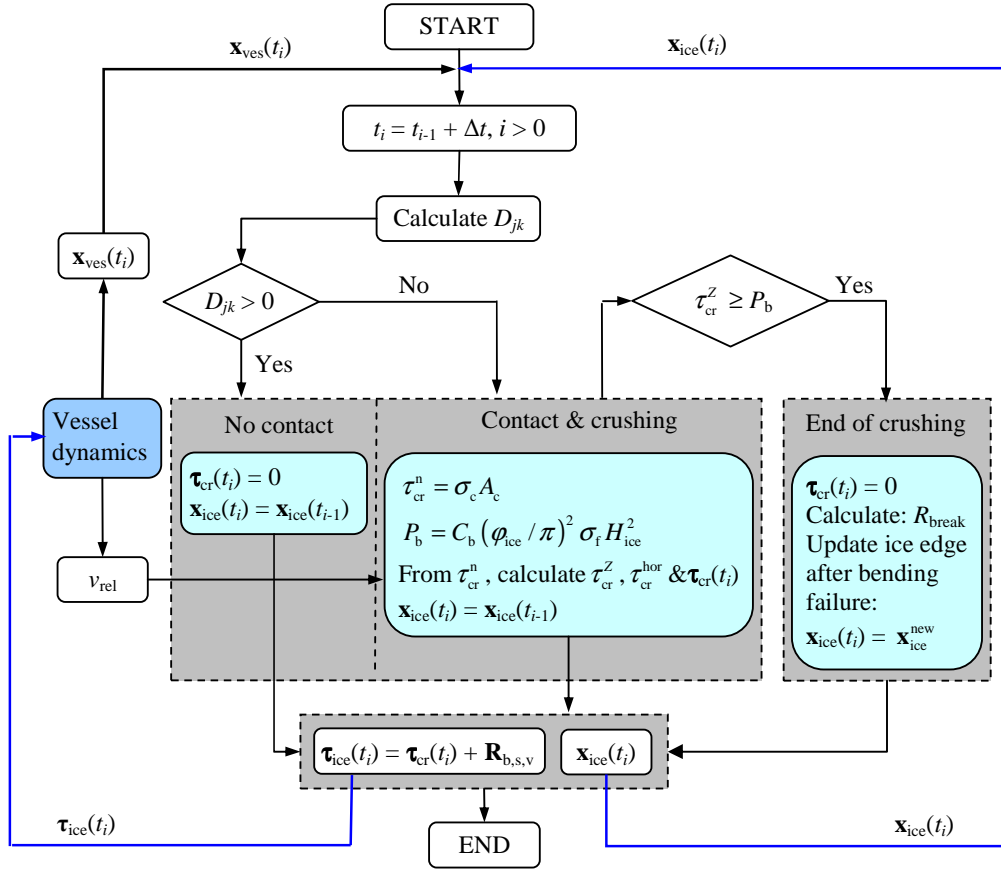
Figure 5.9. Block diagram for simulation of vessel-ice interaction
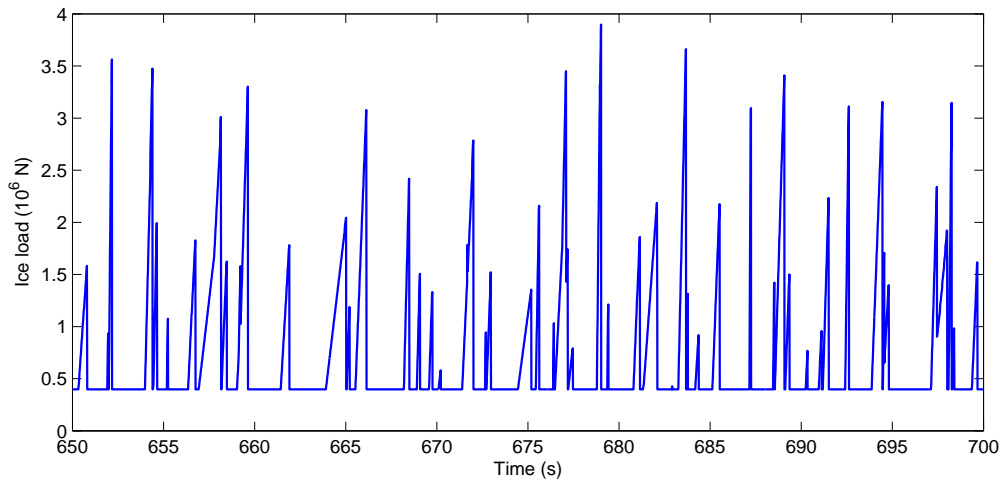

Figure 5.10. Periodicity of level ice forces in a 0.9m thick ice

5.4   Numerical Example

Numerical simulations of an eight-line moored drill ship operating in ice-covered sea with 100 m water depth (see Figure 5.11) are carried out to demonstrate the effect of PM control algorithm proposed in Chapter 3, in which the mean drift motion is controlled by changing the length of each mooring line. To determine the desired position of vessel, the optimal control criterion based on the REAs is adopted.
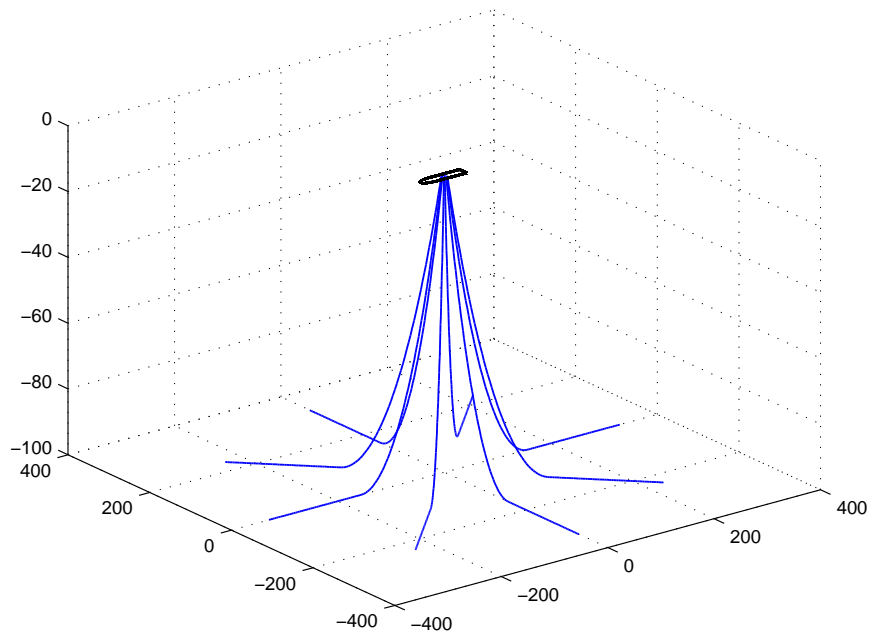
Figure 5.11. Eight-line mooring system configuration in 100m water depth

The drill ship used in the simulations is the Vidar Viking operating in the Arctic region. The main parameters of the drill ship are given in Table 5.1. The mooring system consists of 8 cables connected to the drill ship through the turret, with anchor points distributed evenly on a circle, as shown in Figure 5.12. Each line is a chain which has an average diameter of 0.08 m and length of 356 m. The drill ship operates at a water depth of 100 m and has a riser which is subjected to a vertical tension of 23 tons at its top end. Detailed specifications of the riser are given in Table 5.2.
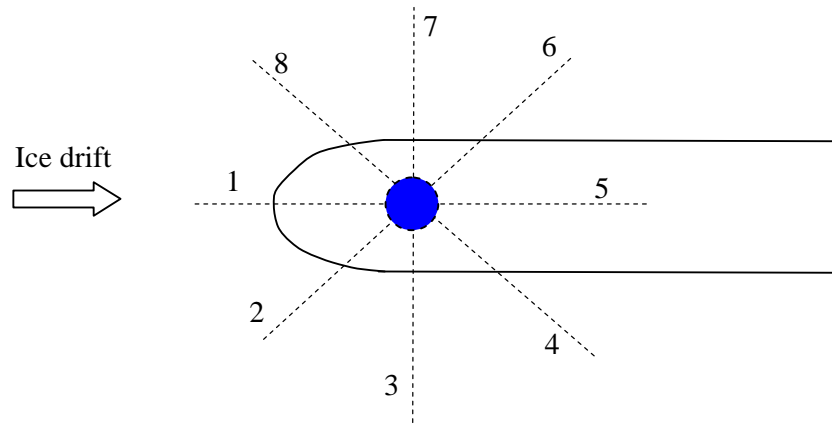
Figure 5.12. Moored vessel with 8 anchor lines used in simulations

Table 5.1. Drill ship's main parameters

Parameter	Unit	Value
Mass	ton	3382
Overall length	m	83.7
Breadth	m	18
Design draught	m	6
Stem angle	degree	45
Average waterline entrance angle	degree	61
Slope angle of vessel hull	degree	64

Table 5.2. Properties of riser

Parameter	Unit	Value
Top tension	ton	23
Modulus of elasticity	10^7 kN/m^2	20.2
Sea water density	kg/m^3	1025
Riser pipe density	kg/m^3	7850
Mud density	kg/m^3	800
Outer diameter	m	0.3
Inner diameter	m	0.285
Added mass coefficient		2
Normal drag coefficient		1
Total submerged weight of riser (including mud)	ton	3.5

The vessel is exposed to different ice thicknesses in which the thickness changes from small thickness (0.6 m) to larger thickness (0.9 m and 1.2 m). The ice parameters are shown in Table 5.3. The open water regime is described by the JONSWAP-distributed wave with a significant wave height, H_s = 2 m and wave period, T_p = 8.78 s; wind velocity, v_{10} = 7.65 m/s and surface current velocity, v_c = 0.7 m/s. The corresponding ice drift velocity is 0.7 m/s. The level ice regime consists of wind, current and level ice loads. The simulations are conducted using the Marine Systems Simulator (MSS) developed by Fossen and Perez (2004) at the Norwegian University of Science and Technology (NTNU). In this study, the multi-cable mooring system, riser FEM (50 beam elements) and level ice models are added to the original MSS to execute the proposed control strategy of the vessel-mooring-riser system in ice regime.

Table 5.3. Ice parameters

Parameter	Unit	Value
Bending strength	10^3 kN/m^2	0.5
Crushing strength	10^3 kN/m^2	2.86
Friction coefficient		0.2

The following four cases are simulated for comparison:

1. Case 1: Without control (denoted as "no control").
2. Case 2: PM control algorithm proposed in Chapter 3 ("proposed").
3. Case 3: Modified DP control for ice conditions ("modified DP").
4. Case 4: Conventional DP control for open water ("conventional DP").

The conventional DP found in the literature is a well established system in open water, which may be difficult to adopt for operations in ice. In a recent study, Nguyen et al. (2009a) modified the conventional DP control to extend its operation in level ice regime. The results of Nguyen et al. (2009a) showed that the modified DP control enables the system to operate satisfactorily in and out of level ice with thickness of 0.7 m. In this study, the proposed PM control is compared with the modified DP control.

5.5   Simulation Results

5.5.1 Effect of Vessel Offset on REAs

Figures 5.13 and 5.14 show the static deformations of the riser and the REAs under uniform vertical current of 0.7 m/s for various vessel offsets (from 0 m to 10 m) of the drill ship operating in a water depth of 100 m. When the vessel offset is zero, meaning that the vessel is right above the well-head, the bottom and top angles are 1° and -1° respectively, due to riser deformation caused by vertical uniform current of 0.7 m/s. When the vessel offset increases, the REAs also increase, where the bottom and top angles can reach values of 6.6^o and 4.6^o for vessel offset of 10 m. The allowable REA limits (ideally, $\pm2^o$) for continuous drilling operations may thus be exceeded.
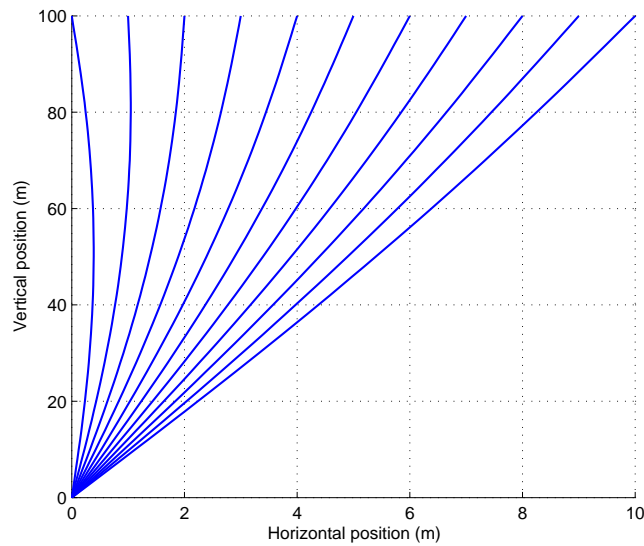

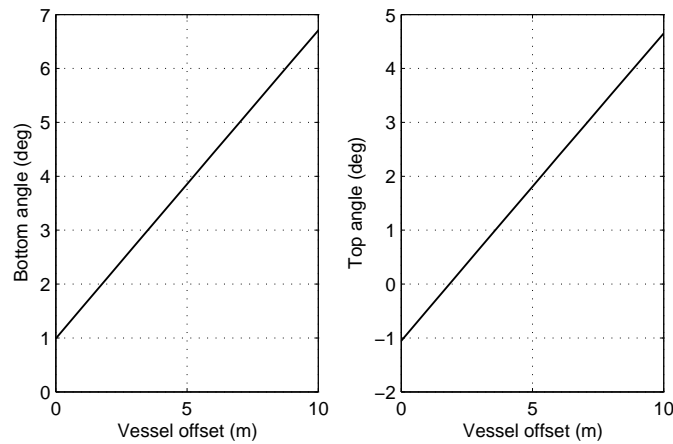Figure 5.13. Riser deflections with different vessel offsets (0 m – 10 m)

Figure 5.14. Bottom and top riser angle with different vessel offsets (0 m – 10 m)

5.5.2 Effect of Position Mooring Control

The model was first simulated without control for the first 200 s, before activating automatic control for the next 1200 s as shown in Figures 5.15 − 5.22. To control both angles, (3.35) was used to obtain the optimal vessel position. The vessel was exposed to open water in the first 400 s and in the last 400 s. In the remaining time, the vessel operated in level ice regime with three cases of ice thickness (0.6 m, 0.9 m and 1.2 m). Figure 5.15 shows the North position of the vessel for the four simulated cases. Figure 5.16 shows the time history of REAs for the four simulated cases.

When there was no control (all line lengths were kept equal at 356 m) and under the large impact of ice movement, the vessel has experienced a drift of up to 10 m (for ice thickness of 1.2 m) with corresponding REAs of 6.6^o for the bottom angle and 5° for the top angle.

When automatic control was activated after 200 s, the optimal set-point was generated based on the measured REAs. The controller activated the vessel to the generated optimal position around the field zero point (Figure 5.15). The results show that the PM control proposed in this study and the modified DP control of Nguyen et al. (2009a) yielded better performances compared to the conventional DP control in terms of less offsets when the environment changed from open water to ice regime with different ice thicknesses (from 0.6 m to 1.2 m). Specifically, as shown in Figure 5.15, when the vessel entered and left the ice regime with different ice thicknesses, the maximum vessel offsets with the proposed PM control are 0.91 m (in 0.6 m ice), 0.9 m (in 0.9 m ice), 1.64 m (in 1.2 m ice) and 2.7 m (in open water). These offsets with the modified DP control are 0.7 m, 0.48 m, 2.55 m and 3.65 m while these offsets with the conventional DP control are 2.8 m, 1.8 m, 3.64 m and 7.55 m. As shown in Figure 5.16, in term of the REA response, performances of the proposed PM control and the modified DP control are also better than the conventional DP control. It is observed that with PM control, the REAs were kept within the acceptable range of $\pm 2^o$, indicating the feasibility of the control strategy of mooring lines proposed in this study.
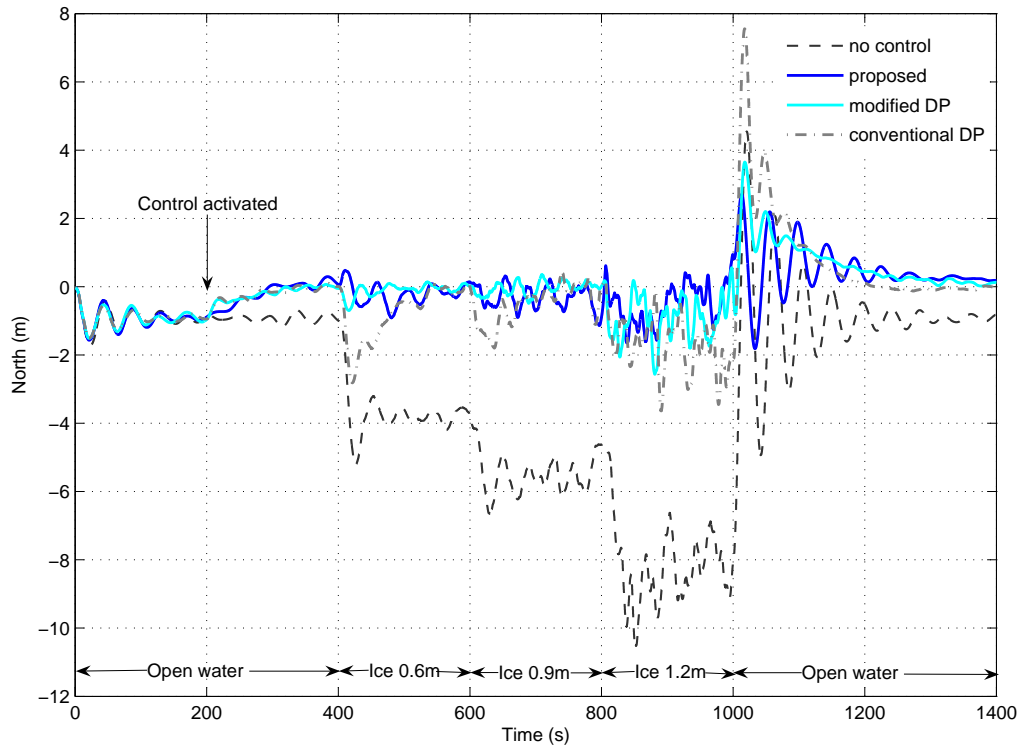
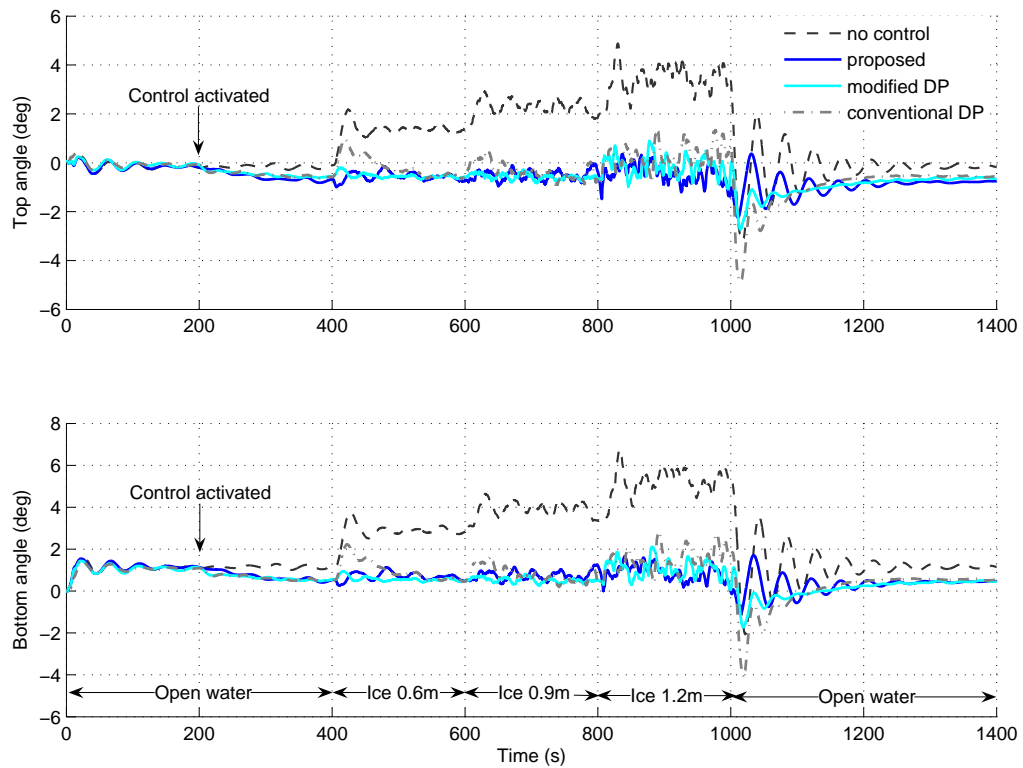Figure 5.15. North position of vessel

Figure 5.16. Time history of top and bottom end riser angles

The initial length of each mooring line is 356 m. In PM control, when the set-point chasing was activated, the line lengths are automatically adjusted to generate the required forces to counteract the impact caused by level ice drifts as well as maintain the mean position at the optimal set-point generated from (3.35). Different line lengths generated after activating the PM control are shown in Figure 5.17. The ice loads with respect to three different ice thicknesses are shown in Figure 5.18. These loads include a constant ice resistance and a sequence of crushing events, which are discussed in the previous sections. Figure 5.19 indicates that line breakage may be prevented during control operations since there was no significant change in the tension of mooring lines compared to uncontrolled case. For the chain with 0.08 m diameter used in the simulation, the breaking strength is 6.5×10^6 N. According to API (1996), the maximum tension of mooring lines is required to be less than 50% of the breaking strength in intact conditions. As shown in Figure 5.19, the maximum tension occurs in the case of maximum ice contact (1.2 m ice thickness). The values are 1.44×10^6 N and 1.35×10^6 N with respect to the uncontrolled and controlled cases. These tensions are less than 3.25×10^6 N, which satisfies the requirement of API (1996). In addition, the changes in the tensions are relatively less rapid for the controlled case.
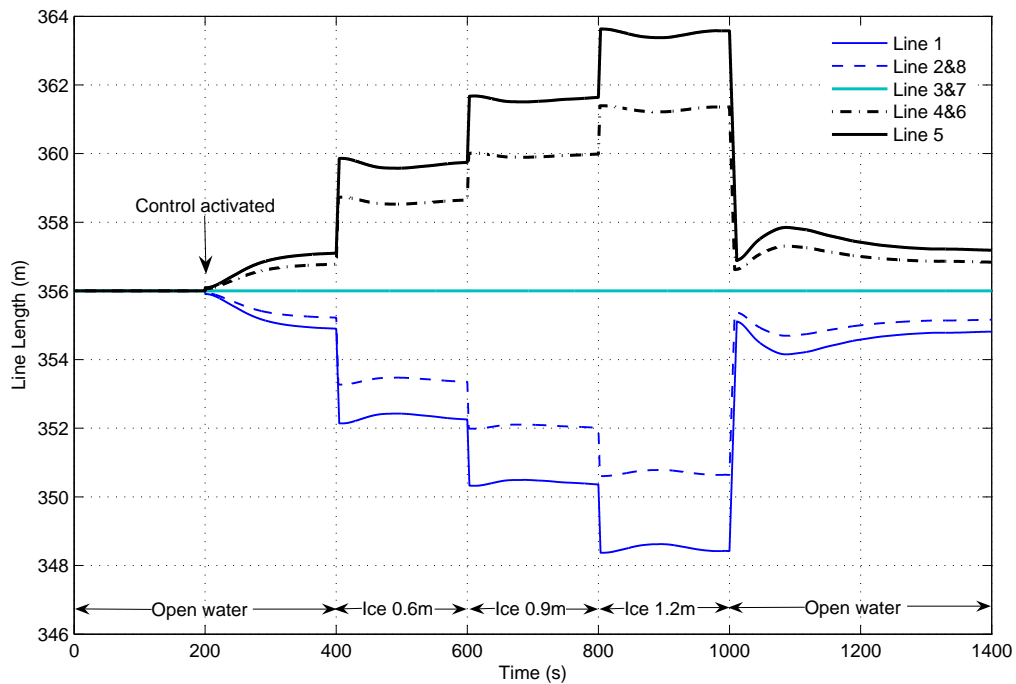
Figure 5.17. Variation of line lengths in proposed PM control
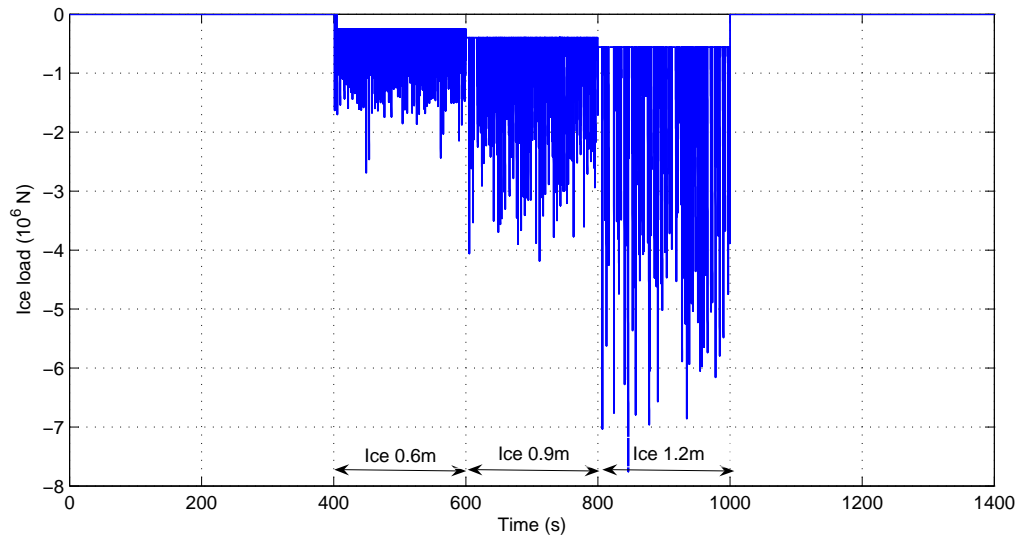
Figure 5.18. Ice load of 0.6 m, 0.9 m and 1.2 m level ice
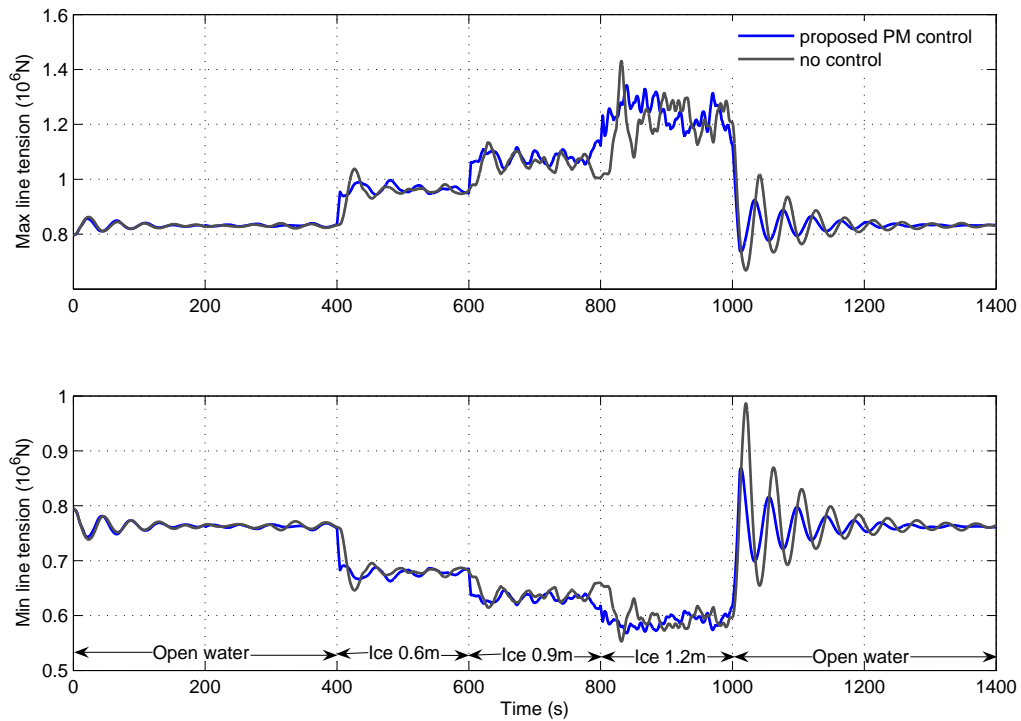
Figure 5.19. Time history of maximum and minimum tension of mooring lines

In Figure 5.20, snapshots of the riser profile from the simulations are shown. The effectiveness of the control is shown clearly by the fact that before control the riser profile can vary widely. With the optimal set-point chasing algorithm, the riser profile is maintained close to the vertical around the well-head, ensuring small REAs.
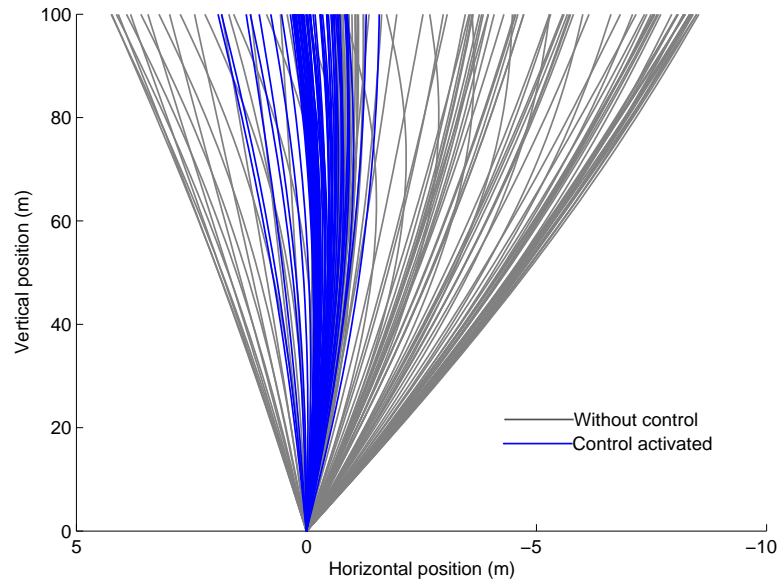
Figure 5.20. Riser snapshots under vessel motions

Figure 5.21 shows the bending stress profiles where the maximum values without and with control are 15 MPa and 37 MPa respectively. Figure 5.22 gives the time history of bending stresses along the riser at node 5 (near the bottom end), node 26 (at the middle) and node 45 (near the top end). As shown in Figure 5.22, during PM control (Case 2) operation, the bending stresses along the riser are considerably smaller than those of Case 1 (without control). Thus with control, savings through the optimal use of materials is possible and can be significant.
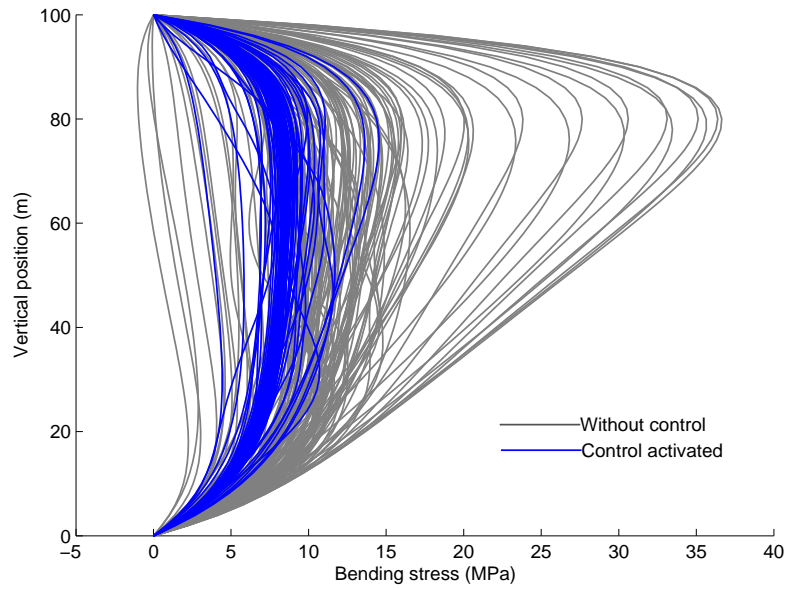
Figure 5.21. Bending stress profiles corresponding to riser snapshots
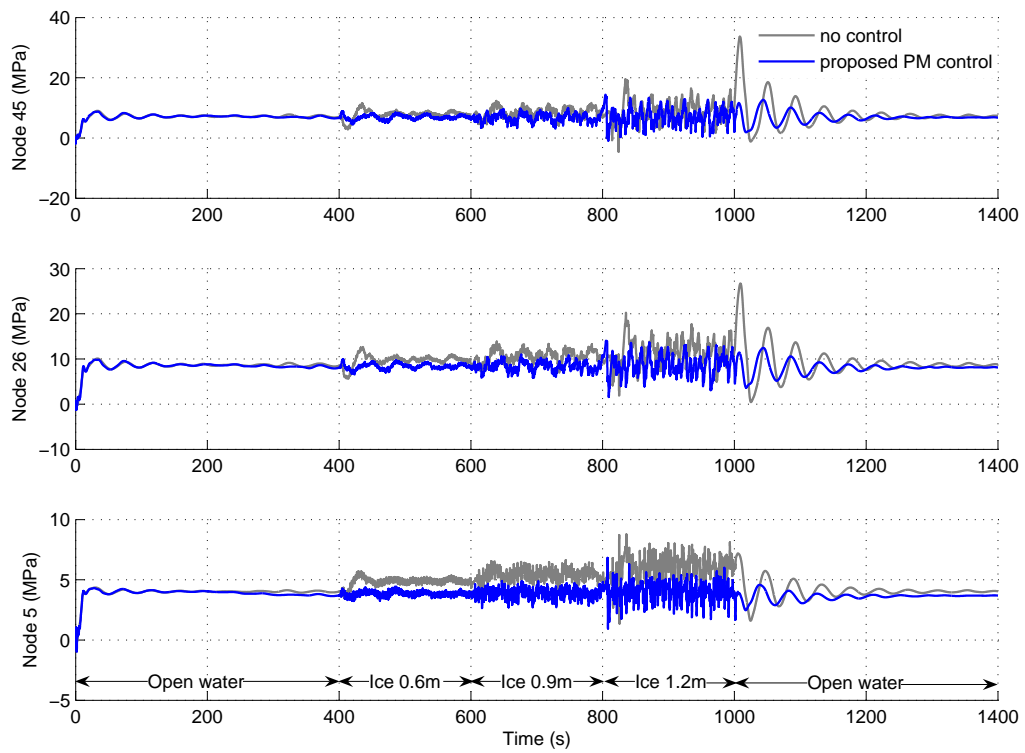
Figure 5.22. Time history of bending stresses along riser

5.6   Conclusions

In this chapter, the control strategy for PM system proposed in Chapter 3 was tested in the level ice regime. An optimal set-point chasing algorithm based on the REAs as the control criterion was adopted to obtain the desired vessel positions. The performance of PM control was compared with the modified and conventional DP introduced by Nguyen et al. (2009a). The ice load model, which was mainly based on the calculations of Nguyen et al. (2009a), was used to simulate the vessel-ice interaction. The vessel was first exposed to open water and then exposed to level ice with different ice thicknesses. Simulation results indicated that the PM control proposed in this study and the modified DP control of Nguyen et al. (2009a) obtained better performances than the conventional DP control for open water. The REAs and bending stresses along the riser are reduced considerably under control operations, which showed the effectiveness of the set-point chasing algorithm.

Under the ice regime, the sea state is generally calm and the effect of wave is generally not a concern while the other environmental loads from wind and ocean current are similar to that in open water. An additional challenge comes from the ice drift force, which causes large impact on the vessel. In the proposed control strategy, the observer filters out the WF responses due to the short impulses of ice load and only the LF responses enter the control loop. Subsequently, the controller lets the mooring lines counteract the ice drift force and maintains the vessel at appropriate positions. According to Kuehnlein et al. (2009), it is so difficult to adopt the conventional DP for operation in ice. Hence, moored floating vessels may be attractive strategy for operations in ice regime.

CHAPTER 6. CONCLUSIONS AND FUTURE WORKS

6.1   Summary of Key Points

The main objective of this study is to propose a control strategy to minimize the riser end angles (REAs) of position mooring (PM) system when the riser is exposed to ocean currents and vessel motions. This study focused on maintaining the drilling vessel in an appropriate position rather than top tension control to maintain the REAs within an allowable range.

The mathematical model of the riser, mooring system and vessel system was presented. The mooring forces were formulated as position-dependent external forces based on a quasi-static approach where the catenary equation of cable was employed. A FEM model comprising beam elements that include the flexural stiffness was adopted for the marine riser operating in shallow water. Both low frequency (LF) and wave frequency (WF) motions of the hull were imposed on the riser at the top end as externally defined oscillations.

To obtain zero steady-state error in surge, sway and yaw, the integral controller was designed for PM system and the REA criteria were used to compute the optimal vessel positions. The mean offset was compensated by adjusting the lengths of the mooring lines.

The strategy was numerically simulated using the Marine Systems Simulator (MSS) developed by Fossen and Perez (2004) at the Norwegian University of Science and Technology (NTNU). Experimental tests using the model vessel, Cybership 3, which is a 1:120 scaled model of the vessel in the numerical simulation, were carried out in the Marine Cybernetics Laboratory (MCLab) at NTNU. The results were compared with those obtained in the simulations.

The generalization of the control algorithm for PM system was also extended to take into account the bending stresses of the riser when controlling the vessel positions using the criteria based on the REAs. Two cases were considered, namely, where both ends of the riser were (a) hinge-connected (which is normally assumed for simplicity), and (b) connected with bending stiffeners. The main purpose of the bending stiffener was to provide a gradual transition between the flexible pipe and the rigid well-head. It

also increased and distributed the bending stiffness in specific areas of flexible riser pipes.

The control strategy for PM system proposed herein was studied for its applicability in ice-covered sea in view of increasing oil and gas operations in the Arctic region. The ice load model of Nguyen et al. (2009a) was used to simulate the vessel-ice interaction which took into account the coupling between the vessel motion and the ice-breaking process. To validate the control performance in ice-covered sea, the vessel was first exposed to open water and then exposed to the level ice regime with different ice thicknesses. The performances of the PM control was compared with those of the conventional DP control for open water and the modified DP for level ice proposed by Nguyen et al. (2009a).

6.2   Conclusions

From the numerical simulations for PM vessels, the controller was able to automatically adjust the vessel position to reduce the REAs by controlling the lengths of the mooring lines. Basically, the mooring system provided the mean force to compensate the mean drift loads of the environment due to ocean wind, wave and current. When the vessel oscillations became significant, additional damping was compensated by the thrusters. The results indicated that by letting the line tensioning counteract the mean loads arising from the disturbances, compared to the case of using thruster control continuously for both position and heading as in DP systems, fuel consumption is reduced.

The experimental results agreed well with those obtained in the simulations. During the tests, the controller was able to generate the necessary changes in mooring line lengths to obtain the appropriate vessel positions and yet the changes of line lengths did not contain significant oscillations. Hence, the wear and tear of mooring lines was somewhat minimized with lower energy and yet able to fulfill the control objective.

For the extension to study the control of bending stresses with REAs, the simulation results showed that the mean value of LF bending stresses along the riser was also reduced when the vessel moved to the optimal position generated by the REA criteria. For the case when bending stiffeners were provided, the end angles were forced to be constantly zero. The allowable stresses rather than allowable angles

seemed to dominate the control action. Based on the simulation results, the bending stresses at both ends of the riser is similar to that obtained for the case of using REAs only without bending stiffener.

For application of the control strategy in ice-covered sea, the simulation results indicated that like the modified DP for level ice, the proposed PM control performed better than conventional DP when the vessel moved to level ice regime. This finding is relevant to drilling and work over operations since the sea condition in ice regime is normally calm and the fuel consumption is relatively low for moored vessel using the proposed control strategy in normal sea states.

6.3   Recommendations for Further Work

Based on the findings of this study, some recommendations are given for further work on this subject:

- Generally, the numerical and experimental results have confirmed the actual implementation of the control strategy proposed in this study. However, this effectiveness of this control strategy for extreme sea states may need to be further investigated. In such sea states, thruster operations may be intensive to reduce considerable vessel oscillations and require high fuel consumption. Secondly, the risk of mooring line breakage has to be investigated.

- In the experimental tests, the depth of the water basin was restricted to 1.5m which might not have simulated all the dynamic effects of a real riser. Further tests in deeper water tanks should be carried out where possible to ascertain the accuracy of this study.

- The control concept was validated by the experimental tests in this study. Analytical studies of the robustness and stability of the proposed procedures need to be carried out.

- The present study of the PM control in the ice regime may show a potential of considerable applications for oil and gas exploration in ice-covered sea. Besides level ice condition, other aspects such as ice ridge issues which cause sudden large impacts to drilling vessel should be included in further studies of PM systems.

- Additional experimental tests would be important to validate the actual implementation of the proposed PM control strategy for riser bending stresses and ice-covered sea.

REFERENCES

[1]   Aamo O. M. and Fossen T. I. (1999). Controlling line tension in thruster assisted mooring systems. *In Proceeding of the 1999 IEEE, International Conference on Control Applications*, pp. 1104–1109.

[2]   Aamo O. M. (1999). *Adding mooring systems to the ABB Integrated Vessel Simulator – Implementation*. Department of Engineering Cybernetics, NTNU, Trondheim, Norway.

[3]   Aamo O. M. and Fossen T. I. (2001). Finite element modelling of moored vessels. *Mathematical and Computer Modelling of Dynamical Systems,* Vol. 7, No. 1, pp. 47–75.

[4]   Admad S. and Datta T. K. (1989). Dynamic response of marine risers. *Engineering Structures*, Vol. 11, pp. 179–188.

[5]   API – American Petroleum Institute (1977). *Bulletin on comparison of marine drilling riser analyses*. API Bulletin 2J, 1st edition, January.

[6]   API – American Petroleum Institute (1996). *Recommended practice for design and analysis of station keeping systems for floating structures*. Recommended practice 2SK, 2nd edition, December.

[7]   API – American Petroleum Institute (1998). *Design of risers for floating production systems (FPSs) and tension-leg platforms (TLPs)*. Recommended practice 2RD, 1st edition.

[8]   Biao S., Riska K. and Moan T. (2010). A numerical method for the prediction of ship performance in level ice. *Journal of Cold Regions Science and Technology*, Vol. 60, pp. 177–188.

[9]   Bonnemaire B., Jensen A., Gudmestad O. T., Lundamo T. and Løset S. (2007). Oil and gas developments in Arctic and cold regions - Challenges related to station keeping in ice. *9th annual INTSOK Conference*, Houston, Texas, USA, March.

[10] Burke B. G. (1973). An analysis of marine risers for deep water. *The 5th Offshore Technology Conference*, OTC 1771, Houston, Texas, USA, April 29–May 2.

[11] Chen Q. (2001). *Analysis and control of riser angles*. Master thesis, Department of Marine Structures, Faculty of Marine Technology, NTNU, Trondheim, Norway.

[12] Chen Y. H. (1987). General nonlinear analysis of marine risers. *IEEE Journal of Ocean Engineering*, pp. 527–529.

[13] Chen Y. H. and Lin F. M. (1989). General drag-force linearization for nonlinear analysis of marine risers. *Ocean Engineering*, Vol. 16, No. 3, pp. 265–280.

[14] Clough R. W. and Penzien J. (2003). *Dynamics of structures*. McGraw-Hill, Inc., New York.

[15] DNV – Det Norske Veritas (2004). *Position mooring*. Offshore Standard DNV-OS-E301, October.

[16] Do K. D. and Pan J. (2008a). Boundary control of transverse motion of marine risers with actuator dynamics. *Journal of Sound and Vibration*, Vol. 318, pp. 768–791.

[17] Do K. D. and Pan J. (2008b). Nonlinear control of an active heave compensation system. *Ocean Engineering*, Vol. 35, pp. 558–571.

[18] Do K. D. and Pan J. (2009). Boundary control of three-dimensional inextensible marine risers. *Journal of Sound and Vibration*, Vol. 327, pp. 299–321.

[19] Ellwanger G. B., Lima E. P., Siqueira M. Q. and Casaprima H. (1991). Lanczos-Ritz modal dynamic analysis of marine rigid risers. *Proceedings of the first International Offshore and Polar Engineering Conference*, Vol. 2, pp. 178–181, Edinburg, United Kingdom, August 11–16.

[20] Engseth A., Bech A. and Larsen C. M. (1988). Efficient method for analysis of flexible risers. *BOSS 88*, pp. 1357–1371, Trondheim, Norway.

[21] Enkvist E., Varsta P. and Riska K. (1979). The ship – ice interaction. *In the proceeding of 5th International Conference on Port and Ocean Engineering under Arctic Conditions (POAC79)*, pp. 977–1002, Trondheim, Norway.

[22] Faltinsen O. M. (1990). *Sea loads on ships and offshore structures*. Cambridge University Press, Cambridge.

[23] Faltinsen O. M. and Løken A. E. (1979). Slow-drift oscillations of a ship in irregular wave. *Applied Ocean Research*, Vol. 1, No. 1, pp. 21–31.

[24] Fard M. P. and Sagatun S. I. (2001). Exponential stabilization of a transversely vibrating beam by boundary control via Lyapunov's direct method. *Journal of Dynamic Systems, Measurement and Control*, Vol. 123, No. 10, pp. 195–200.

[25] Fard M. P. (2001). *Modelling and control of mechanical flexible systems*. PhD thesis, Department of Engineering Cybernetics, Norwegian University of Science and Technology, Trondheim, Norway.

[26] Fossen T. I. (1994). *Guidance and control of ocean vehicles*. John Wiley and Sons Ltd, New York.

[27] Fossen T. I. (2002). *Marine control systems: Guidance navigation and control of ships rigs and underwater vehicles*. Marine Cybernetics, Trondheim, Norway.

[28] Fossen T. I. and Perez T. (2004). Marine Systems Simulator (MSS). <www.marinecontrol.org>.

[29] Fossen T. I. and Strand J. P. (1999). Passive nonlinear observer design for ships using Lyapunov methods: full-scale experiments with a supply vessel. *Automatica*, Vol. 35, No. 1, pp. 3–16.

[30] Fung P. T. K. and Grimble M. J. (1983). Dynamic ship positioning using self-tuning Kalman filter. *IEEE Transaction, Automatic Control*, Vol. 28, No. 3, pp. 339 – 349.

[31] Fylling I. J., Larsen C. M., Sødahl N., Omberg H., Engseth A. G, Passano E. and Holthe K. (2005). *Theory manual RiflexTM-34-rev0*. SINTEF Marintek. Trondheim, Norway.

[32] Ghadimi R. (1988). A simple and efficient algorithm for the static and dynamic analysis of flexible marine risers. *Computer and Structures*, Vol. 29, No. 4, pp. 541–555.

[33] Grimble M. J., Patton R. J. and Wise D. A. (1980). The design of dynamic ship positioning control systems using stochastic optimal control theory. *Optimal Control Applications & Methods*, Vol. 1, pp. 167–202.

[34] Grimble M. J. and Johnson M. A. (1988). *Optimal control and stochastic estimation: Theory and applications*. John Wiley and Sons, UK.

[35] Guedes C., Fonseca N. and Pascoal R. (2005). Experimental and numerical study of the motions of a turret moored FPSO in waves. *Journal of Offshore Mechanics and Arctic Engineering*, Vol. 127, No. 10, pp. 197–204.

[36] Hansen E. H. and Løset S. (1999). Modelling floating offshore units moored in broken ice: comparing simulations with ice tank tests. *Journal of Cold Regions Science and Technology*, Vol. 29, pp. 107–119.

[37] Hinkel R. M., Thibodeau S. L. and Hippman A. (1988). Experience with drillship operations in the U.S. Beaufort Sea. *The 20th Offshore Technology Conference*, OTC 5685, Houston, Texas, USA, May 2 – 5.

[38] Huang T. and Kang Q. L. (1991). Three dimensional analysis of a marine riser with large displacements. *Proceedings of the first International Offshore and Polar Engineering Conference*, Vol. 2, pp. 170–177, Edinburgh, United Kingdom, August 11 – 16.

[39] Huang T. and Chucheepsakul S. (1985). Large displacement analysis of a marine riser. *Journal of Energy Resources Technology, ASME*, Vol. 107, pp. 54–59.

[40] Isherwood M. A. (1972). Wind resistance of merchant ships. *Transactions Institution of Naval Architects, RINA*, Vol. 115, pp. 327–338.

[41] Jacobsen A. H. (2006). *Observer design for risers on TLPs*. Master Thesis, Department of Marine Technology, Norwegian University of Science and Technology, Trondheim, Norway.

[42] Johansen T. A., Fugleseth T. P., Tøndel P. and Fossen T. I. (2007). Optimal constrained control allocation in marine surface vessels with rudders. *Control Engineering Practice*, Vol. 16, No. 4, pp. 457–464.

[43] Kaewunruen S., Chiravatchradej J. and Chucheepsakul S. (2005). Nonlinear free vibrations of marine risers/pipes transporting fluid. *Ocean Engineering*, Vol. 32, pp. 417–440.

[44] Keinonen A., Wells H., Dunderdale P., Pilkington R., Miller G. and Brovin A. (2000). Dynamic positioning operation in ice, Offshore Sakhalin, May-June 1999. *Proceedings of the 10th International Offshore and Polar Engineering Conference*, Vol. 1, pp. 683–690, Seattle, USA, May 10 – June 2.

[45] Kerr A. D. (1976). The bearing capacity of floating ice plates subjected to static or quasi-static loads. *Journal of Glaciology*, Vol. 17, No. 76, pp. 229–268.

[46] Kirk C. L., Etok E. U. and Cooper M. T. (1979). Dynamic and static analysis of a marine riser. *Applied Ocean Research*, Vol. 1, No. 3, pp. 125–135.

[47] Kirk C. L. (1985). Dynamic response of marine risers by single wave and spectral analysis methods. *Applied Ocean Research*, Vol. 7, No. 1, pp. 2–13.

[48] Kordkheili S. A. H. and Bahai H. (2007). Non-Linear Finite Element Static Analysis of Flexible Risers with a Touch Down Boundary Condition. *Proceedings of the 26th International Conference on Offshore Mechanics and Arctic Engineering*, San Diego, California, USA, June 10 – 15.

[49] Krolikowski L. P. and Gay T. A. (1980). An improved linearization technique for frequency domain analysis. *Offshore Technology Conference*, OTC 3777, pp. 341–347, Houston, Texas, USA, May 5 – 8.

[50] Kuehnlein W. L., sea2ice and HSVA (2009). Philosophies for dynamic positioning in ice-covered waters. *Offshore Technology Conference*, OTC 20019, Houston, Texas, USA, May 4 – 7.

[51] Langley R. S. (1984). The linearization of three-dimensional drag force in random seas with current. *Applied Ocean Research*, Vol. 6, No. 3, pp. 126–131.

[52] Larsen C. M. (1976). Marine riser analysis. *In Norwegian Maritime Research,* No. 4, pp. 15–26, Oslo, Norway.

[53] Larsen C. M. (1992). Flexible Riser Analysis – Comparison of Results from Computer Programs. *Marine Structures*, Vol. 5, pp. 103–119.

[54] Leira B. J. (1987). Multidimensional stochastic linearization of drag forces. *Applied Ocean Research*, Vol. 9, No. 3, pp. 150–162.

[55] Leira B. J., Sørensen A. J. and Larsen C. M. (2004). A reliability-based control algorithm for dynamic positioning of floating vessels. *Structural Safety*, Vol. 26, pp. 1–28.

[56] Lindqvist G. (1989). A straightforward method for calculation of ice resistance of ships. *In the proceeding of 10th International Conference on Port and Ocean Engineering under Arctic Conditions (POAC89)*, pp. 722–735, Lulea, Sweden.

[57] Liu J., Lau M. and Williams F. M. (2010). Mathematical modelling of ice-hull interaction for ship maneuvering in ice simulations. *The 7th International Conference and Exhibition on Performance of Ships and Structures in Ice*, Alaska, USA, September 20 – 23.

[58] Løset S., Kanestrøm Ø. and Pytte T. (1998). Model tests of a submerged turret loading concept in level ice, broken ice and pressure ridges. *Journal of Cold Regions Science and Technology*, Vol. 27, pp. 57–73.

[59] Moran K., Backman J. and Farrell J. W. (2006). Deepwater drilling in the Arctic Ocean's permanent sea ice. *In Proceedings of the Integrated Ocean Drilling Program (IODP)*, Vol. 302.

[60] Nguyen T. D. (2004). *Observer design for mechanical systems described by semilinear partial differential equations*. PhD thesis, Department of Engineering Cybernetics, Norwegian University of Science and Technology, Trondheim, Norway.

[61] Nguyen T. D., Sørbø A. H. and Sørensen A. J. (2009a). Modelling and Control for Dynamic Positioned Vessels in Level Ice. *In Proceedings of 8th Conference on Manoeuvring and Control of Marine Craft (MCMC'2009)*, pp. 229–236, Guarujá, Brazil, September 16 – 18.

[62] Nguyen T. D. and Sørensen A. J. (2009b). Switching control for thruster-assisted position mooring. *Control Engineering Practice*, Vol. 17, No. 9, pp. 985–994.

[63] Nguyen T. D. and Sørensen A. J. (2009c). Set-point chasing for thruster-assisted position mooring. *Journal of Ocean Engineering*, Vol. 34, No. 4, pp. 548–558.

[64] Nilsen T. (2003). *Development of Cybership III*. Master Thesis. Department of Marine Technology, NTNU, Trondheim, Norway.

[65] O'Brien P. J. and McNamara J. F. (1989). Significant characteristics of three-dimensional flexible riser analysis. *Engineering Structures*, Vol. 11, pp. 223–233.

[66] Patel M. H., Sarohia S. and Ng K. F. (1984). Finite-element marine riser analysis of the marine riser. *Engineering Structures,* Vol. 6, No. 2, pp. 175–184.

[67] Patel M. H. and Jesudasen A. S. (1987). Theory and model tests for the dynamic response of free hanging risers. *Journal of Sound and Vibration*, Vol. 112, No. 1, pp. 149–166.

[68] Perez T. and Blanke M. (2003). DCMV a Matlab/Simulink® Toolbox for Dynamics and Control of Marine Vehicles. *In the proceedings of 6th IFAC Conference on Manoeuvring and Control of Marine Craft, MCMC'03*, Girona, Spain, September 17 – 19.

[69] Perez T., Smogeli Ø. N., Fossen T. I., and Sørensen A. J. (2005). An Overview of Marine Systems Simulator (MSS): A Simulink® Toolbox for Marine Control Systems. *Scandinavian Conference on Simulation and Modeling SIMS05*, Trondheim, Norway, October 13 – 14.

[70] Przemieniecki J. S. (1968). *Theory of matrix structural analysis*. McGraw-Hill, Inc., New York.

[71] Riska K. (2007). *Arctic Structures*. Lecture Notes, Department of Marine Technology, NTNU, Trondheim, Norway.

[72] Rustad A. M., Larsen C. M. and Sørensen A. J. (2008). FEM modelling and automatic control for collision prevention of top tensioned risers. *Marine Structures*, Vol. 21, No. 1, pp. 80–112.

[73] Rustad A. M. (2007). *Modelling and control of top tensioned risers*. PhD thesis, Department of Marine Technology, Norwegian University of Science and Technology, Trondheim, Norway.

[74] SNAME – The Society of Naval Architects and Marine Engineers (1950). Nomenclature for Treating the Motion of a Submerged Body through a Fluid. *In: Technical and Research Bulletin No. 1–5*.

[75] Spanos P. D., Tein W. Y. and Ghanem R. (1990). Frequency domain analysis of marine risers with time dependent tension. *Applied Ocean Research*, Vol. 12, No. 4, pp. 200–210.

[76] Sørdalen O. J. (1997). Optimal thrust allocation for marine vessels. *Control Engineering Practice*, Vol. 5, No. 9, pp. 1223–1231.

[77] Sørensen A. J., Sagatun S. I., and Fossen T. I. (1996). Design of a dynamic position system using model-based control. *Control Engineering Practice*, Vol. 4, No. 3, pp. 359–368.

[78] Sørensen A. J., Strand J. P. and Fossen T. I. (1999). Thruster assisted position mooring system for turret-anchored FPSOs. *In Proceedings of the 1999 IEEE International Conference on Control Applications,* pp. 1110 – 1117, Hawai'i, USA, August 22 – 27.

[79] Sørensen A. J., Leira B., Strand J. P. and Larsen C. M. (2001). Optimal set-point chasing in dynamic positioning of deep-water drilling and intervention vessels. *International Journal of Robust and Nonlinear Control*, Vol. 11, No. 10, pp. 1187–1205.

[80] Sørensen A. J., Pedersen E. and Smogeli Ø. N. (2003). Simulation-Based Design and Testing of Dynamically Positioned Marine Vessels. *In Proceedings of International Conference on Marine Simulation and Ship Maneuverability, MARSIM'03*, Kanazawa, Japan, August 25 – 28.

[81] Sørensen A. J. (2005a). Structural issues in the design and operation of marine control systems. *Journal of Annual Review in Control*, Vol. 29, No. 1, pp. 125–149.

[82] Sørensen A. J. (2005b). *Marine Cybernetics: Modelling and Control*. Lecture Notes, Fifth Edition, UK-05-76, Department of Marine Technology, NTNU, Trondheim, Norway.

[83] Strand J. P., Sørensen A. J. and Fossen T. I. (1997). Modelling and control of thruster assisted position mooring systems for ships. *In Proceedings of the IFAC Conference on Maneuvering and Control of Marine Craft*, pp. 160–165.

[84] Strand J. P., Sørensen A. J. and Fossen T. I. (1998). Design of automatic thruster assisted position mooring systems for ships. *Modelling, Identification and Control*, Vol. 19, No. 2, pp. 61–75.

[85] Strand J. P. (1999). *Nonlinear position control systems design for marine vessels*. PhD thesis, Department of Engineering Cybernetics, Norwegian University of Science and Technology, Trondheim, Norway.

[86] Strand J. P. and Fossen T. I. (1999). Nonlinear passive observer for ships with adaptive wave filtering. *New Directions in Nonlinear Observer Design* (H. Nijmeijer and Fossen T. I., Editors). Chap. I-7, pp. 113–134, Springer-Verlag, London.

[87] Suzuki H., Watanabe K. and Yoshida K. (1995). Operability improvement of deepsea riser by active control. *In Proceedings of OMAE'95, 14th International Conference on Offshore Mechanics and Arctic Engineering*, Vol. 1B, pp. 289–297, Copenhagen, Denmark, June 18 – 22.

[88] Tanaka N. and Iwamoto H. (2007). Active boundary control of an Euler-Bernoulli beam for generating vibration-free state. *Journal of Sound and Vibration*, Vol. 304, pp. 570–586.

[89] Triantafyllou M. S. (1990). *Cable mechanics with marine applications*. Cambridge, MA 02139, Department of Ocean Engineering, Massachusetts Institute of Technology, USA.

[90] Trim A. D. (1990). Time-domain random analysis of marine risers and estimation of non-Gaussian bending stress statistics. *Applied Ocean Research*, Vol. 12, No. 4, pp. 162–174.

[91] Tucker T. C. and Murtha J. P. (1973). Nondeterministic analysis of marine riser. *Offshore Technology Conference*, OTC 1770.

[92] Valanto P. (2001). The resistance of ships in level ice. *SNAME Transactions*, Vol. 109, pp. 53-83.

[93] Wang S. (2001). *A dynamic model for breaking pattern of level ice by conical structures*. PhD thesis. Department of Mechanical Engineering, Helsinki University of Technology, Finland.

[94] Wichers J. E. W. (1993). Position Control – From anchoring to DP system. *New Techniques for Assessing and Qualifying Vessel Stability and Sea keeping Qualities, University Enterprise Training Partnership. UETP, Marine Science and Technology Section 18*, pp. 1 – 23, Trondheim, Norway.

[95] Wright B. (2000). *Full scale experience with Kulluk station keeping operations in pack ice (with reference to Grand Banks Developments)*. Working report 25-44 for the Program of Energy, Research and Development (PERD), National Research Council, Ottawa, Canada, July.

[96] Wu S. C (1976). The effects of current on dynamic response of offshore platforms. *Offshore Technology Conference*, OTC 2540, Houston, Texas, May 3–6.

[97] Yazdchi M. and Crisfeld M. A. (2002). Buoyancy forces and the 2D finite element analysis of flexible offshore pipes and risers. *International Journal for Numerical Methods in Engineering*, Vol. 58, pp. 61–88.

APPENDIX A. MARINE CYBERNETICS LABORATORY (MCLAB) AND CYBERSHIP III MODEL

A.1 Marine Cybernetics Laboratory (MCLab)

The Marine Cybernetic Laboratory (MCLab), which is located at the Department of Marine Technology (NTNU), is a 40 m × 6.45 m × 1.5 m towing tank with an associated control room and a towing carriage, as shown in Figures A.1 − A.3. The laboratory is used for testing sea keeping, fixed and floating offshore structures, and mooring systems. It is also suitable for more specialised hydrodynamic tests, mainly due to the advanced towing carriage, which has capability for precise movement of models in 6 degrees of freedom.
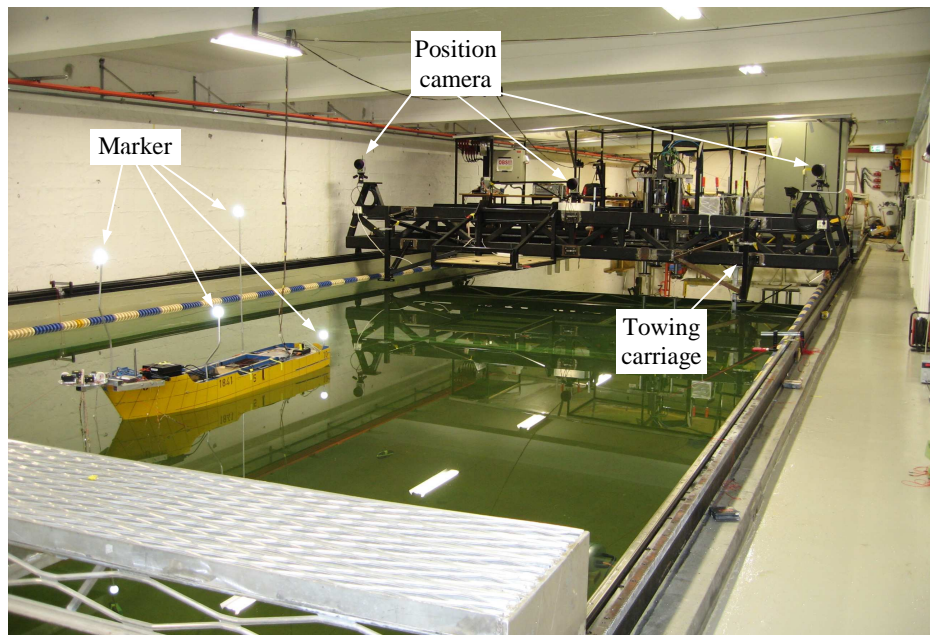

Figure A.1. MCLab at NTNU
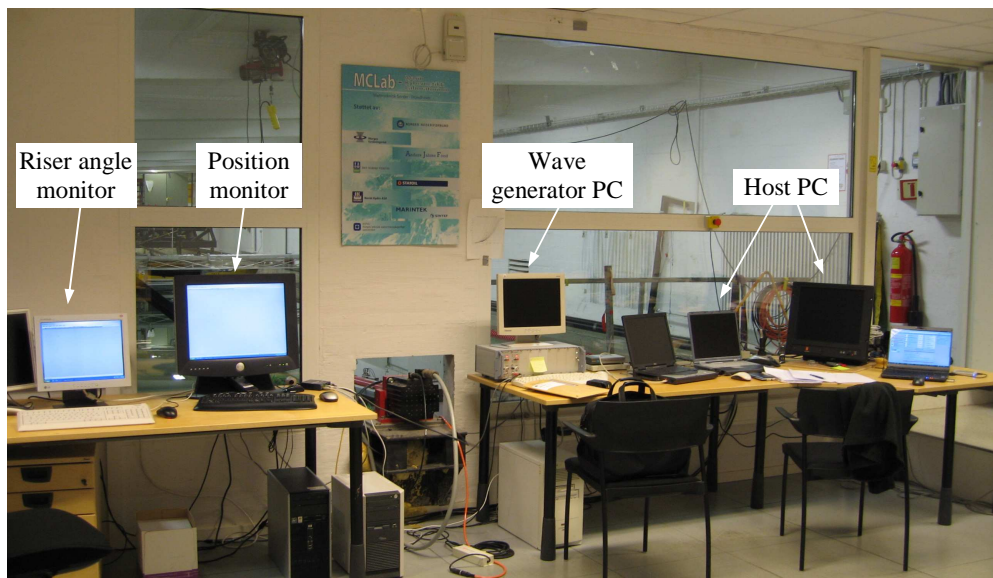
Figure A.2. Close-up view of position camera

Figure A.3. Control room in MCLab

The DHI wave maker at one end of the water tank (Figure A.4) can generate regular and irregular waves with maximum wave height $H_s = 0.3$ m and period $T = 0.6$ – 1.5 s. The position monitoring is performed by a Qualisys monitoring system with three cameras mounted on the towing carriage (Figures A.1 and A.2). The cameras

monitor the position of markers mounted on the vessel (Figure A.1) and transmit data to a computer in the control room (Figure A.3). This computer is installed with Qualisys Track Manager (QTM) software. This software computes the position of the center of gravity (CG) of Cybership III, based on the data from the cameras and predefined distances from the markers to the CG. The calculated position in 6 DOFs is then transmitted to the onboard computer of the vessel. When implementing experimental tests, there is a wireless communication between the onboard computer and the computer in the control room. Positions and control signal are then constantly transmitted to the control room, and users can adjust the control parameters which are transmitted back to the onboard computer. The control interface is loaded into the Opal-RT environment, which governs the communication between the vessel and the control room. The software used in the MCLab was developed using rapid prototyping techniques and automatic code generation under Matlab/Simulink® and Opal-RT. The target computer onboard the vessel runs the QNX real-time operating system while experimental results are presented in real-time on a host computer in the control room.

Figure A.4. Wave generator

A.2 Cybership III Model

The Cybership III (see Figure A.5) using in the MCLab has been developed in cooperation between the Department of Marine Technology and the Department of Engineering Cybernetics at NTNU for testing dynamic position system and navigational system. Details of the project were described in Nilsen (2003). Before the Cybership III, the Cybership I and II have been frequently used, but they both have limitations to their usage due to model size, control method and propulsion system. The Cybership I is a 1:70 scaled model of a thruster controlled supply vessel for DP, having a mass of $m = 17.6$ kg, length $L = 1.19$ m and equipped with 4 controlled azimuth thrusters with independent controllable azimuth angles. The Cybership II is a 1:70 scaled model of a multipurpose supply vessel for DP and tracking control, having a mass of $m = 15$ kg, length $L = 1.15$ m and equipped with 2 aft azimuth thrusters with 2 rudders, 1 fore azimuth thruster and 1 tunnel thruster at the bow.
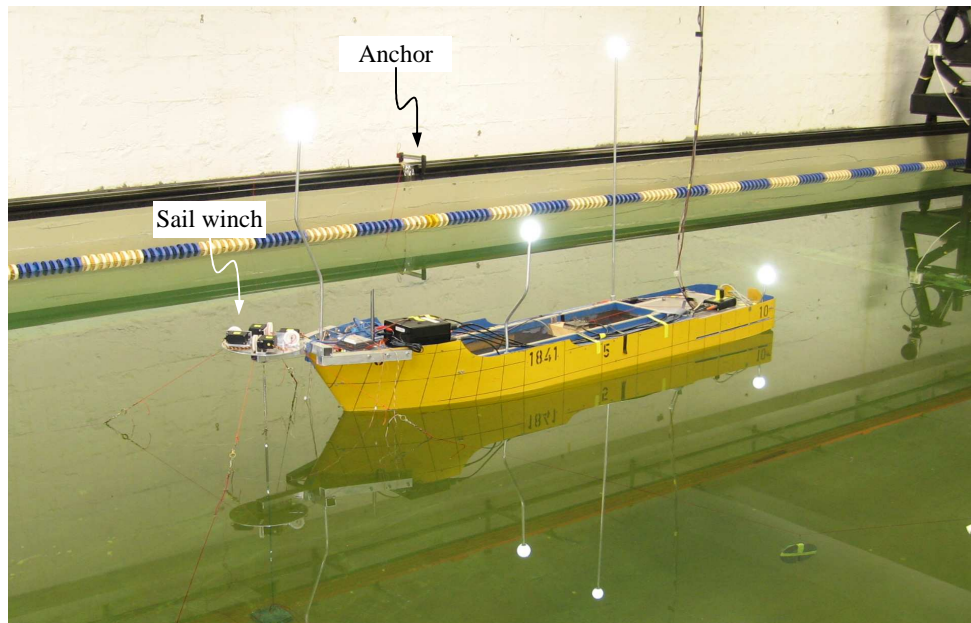

Figure A.5. Cybership III

The Cybership III combined the best parts of its predecessors by using a propulsion system similar to that on the Cybership I and the computer system identical to that on the Cybership II. It is a 1:30 scaled model of a supply vessel, having a mass

m = 75 kg, length L = 2.27 m and breath B = 0.4 m. Mechanical and electric configuration/installation of the Cybership III were developed by Nilsen (2003). The vessel is equipped with two main aft azimuth thrusters, one fore tunnel thruster and one fore azimuth thruster (Figure A.6). The power system includes four 12V-18Ah batteries which can sustain the ship systems for at least one day of experiments without charging. The internal hardware architecture is controlled by an onboard PC which can communicate with an onshore PC through a WLAN. The PC onboard the ship (target PC) uses the QNX real-time operating system. The control system is developed on a PC in the control room (host PC) under Simulink/Opal and downloaded to the target PC using an automatic C-code generation and a wireless Ethernet.
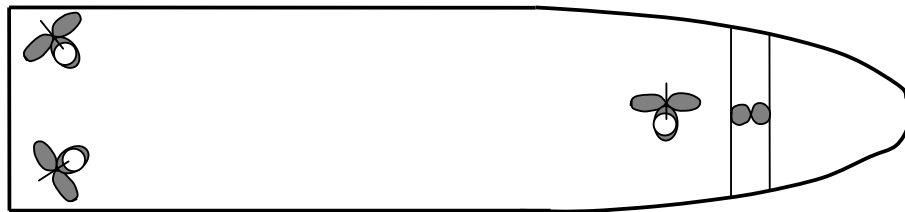

Figure A.6. Two aft azimuth thrusters (left), 1 fore azimuth thruster and 1 fore tunnel thruster (right) of Cybership III

The motion capture unit (MCU) manufactured by Qualysis provides the Earth-fixed position and heading of the vessel. The MCU consists of three onshore cameras mounted on the towing carriage. The cameras emit infrared light and receive the light reflected form the markers on the ship.

In order to test the PM control strategy a turret mooring system was designed and mounted on the Cybership III, as shown in Figure A.7. The mooring system

consists of four mooring lines; each attached at one end to the turret via sail winches, and at the other to an anchor mounted on the tank wall. Strain gauges were attached to the lines to measure the tensions during the experiment. The HITEC HS-785HB sail winches (Figure A.7) installed on the turret of the vessel were used to obtain the required lengths by pulling or releasing the lines. These sail winches are derived forms of heavy duty servo with many advanced features that provide good performance and reliability. Each winch can rotate forward or backward up to 2.5 turns, depending on the input voltage. Each turn will wind about 120 mm of the line. The drilling riser was modelled by a plastic pipe with outer diameter of 6 mm. To provide higher mass, lead was put inside the riser pipe. The riser was subjected to tension at the top, which was modelled by a tensioned spring. The riser was installed just below the turret. In order to measure the REAs, two reflected light markers were attached at the top and bottom of the riser. An underwater camera (see Figure A.8) at the bottom of the water tank was used to capture these marker motions. From these signals, the REAs can be computed.
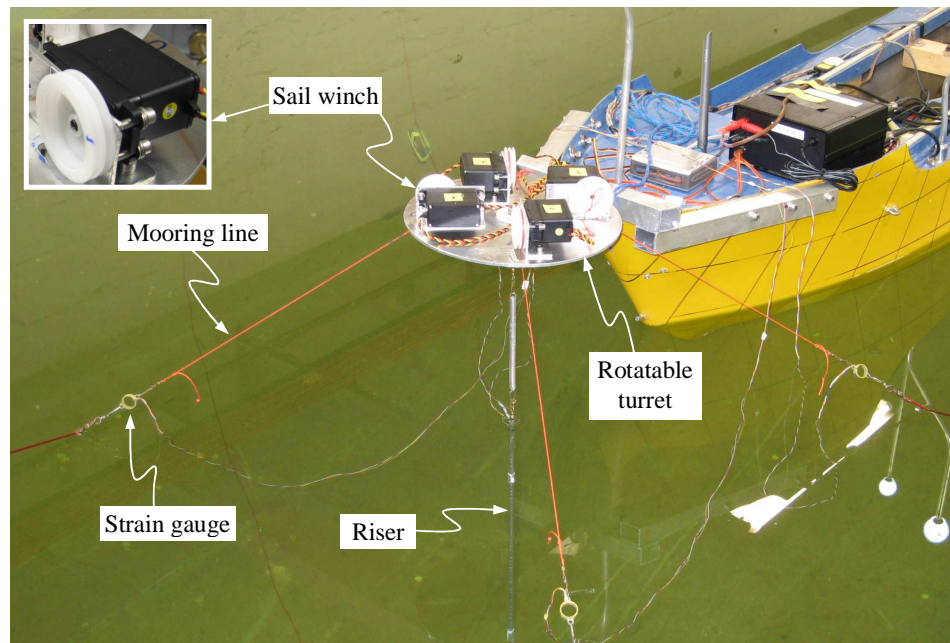

Figure A.7. Mooring turret mounted on Cybership III

Figure A.8. Underwater camera

APPENDIX B. MARINE SYSTEMS SIMULATOR

The Marine Systems Simulator (MSS), which was developed and introduced by Fossen and Perez (2004) at NTNU, is a Matlab/Simulink® library and simulator for marine systems (Figure B.1). It includes models for ships, underwater vehicles, and floating structures. The library also contains guidance, navigation, and control (GNC) blocks for real-time simulation. An overview of the MSS has been presented by Perez et al. (2005). There are three main toolboxes in the MSS: Marine GNC (Guidance and Navigation Control) toolbox, MCSim (Marine Cybernetics Simulator) and DCMV (Dynamics and Control of Marine Vehicles). The Marine GNC toolbox was firstly developed by Fossen T. I. and his students at NTNU as a supporting tool for his book (Fossen, 2002). The MCSim was a complete simulator of DP marine operations, which was developed by Sørensen A. J. and Smogeli ∅. N. at NTNU (Sørensen et al., 2003). The DCMV toolbox was developed by Perez and Blanke (2003) for autopilot design.

In this study, the multi-cable mooring system, riser FEM model and level ice model were added in the original MSS to execute the proposed PM control strategy.
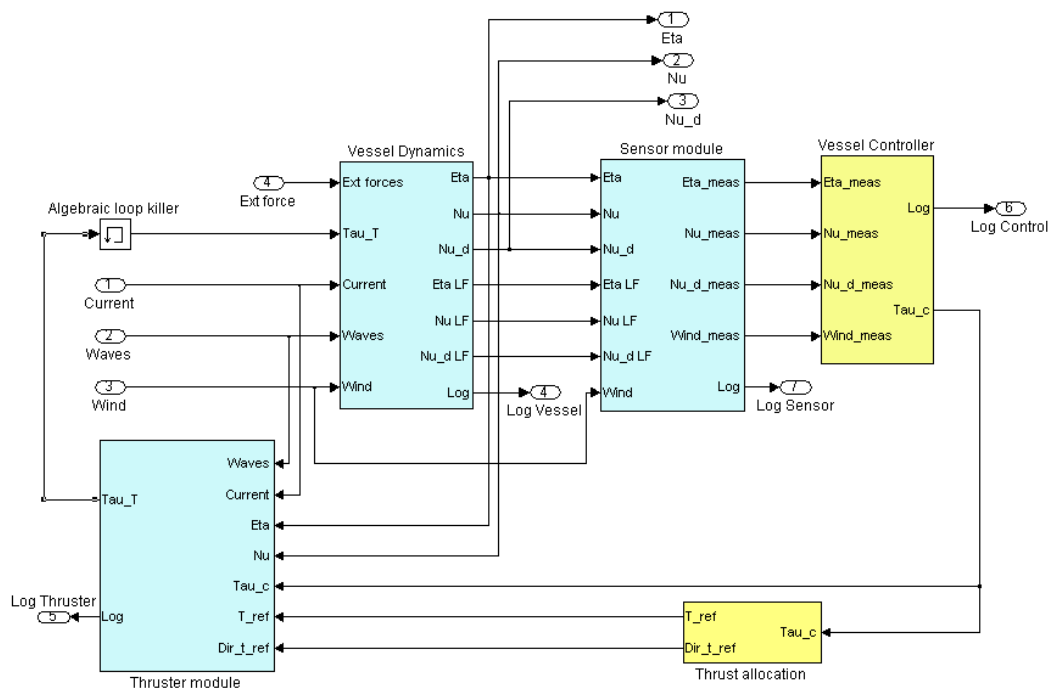

Figure B.1. Marine systems simulator

APPENDIX C. PUBLICATIONS AND SUBMITTED PAPERS

C.1 Journal Papers

[1]   Nguyen H. D., Nguyen T. D., Quek S. T. and Sørensen A. J. (2010). Control of marine riser end angles by position mooring. *Journal of Control Engineering Practice*, Vol. 18, No. 9, pp. 1013-1021.

[2]   Nguyen H. D., Nguyen T. D., Quek S. T. and Sørensen A. J. (2011). Position-moored drilling vessel in level ice by control of riser end angles. *Journal of Cold Regions Science and Technology*, Vol. 66, No. 2-3, pp. 65-74.

C.2 Conference Papers

[3]   Nguyen H. D., Quek S. T. and Nguyen T. D. (2007). Modelling of drilling marine riser: Comparisons in static analysis. *In Proceedings of 1st International Conference on Modern Design, Construction and Maintenance of Structures (MDCMS)*, Vol. 2, pp. 243–252, Hanoi, Vietnam, December 10–11.

[4]   Nguyen H. D. and Quek S. T. (2007). Comparison of cable and tensioned beam models for marine riser. *In Proceedings of Twentieth KKCNN Symposium on Civil Engineering*, Jeju, Korea, October.

[5]   Nguyen H. D., Nguyen T. D., Quek S. T. and Sørensen A. J. (2008). Control of marine drilling riser angles by position mooring. *In Proceedings of the Marine Operations Specialty Symposium 2008 – MOSS-2008*, pp. 367–379, CORE, National University of Singapore, Singapore, March 5–7.

[6]   Nguyen H. D., Nguyen T. D., Quek S. T. and Sørensen A. J. (2009). Design of marine riser angle control by position mooring. *In Proceedings of Twenty-Second KKCNN Symposium on Civil Engineering*, Chiengmai, Thailand, October 31 – November 2.

[7]   Nguyen H. D., Nguyen T. D. and Quek S. T. (2010). Control of marine riser in level-ice environment. *In Proceedings of Twenty-Third KKCNN Symposium on Civil Engineering*, Taipei, Taiwan, November 13 – 15.